SANDIA REPORT

SAND2015-7998
Unlimited Release
Printed September 2015

Strong Local-Nonlocal Coupling for Integrated Fracture Modeling

David J. Littlewood, Stewart A. Silling, John A. Mitchell, Pablo D. Seleson, Stephen D. Bond, Michael L. Parks, Daniel Z. Turner, Damon J. Burnett, Jakob Ostien, and Max Gunzburger

Prepared by
Sandia National Laboratories
Albuquerque, New Mexico 87185 and Livermore, California 94550

Sandia National Laboratories is a multi-program laboratory managed and operated by Sandia Corporation, a wholly owned subsidiary of Lockheed Martin Corporation, for the U.S. Department of Energy's National Nuclear Security Administration under contract DE-AC04-94AL85000.

Sandia National Laboratories

Issued by Sandia National Laboratories, operated for the United States Department of Energy by Sandia Corporation.

Available to DOE and DOE contractors from
U.S. Department of Energy
Office of Scientific and Technical Information
P.O. Box 62
Oak Ridge, TN 37831

Telephone: (865) 576-8401
Facsimile: (865) 576-5728
E-Mail: reports@adonis.osti.gov
Online ordering: http://www.osti.gov/bridge

Available to the public from
U.S. Department of Commerce
National Technical Information Service
5285 Port Royal Rd
Springfield, VA 22161

Telephone: (800) 553-6847
Facsimile: (703) 605-6900
E-Mail: orders@ntis.fedworld.gov
Online ordering: http://www.ntis.gov/help/ordermethods.asp?loc=7-4-0#online

SAND2015-7998
Unlimited Release
Printed September 2015

Strong Local-Nonlocal Coupling for Integrated Fracture Modeling

David J. Littlewood
Center for Computing Research
Sandia National Laboratories
P.O. Box 5800
Albuquerque, NM 87185-1322
djlittl@sandia.gov

Stewart A. Silling
Center for Computing Research
Sandia National Laboratories
P.O. Box 5800
Albuquerque, NM 87185-1322
sasilli@sandia.gov

John A. Mitchell
Center for Computing Research
Sandia National Laboratories
P.O. Box 5800
Albuquerque, NM 87185-1322
jamitch@sandia.gov

Pablo D. Seleson
Computer Science and Mathematics Division
Oak Ridge National Laboratory
P.O. Box 2008
Oak Ridge, TN 37831-6211
selesonpd@ornl.gov

Stephen D. Bond
Center for Computing Research
Sandia National Laboratories
P.O. Box 5800
Albuquerque, NM 87185-1318
sdbond@sandia.gov

Michael L. Parks
Center for Computing Research
Sandia National Laboratories
P.O. Box 5800
Albuquerque, NM 87185-1320
mlparks@sandia.gov

Daniel Z. Turner
Center for Computing Research
Sandia National Laboratories
P.O. Box 5800
Albuquerque, NM 87185-1323
dturne@sandia.gov

Damon J. Burnett
Homeland Security and Defense Systems Center
Sandia National Laboratories
P.O. Box 5800
Albuquerque, NM 87185-1160
dburnet@sandia.gov

Jakob Ostien
Weapon Systems Engineering
Sandia National Laboratories
P.O. Box 969
Livermore, CA 94551-9042
jtostie@sandia.gov

Max Gunzburger
Department of Scientific Computing
Florida State University
Tallahassee, FL 32306-4120
gunzburg@fsu.edu

Abstract

Peridynamics, a nonlocal extension of continuum mechanics, is unique in its ability to capture pervasive material failure. Its use in the majority of system-level analyses carried out at Sandia, however, is severely limited, due in large part to computational expense and the challenge posed by the imposition of nonlocal boundary conditions. Combined analyses in which peridynamics is employed only in regions susceptible to material failure are therefore highly desirable, yet available coupling strategies have remained severely limited. This report is a summary of the Laboratory Directed Research and Development (LDRD) project "Strong Local-Nonlocal Coupling for Integrated Fracture Modeling," completed within the Computing and Information Sciences (CIS) Investment Area at Sandia National Laboratories. A number of challenges inherent to coupling local and nonlocal models are addressed. A primary result is the extension of peridynamics to facilitate a variable nonlocal length scale. This approach, termed the peridynamic partial stress, can greatly reduce the mathematical incompatibility between local and nonlocal equations through reduction of the peridynamic horizon in the vicinity of a model interface. A second result is the formulation of a blending-based coupling approach that may be applied either as the primary coupling strategy, or in combination with the peridynamic partial stress. This blending-based approach is distinct from general blending methods, such as the Arlequin approach, in that it is specific to the coupling of peridynamics and classical continuum mechanics. Facilitating the coupling of peridynamics and classical continuum mechanics has also required innovations aimed directly at peridynamic models. Specifically, the properties of peridynamic constitutive models near domain boundaries and shortcomings in available discretization strategies have been addressed. The results are a class of position-aware peridynamic constitutive laws for dramatically improved consistency at domain boundaries, and an enhancement to the meshfree discretization applied to peridynamic models that removes irregularities at the limit of the nonlocal length scale and dramatically improves convergence behavior. Finally, a novel approach for modeling ductile failure has been developed, motivated by the desire to apply coupled local-nonlocal models to a wide variety of materials, including ductile metals, which have received minimal attention in the peridynamic literature. Software implementation of the partial-stress coupling strategy, the position-aware peridynamic constitutive models, and the strategies for improving the convergence behavior of peridynamic models was completed within the *Peridigm* and *Albany* codes, developed at Sandia National Laboratories and made publicly available under the open-source 3-clause BSD license.

Acknowledgment

This work was funded by the Computing and Information Sciences (CIS) Investment Area within the Laboratory Directed Research and Development (LDRD) Program at Sandia National Laboratories, project number 165616 and title “Strong Local-Nonlocal Coupling for Integrated Fracture Modeling.” The authors thank the CIS committee, Program Manager Randall Summers, and manager Veena Tikare for their support.

Contents

Appendix

List of Figures

List of Tables

Chapter 1

Introduction

Peridynamics is a nonlocal extension of continuum mechanics that seeks to unify the mechanics of continuous media, cracks, and particles [61, 64, 65]. Unlike classical approaches incorporating partial derivatives, the peridynamic governing equations utilize integral expressions that remain valid in the presence of discontinuities. The result is a consistent framework for capturing a wide range of constitutive responses in combination with material failure. The application of peridynamics for system-level analyses is challenging, however, due largely to computational expense and the need to specify constraints over a nonlocal volumetric boundary region [2, 43]. Additionally, characteristics of nonlocal models, such as wave dispersion, are desirable in some cases but undesirable in others.

This study focuses on enabling combined analyses, in which peridynamics is applied within regions susceptible to material failure and classical continuum mechanics is applied elsewhere. A primary result is the extension of peridynamics to facilitate a variable nonlocal length scale [67, 66]. This approach, termed the peridynamic partial stress, can greatly reduce the mathematical incompatibility between local and nonlocal equations through reduction of the peridynamic horizon in the vicinity of a model interface. It has been proven to provide exact solutions to a certain class of equilibrium problems, and numerical experiments have demonstrated its viability for model coupling within a computational simulation. A second result is the formulation of a blending-based coupling approach [55, 2] that may be applied either as the primary coupling strategy, or in combination with the peridynamic partial stress. This blending-based approach is distinct from general blending methods, such as the Arlequin approach, in that it is specific to the coupling of peridynamics and classical continuum mechanics. This specialization manifests as an additional coupling term that mitigates so-called ghost forces at local-nonlocal interfaces.

Facilitating the coupling of peridynamics and classical continuum mechanics has also required innovations aimed directly at the peridynamic models. Specifically, the properties of peridynamic constitutive models near domain boundaries and shortcomings in available discretization strategies have been addressed. The results are a position-aware peridynamic constitutive law [37] for dramatically improved consistency at domain boundaries, and an enhancement to the meshfree discretization often applied to peridynamic models that removes irregularities at the limit of the peridynamic horizon [51, 56].

Local-nonlocal coupling strategies and improved peridynamic models developed in this study have been implemented in the *Peridigm* [46, 48] peridynamics code and the *Laboratory for Com-*

putational Mechanics module of the *Albany* [50] code. Both *Peridigm* and *Albany* are open-source software that leverage *Trilinos* [25, 26] agile components and are distributed under the 3-clause BSD license. Combined peridynamic and classical continuum mechanics simulations have been enabled within a single, unified executable. Nonlocal domains are modeled using the meshfree peridynamic discretization of Silling and Askari [63, 32] while local domains are discretized using standard finite-element approaches. The coupling of local and nonlocal models provides an integrated fracture modeling capability that combines the strengths of peridynamics with those of classical continuum mechanics.

This report is organized as follows. Chapters 2 and 3 present strategies for the direct coupling of local and nonlocal models. An extension to peridynamic models allowing for a variable nonlocal length scale is presented first, followed by a blending-based coupling approach specific to peridynamics and classical continuum mechanics. Next are chapters covering improvements to peridynamics that increase compatibility with classical models and strengthen peridynamics as an engineering tool. A new class of position-aware constitutive models is given in Chapter 4, followed by improvements to the convergence behavior of peridynamics in Chapter 5, and a novel method for incorporating classical ductile failure models within the peridynamic framework in Chapter 6. Details regarding the software implementation strategy employed in this study are given in Chapter 7. A complete list of publications and presentations resulting from this project is given in Appendix A.

Chapter 2

Variable Nonlocal Length Scale for Peridynamic Models

2.1 Introduction

In the peridynamic theory, the classical (local) partial differential equations of solid mechanics are recovered in the limit of zero length scale [21, 68]. Therefore, the problem of local-to-nonlocal coupling can be viewed as the problem of changing the length scale within a region as a function of position. In this chapter, we report on our research that, first, shows that this length scale (the peridynamic horizon) cannot be varied arbitrarily without resulting in spurious "ghost forces" that create undesirable features in the solution. Second, we discuss new techniques to address this problem, resulting in viable methods for local-to-nonlocal coupling. A complete treatment of the work summarized in this chapter may be found in [67, 66].

The peridynamic theory is a strongly nonlocal formulation of solid mechanics, based on long-range forces, that is adapted to the study of continuous bodies with evolving discontinuities, including cracks [65]. Each material point $\mathbf{x}$ in the reference configuration of a body $\mathscr{B}$ interacts through the material model with other material points within a distance $\delta(\mathbf{x})$ of itself. The maximum interaction distance $\delta(\mathbf{x})$ is called the *horizon* of $\mathbf{x}$. The material points within the horizon of $\mathbf{x}$ comprise a set called the *material family* of $\mathbf{x}$:

$$\mathscr{F}_{\mathbf{x}} = \Big\{ \mathbf{q} \in \mathscr{B} \,:\, 0 < |\mathbf{q}-\mathbf{x}| \leq \delta(\mathbf{x}) \Big\}.$$

The vector from $\mathbf{x}$ to any neighboring material point $\mathbf{q} \in \mathscr{F}_{\mathbf{x}}$ is called a *bond*, $\boldsymbol{\xi} = \mathbf{q}-\mathbf{x}$. The set of bonds from $\mathbf{x}$ to its neighbors within its horizon is called the *family* of $\mathbf{x}$, denoted $\mathscr{H}_{\mathbf{x}}$:

$$\mathscr{H}_{\mathbf{x}} = \Big\{ \boldsymbol{\xi} \in \mathbb{R}^3 \,:\, \mathbf{x}+\boldsymbol{\xi} \in \mathscr{F}_{\mathbf{x}} \Big\}.$$

In an elastic peridynamic solid, the strain energy density $W(\mathbf{x})$ is determined by the collective deformation of $\mathscr{F}_{\mathbf{x}}$. To express this collective deformation, it is convenient to define the function $\underline{\mathbf{Y}}[\mathbf{x},t]\langle\cdot\rangle : \mathscr{H}_{\mathbf{x}} \to \mathbb{R}^3$ that maps bonds into their images under the deformation $\mathbf{y}$. For any material point $\mathbf{q} \in \mathscr{F}_{\mathbf{x}}$ at time t, let

$$\underline{\mathbf{Y}}[\mathbf{x},t]\langle \mathbf{q}-\mathbf{x} \rangle = \mathbf{y}(\mathbf{q},t) - \mathbf{y}(\mathbf{x},t). \tag{2.1}$$

The function $\underline{\mathbf{Y}}[\mathbf{x},t]\langle\cdot\rangle$ is called the *deformation state*. States are mappings from bonds in a family to some other quantity. The inner product of two states $\underline{\mathbf{A}}$ and $\underline{\mathbf{B}}$ is defined by

$$\underline{\mathbf{A}} \bullet \underline{\mathbf{B}} = \int_{\mathscr{H}} \underline{\mathbf{A}}\langle\boldsymbol{\xi}\rangle \cdot \underline{\mathbf{B}}\langle\boldsymbol{\xi}\rangle \, dV_{\boldsymbol{\xi}}. \tag{2.2}$$

In an elastic material, the strain energy density $W(\mathbf{x})$ depends through the material model on the deformation state, and this dependence is written

$$W(\mathbf{x}) = \hat{W}(\underline{\mathbf{Y}}[\mathbf{x}]).$$

In manipulating functions of states such as W, it is helpful to introduce the *Fréchet derivative*. The Fréchet derivative $\hat{W}_{\underline{\mathbf{Y}}}$ is a functional derivative with the property that if $\delta\underline{\mathbf{Y}}$ is a small increment in the deformation state,

$$\hat{W}(\underline{\mathbf{Y}} + \delta\underline{\mathbf{Y}}) = \hat{W}(\underline{\mathbf{Y}}) + \hat{W}_{\underline{\mathbf{Y}}}(\underline{\mathbf{Y}}) \bullet \delta\underline{\mathbf{Y}} + O(\|\delta\underline{\mathbf{Y}}\|). \tag{2.3}$$

(Note that $\hat{W}_{\underline{\mathbf{Y}}}$ is a state-valued function even though $\hat{W}$ is scalar-valued.)

The equilibrium equation in peridynamics can be obtained from the Euler-Lagrange equation associated with stationary values of total potential energy. This equation is given by

$$\mathbf{L}^{\mathrm{pd}}(\mathbf{x}) + \mathbf{b}(\mathbf{x}) = \mathbf{0} \tag{2.4}$$

for all $\mathbf{x} \in \mathscr{B}$. Here, the *peridynamic internal force density* at $\mathbf{x}$ is given by

$$\mathbf{L}^{\mathrm{pd}}(\mathbf{x}) = \int_{\mathscr{B}} \left\{ \underline{\mathbf{T}}[\mathbf{x}]\langle\mathbf{q}-\mathbf{x}\rangle - \underline{\mathbf{T}}[\mathbf{q}]\langle\mathbf{x}-\mathbf{q}\rangle \right\} dV_{\mathbf{q}}, \tag{2.5}$$

where $\underline{\mathbf{T}}[\mathbf{x}]$ is the *force state* at $\mathbf{x}$, which is related to the strain energy density by

$$\underline{\mathbf{T}}[\mathbf{x}] = \hat{W}_{\underline{\mathbf{Y}}}(\underline{\mathbf{Y}}[\mathbf{x}]). \tag{2.6}$$

The *pairwise bond force density* $\mathbf{f}$ on a point $\mathbf{x}$ due to interaction with any point $\mathbf{q} \in \mathscr{F}_{\mathbf{x}}$ is given by

$$\mathbf{f}(\mathbf{q},\mathbf{x}) = \underline{\mathbf{T}}[\mathbf{x}]\langle\mathbf{q}-\mathbf{x}\rangle - \underline{\mathbf{T}}[\mathbf{q}]\langle\mathbf{x}-\mathbf{q}\rangle. \tag{2.7}$$

As shown in [31], the peridynamic internal force density can be expressed without approximation as

$$\mathbf{L}^{\mathrm{pd}} = \nabla \cdot \boldsymbol{\nu}^{\mathrm{pd}} \qquad \text{on } \mathscr{B}$$

where $\boldsymbol{\nu}^{\mathrm{pd}}$ is the *peridynamic stress tensor* field defined for any $\mathbf{x}$ by

$$\boldsymbol{\nu}^{\mathrm{pd}}(\mathbf{x}) = \frac{1}{2} \int_{\mathscr{S}} \int_0^{\infty} \int_0^{\infty} (v+w)^2 \mathbf{f}(\mathbf{x}+v\mathbf{m}, \mathbf{x}-w\mathbf{m}) \otimes \mathbf{m} \, dw \, dv \, d\Omega_{\mathbf{m}} \tag{2.8}$$

where $\mathscr{S}$ is the unit sphere, $d\Omega_{\mathbf{m}}$ is a differential solid angle in the direction of the unit vector $\mathbf{m}$, and $\mathbf{f}$ is given by (2.7).

In a *uniform* deformation, there is a constant tensor $\mathbf{F}$ such that $\mathbf{y}(\mathbf{x}) = \mathbf{x}_0 + \mathbf{F}\mathbf{x}$ for all $\mathbf{x}$. If the deformation is uniform and the body is homogeneous and occupies $\mathbb{R}^3$, then it is easily shown that

$$\boldsymbol{\nu}^{\text{pd}} = \boldsymbol{\nu}^0 \tag{2.9}$$

where $\boldsymbol{\nu}^0$ is the *collapsed stress tensor* defined by

$$\boldsymbol{\nu}^0 = \int_{\mathscr{H}} \underline{\hat{\mathbf{T}}}(\underline{\mathbf{F}})\langle\boldsymbol{\xi}\rangle \otimes \boldsymbol{\xi}\, dV_{\boldsymbol{\xi}}. \tag{2.10}$$

Also define the *collapsed internal force density* field by

$$\mathbf{L}^0 = \nabla \cdot \boldsymbol{\nu}^0 \qquad \text{on } \mathscr{B}. \tag{2.11}$$

As discussed in [68], the collapsed stress tensor is an admissible first Piola-Kirchhoff stress tensor whose constitutive model depends on the local deformation gradient tensor through (2.10). The collapsed internal force density field provides the "local limit of peridynamics" in the sense that as $\delta \to 0$,

$$\mathbf{L}^{\text{pd}} \to \mathbf{L}^0$$

provided the deformation is twice continuously differentiable and $\underline{\hat{\mathbf{T}}}$ obeys the scaling relation derived in the next section.

2.2 Rescaling a material model at a point

Suppose an elastic material model is given for a particular value of horizon (without loss of generality, we will assume that this horizon is 1), and call the strain energy density function $\hat{W}_1$. An elastic material model with a different horizon δ has the same bulk response provided

$$\hat{W}(\underline{\mathbf{Y}}) = \hat{W}_1(\underline{\mathbf{Y}}_1) \tag{2.12}$$

where $\underline{\mathbf{Y}}_1$ is the *reference deformation state* defined by

$$\underline{\mathbf{Y}}_1\langle\mathbf{n}\rangle = \delta^{-1}\underline{\mathbf{Y}}\langle\delta\mathbf{n}\rangle \qquad \forall \mathbf{n} \in \mathscr{H}_1 \tag{2.13}$$

where $\mathscr{H}_1$ is the family of $\mathbf{x}$ with horizon 1.

As shown in detail in [67, 66], the force state rescales for any δ according to

$$\underline{\hat{\mathbf{T}}}(\underline{\mathbf{Y}})\langle\boldsymbol{\xi}\rangle = \delta^{-(1+D)}\underline{\hat{\mathbf{T}}}_1(\underline{\mathbf{Y}}_1)\langle\delta^{-1}\boldsymbol{\xi}\rangle \qquad \forall \boldsymbol{\xi} \in \mathscr{H} \tag{2.14}$$

where D is the number of dimensions and $\underline{\mathbf{Y}}_1$ is given by (2.13). $\underline{\hat{\mathbf{T}}}_1$ is called the *reference material model*. Furthermore, the collapsed stress tensor, like W, is invariant to changes in δ.

A peridynamic body $\mathscr{B}$ is a *variable scale homogeneous* (VSH) body if for some reference material model $\underline{\hat{\mathbf{T}}}_1$, the material model at any point $\mathbf{x}$ follows the scaling relation (2.14):

$$\underline{\hat{\mathbf{T}}}(\underline{\mathbf{Y}}[\mathbf{x}], \mathbf{x})\langle\boldsymbol{\xi}\rangle = \frac{1}{(\delta(\mathbf{x}))^{1+D}}\underline{\hat{\mathbf{T}}}_1(\underline{\mathbf{Y}}_1[\mathbf{x}])\left\langle \frac{\boldsymbol{\xi}}{\delta(\mathbf{x})} \right\rangle \qquad \boldsymbol{\xi} \in \mathscr{H}_{\mathbf{x}}. \tag{2.15}$$

2.3 Ghost forces

Here we demonstrate that in the absence of body forces, a uniform deformation of a VSH body is not necessarily in equilibrium. To see this, assume that δ is twice continuously differentiable, and compute the net internal force density $\mathbf{L}^{\mathrm{pd}}(\mathbf{x})$. For a uniform deformation of a VSH body, from (2.5) and (2.15), for any $\mathbf{x}$,

$$\begin{aligned}\mathbf{L}^{\mathrm{pd}}(\mathbf{x}) &= \int \{\underline{\mathbf{T}}[\mathbf{x}]\langle \mathbf{q}-\mathbf{x}\rangle - \underline{\mathbf{T}}[\mathbf{q}]\langle \mathbf{x}-\mathbf{q}\rangle\}\, dV_{\mathbf{q}} \\ &= \int \left\{\delta^{-(1+D)}(\mathbf{x})\underline{\mathbf{T}}_1\langle \mathbf{m}\rangle - \delta^{-(1+D)}(\mathbf{q})\underline{\mathbf{T}}_1\langle \mathbf{n}\rangle\right\} dV_{\mathbf{q}} \end{aligned} \tag{2.16}$$

where

$$\mathbf{m} = \frac{\mathbf{q}-\mathbf{x}}{\delta(\mathbf{x})}, \qquad \mathbf{n} = \frac{\mathbf{x}-\mathbf{q}}{\delta(\mathbf{q})}. \tag{2.17}$$

(All volume integrals are over $\mathbb{R}^3$.)

It is shown in detail in [67, 66] that,

$$\mathbf{L}^{\mathrm{pd}}(\mathbf{x}) = O(|\nabla\nabla\delta|)O(\|\underline{\mathbf{T}}_1\|). \tag{2.18}$$

The departure from equilibrium represented by nonzero values of $\mathbf{L}^{\mathrm{pd}}$ is called *ghost force* and is an artifact of the position dependence of the horizon. Observe that the leading term in the ghost force depends on the *second* derivative of δ. In fact, it can be shown directly that if δ is a linear function of position, then the ghost force vanishes.

An illustration of the effect of ghost force in a VSH bar in equilibrium is shown in Figure 2.1. The peridynamic reference material model $\hat{\underline{\mathbf{T}}}_1$ is a bond-based model [61] with a nominal Young's modulus of 1. The horizon in the bar depends on position as shown in the top figure. The numerical approximation method is discussed in detail in [67, 66] and is similar to the meshless method described in [63]. Two cases are considered for dependence of the horizon: piecewise linear ("not smoothed") and cubic spline ("smoothed"). The ends of the bar have prescribed displacements corresponding to a nominal strain in the bar of 1. The strain (defined as du/dx) in equilibrium for the two cases is shown in the lower figure (strain is computed numerically using a central finite difference formula). If there were no ghost forces, the strain would be constant and equal to 1. Because of ghost forces, anomalies in strain ("ghost strains") appear that equilibrate the ghost forces. The smoothed $\delta(x)$ has lower ghost strains than the non-smoothed case. This result is consistent with (2.18), which predicts ghost forces proportional to the second derivative of $\delta(x)$.

2.4 Partial stress field

Here we investigate a modified form of the momentum balance that eliminates ghost forces in a VSH body under uniform deformation. The momentum balance is expressed in terms of a new field called the "partial stress" tensor field.

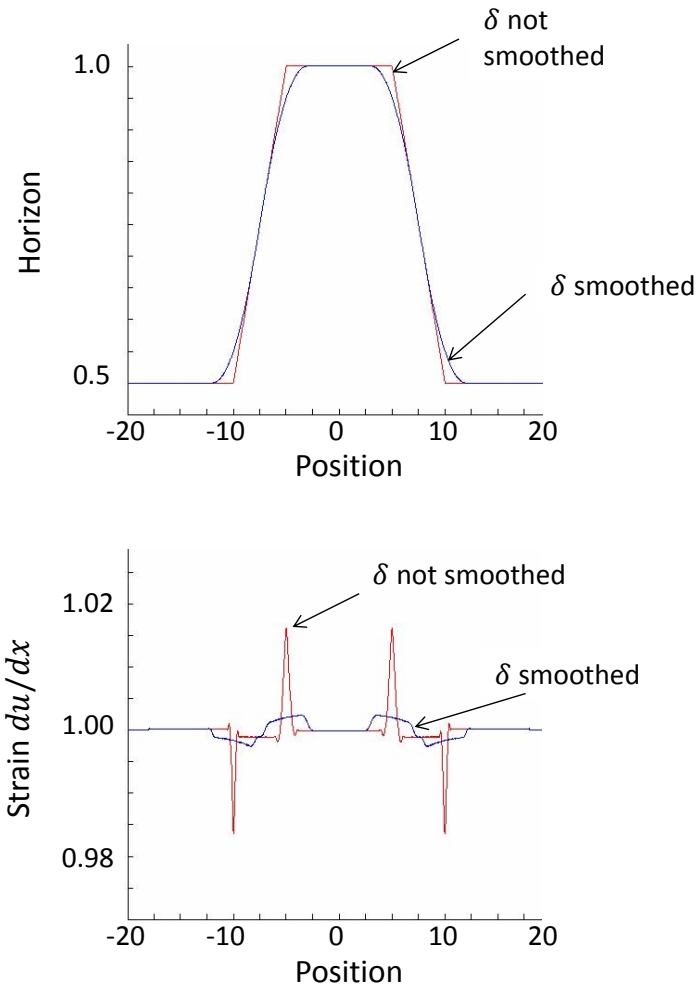

Figure 2.1: Ghost strain in a VSH body in equilibrium. Top: horizon as a function of position. Bottom: strain as a function of position.

Consider a peridynamic body $\mathscr{B}$ and let its force state field $\underline{\mathbf{T}}$ be given. Let the *partial stress* tensor field $\boldsymbol{\nu}^{\mathrm{ps}}$ be defined by

$$\boldsymbol{\nu}^{\mathrm{ps}}(\mathbf{x}) = \int_{\mathscr{H}_{\mathbf{x}}} \underline{\mathbf{T}}[\mathbf{x}]\langle \boldsymbol{\xi} \rangle \otimes \boldsymbol{\xi} \, dV_{\boldsymbol{\xi}} \qquad \forall \mathbf{x} \in \mathscr{B}. \tag{2.19}$$

Also define the *partial internal force density* by

$$\mathbf{L}^{\mathrm{ps}}(\mathbf{x}) = \nabla \cdot \boldsymbol{\nu}^{\mathrm{ps}}(\mathbf{x}) \qquad \forall \mathbf{x} \in \mathscr{B}. \tag{2.20}$$

In a VHS body under uniform deformation, $\boldsymbol{\nu}^{\mathrm{ps}} = \boldsymbol{\nu}^0$, moreover,

$$\boldsymbol{\nu}^{\mathrm{ps}}(\mathbf{x}) = \int_{\mathscr{H}_1} \hat{\underline{\mathbf{T}}}_1(\underline{\mathbf{Y}}_1[\mathbf{x}])\langle \mathbf{n} \rangle \otimes \mathbf{n} \, dV_{\mathbf{n}} \qquad \forall \mathbf{x} \in \mathscr{B} \tag{2.21}$$

where $\underline{\mathbf{Y}}_1$ is given by (2.13). Since, in a uniform deformation, $\underline{\mathbf{Y}}_1$ is constant (and equal to $\underline{\mathbf{F}}$), it follows that that in a VSH body under uniform deformation,

$$\boldsymbol{\nu}^{\mathrm{ps}} \equiv \boldsymbol{\nu}^0 \equiv \mathbf{0}, \qquad \mathbf{L}^{\mathrm{ps}} \equiv \mathbf{L}^0 \equiv \mathbf{0}. \tag{2.22}$$

This establishes that, for a VSH body under uniform deformation, ghost forces are absent in the partial stress formulation of the momentum balance equation. This observation suggests that the partial stress could be used in subregions of a body where the horizon changes, while the full peridynamic equations (or the local PDEs) could be used where it is constant (or zero).

The first task in investigating this possibility is to determine the errors that occur at the boundary between a partial stress region and a fully peridynamic region. As shown in [67, 66], these errors can be estimated from

$$\boldsymbol{\nu}^{\mathrm{pd}} - \boldsymbol{\nu}^{\mathrm{ps}} = O(\delta) O(\|\nabla \underline{\mathbf{T}}_1\|) \quad \text{on } \mathscr{B}, \tag{2.23}$$

$$\mathbf{L}^{\mathrm{pd}} - \mathbf{L}^{\mathrm{ps}} = O(\delta) O(\|\nabla\nabla \underline{\mathbf{T}}_1\|) \quad \text{on } \mathscr{B}. \tag{2.24}$$

Because of (2.24), it follows that at the interface between subregions where $\mathbf{L}^{\mathrm{ps}}$ and $\mathbf{L}^{\mathrm{pd}}$ are used in the momentum balance, there are no ghost forces if the deformation is uniform (since $\underline{\mathbf{T}}_1$ is constant on $\mathscr{B}$).

The above analysis showed how well the partial stress equations approximate the peridynamic equations. Similar analysis compares the partial stress equations with the local PDEs. The results are summarized in the following estimates:

$$\boldsymbol{\nu}^{\mathrm{ps}} - \boldsymbol{\nu}^0 = O(\delta) O(\|\nabla \underline{\mathbf{T}}_1\|) \qquad \text{on } \mathscr{B} \tag{2.25}$$

where $\boldsymbol{\nu}^{\mathrm{ps}}$ and $\boldsymbol{\nu}^0$ are defined by (2.19) and (2.10), and

$$\mathbf{L}^{\mathrm{ps}} - \mathbf{L}^0 = O(\delta) O(\|\nabla\nabla \underline{\mathbf{T}}_1\|) \qquad \text{on } \mathscr{B} \tag{2.26}$$

where $\mathbf{L}^{\mathrm{ps}}$ and $\mathbf{L}^0$ are defined by (2.20) and (2.11).

Comparing (2.23) with (2.25), and comparing (2.24) with (2.26), it follows that

$$\boldsymbol{\nu}^{\mathrm{pd}} - \boldsymbol{\nu}^0 = O(\delta) O(\|\nabla \underline{\mathbf{T}}_1\|) \quad \text{on } \mathscr{B}, \tag{2.27}$$

$$\mathbf{L}^{\mathrm{pd}} - \mathbf{L}^0 = O(\delta) O(\|\nabla\nabla \underline{\mathbf{T}}_1\|) \quad \text{on } \mathscr{B}. \tag{2.28}$$

This result is consistent with the conclusion in [68] that the collapsed internal force density is the "local limit of peridynamics."

2.5 Splice between two peridynamic subregions

Let two values of horizon be denoted δ_+ and δ_-, and assume $\delta_- \le \delta_+$. Let a reference material model $\hat{\underline{\mathbf{T}}}_1$ be given. Suppose, for a given deformation, two force state fields are computed everywhere using (2.14). For any $\mathbf{x} \in \mathscr{B}$,

$$\underline{\mathbf{T}}_+[\mathbf{x}]\langle\boldsymbol{\xi}\rangle = \frac{1}{\delta_+^{1+D}}\hat{\underline{\mathbf{T}}}_1(\underline{\mathbf{Y}}_1[\mathbf{x}])\langle\boldsymbol{\xi}/\delta_+\rangle, \qquad \underline{\mathbf{T}}_-[\mathbf{x}]\langle\boldsymbol{\xi}\rangle = \frac{1}{\delta_-^{1+D}}\hat{\underline{\mathbf{T}}}_1(\underline{\mathbf{Y}}_1[\mathbf{x}])\langle\boldsymbol{\xi}/\delta_-\rangle.$$

Further suppose that $\mathscr{B}$ is divided into two disjoint subregions $\mathscr{B}_+$ and $\mathscr{B}_-$ and that the internal force density at any $\mathbf{x} \in \mathscr{B}$ is given by

$$\mathbf{L}(\mathbf{x}) = \mathbf{L}^{\text{splice}}(\mathbf{x}) := \begin{cases} \int_{\mathscr{B}} \left\{ \underline{\mathbf{T}}_+[\mathbf{x}]\langle\mathbf{q}-\mathbf{x}\rangle - \underline{\mathbf{T}}_+[\mathbf{q}]\langle\mathbf{x}-\mathbf{q}\rangle \right\} dV_{\mathbf{q}} & \text{if } \mathbf{x} \in \mathscr{B}_+, \\ \int_{\mathscr{B}} \left\{ \underline{\mathbf{T}}_-[\mathbf{x}]\langle\mathbf{q}-\mathbf{x}\rangle - \underline{\mathbf{T}}_-[\mathbf{q}]\langle\mathbf{x}-\mathbf{q}\rangle \right\} dV_{\mathbf{q}} & \text{if } \mathbf{x} \in \mathscr{B}_-. \end{cases}$$

The resulting model of $\mathscr{B}$ is called a *splice* of the subregions $\mathscr{B}_+$ and $\mathscr{B}_-$.

A splice is not the same as a VSH with $\delta(\mathbf{x})$ prescribed as a step function. The difference is that in a splice, a point $\mathbf{x}$ near the interface "sees" the force states on the other side of the interface corresponding to the same value of horizon as itself, $\delta(\mathbf{x})$. In contrast, in a VSH, each point is assigned a unique value of horizon, and the force state at each point is uniquely computed according to this horizon. In many applications, a splice provides a viable and convenient way to model a VSH body that has piecewise constant values of horizon.

2.6 Local-nonlocal coupling

One option for local-nonlocal coupling is to use the partial stress field as a bridge between local and peridynamic subregions. In this approach, $\mathscr{B}$ is divided into disjoint subregions $\mathscr{B}_0$, $\mathscr{B}_{\text{ps}}$, and $\mathscr{B}_{\text{pd}}$. To avoid ghost forces under uniform deformation, $\delta > 0$ is assumed to be constant in $\mathscr{B}_{\text{pd}}$. Changes in δ occur entirely within $\mathscr{B}_{\text{ps}}$, so that δ is continuous on $\mathscr{B}$. (Recall from (2.22) that $\boldsymbol{\nu}^{\text{ps}} \equiv \boldsymbol{\nu}^0$ and $\mathbf{L}^{\text{ps}} \equiv \mathbf{L}^0$ where $\delta \equiv 0$.) The internal force density is given by

$$\mathbf{L}(\mathbf{x}) = \begin{cases} \mathbf{L}^{\text{pd}}(\mathbf{x}) & \text{if } \mathbf{x} \in \mathscr{B}_{\text{pd}}, \\ \mathbf{L}^{\text{ps}}(\mathbf{x}) & \text{if } \mathbf{x} \in \mathscr{B}_{\text{ps}}, \\ \mathbf{L}^0(\mathbf{x}) & \text{if } \mathbf{x} \in \mathscr{B}_0. \end{cases} \tag{2.29}$$

The convergence properties of this method were derived in (2.24) and (2.26).

Another option for local-nonlocal coupling is to use the idea of a splice described in the previous section. The body is divided into disjoint subregions $\mathscr{B}_0$ and $\mathscr{B}_{\text{pd}}$ that use the local model and the full peridynamic model (constant $\delta > 0$), respectively. The internal force density in the splice model is given by

$$\mathbf{L}(\mathbf{x}) = \begin{cases} \mathbf{L}^{\text{pd}}(\mathbf{x}) & \text{if } \mathbf{x} \in \mathscr{B}_{\text{pd}}, \\ \mathbf{L}^0(\mathbf{x}) & \text{if } \mathbf{x} \in \mathscr{B}_0. \end{cases} \tag{2.30}$$

The convergence properties of such a splice model are given by (2.28).

These two options for local-nonlocal coupling differ primarily in the way they transmit waves whose wavelength is smaller than or on the order of δ. As an example, we apply these two methods for local-nonlocal coupling to the problem of spall initiated by the impact of two brittle elastic plates. The impactor has half the thickness of the target and strikes the target from the left side. As shown in the wave diagram in Figure 2.3, the compressive waves that issue from the contact surface between the impactor and the target eventually intersect each other at the midplane of the target plate. When this happens, the waves, which by that time are both tensile, reinforce each other to create a thin region where the stress is strongly tensile. Within this tensile region, the strength of the material is exceeded and a crack forms. The formation of this crack creates relief pulses that move in both directions. The velocity induced by the rightward-moving relief pulse as it reflects from the free surface of the target bar can be measured using VISAR or other techniques [22]. With the help of analysis or computational modeling, the exact characteristics of the crack release (or "pullback") pulse can be interpreted using suitable data processing techniques to reveal the dynamic strength properties of materials under strong tension (spall).

In the computational model of this spall experiment, the impactor and target plates have thicknesses of 20 and 40 respectively. The impact velocity is 0.1. The elastic modulus and density of both plates are 1. The reference material model $\underline{\hat{\mathbf{T}}}_1$ is the bond-based prototype microelastic brittle (PMB) material model [63] with a critical bond strain for failure of 0.04. The entire region is discretized into 1000 nodes. The objective is to model the relatively small part of the body where damage can occur using the full peridynamic equations. This peridynamic region is coupled to local regions using either of two methods:

- Partial stress: a peridynamic region of thickness 10, centered at the midpoint of the target plate, is enclosed by layers of thickness 4 where the partial stress method is applied. Beyond this, the local equations are used. In the peridynamic and partial stress regions, the horizon is $\delta = 0.13$.
- Splice: a peridynamic region of thickness 10 and horizon $\delta = 0.13$, centered at the midpoint of the target plate, is spliced to local regions.

For comparison, results using the full peridynamic model in the entire domain ($\delta = 0.13$ throughout) are also computed.

The computed velocity profile using the splice method for local-nonlocal coupling is shown in Figure 2.2. The time of this snapshot is $t = 70$. Comparing this figure with the wave diagram in Figure 2.3, a number of salient features may be seen. The crack appears as a sharp jump in velocity as a function of position $x = 40$. The two release (pullback) pulses move away from the crack at the wave velocity, which is $c = 1.0$. The computed velocity history at the free surface is shown in Figure 2.4. The dips in velocity represent the crack release pulse created in the interior of the target due to spall.

As shown in the figures, the three methods give nearly the same results in this example. However, a fully peridynamic model in multiple dimensions would require a much higher computational

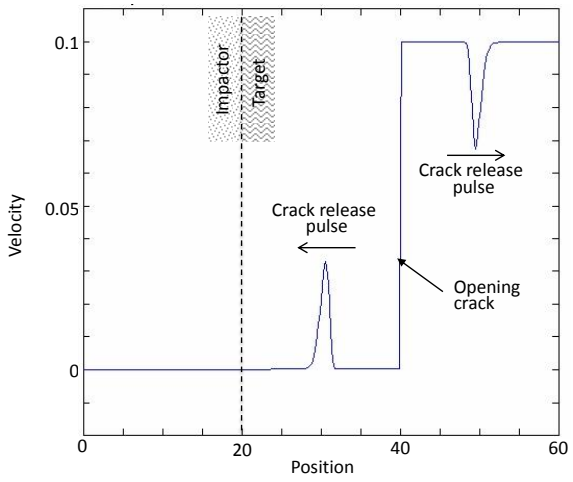

Figure 2.2: Velocity as a function of position at $t = 70$ in the spall example problem using the splice method for local-nonlocal coupling. There are no significant artifacts from the local-nonlocal transitions, which are located at $x = 37$ and $x = 43$.

cost due to the large number of nonlocal interactions required to discretize the material model. So, in multiple dimensions, in problems where damage is confined to a small subregion, the splice or partial stress methods potentially offer a significant reduction in cost, while avoiding ghost forces. This anticipated cost reduction is a primary motivation for development of local-nonlocal coupling methods.

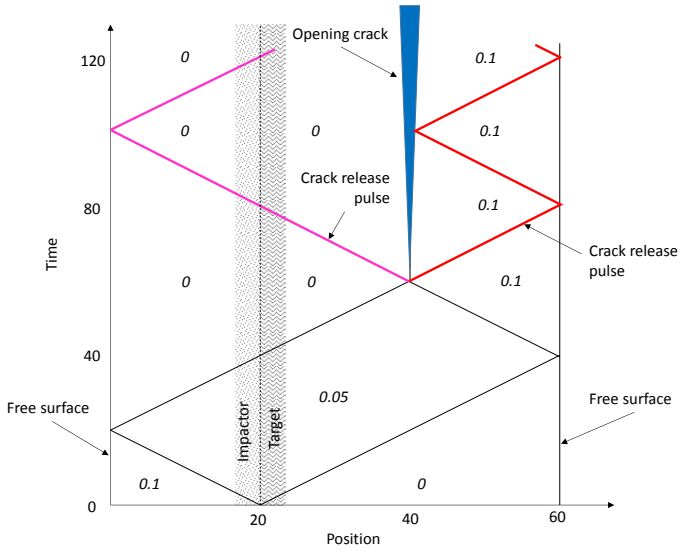

Figure 2.3: Wave diagram for the impact of a plate (from the left) on a target plate. Waves reinforce at the midplane of the target plate to cause fracture. Numbers in italics represent particle velocity.

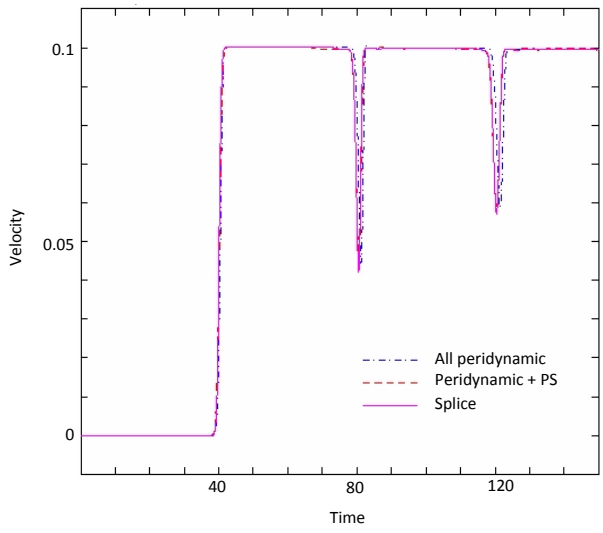

Figure 2.4: Velocity history at the free (right) surface of the target plate, showing the release pulse from the dynamic fracture occurring in the interior of the target bar. The three curves are for fully peridynamic (PD), local-nonlocal coupling using partial stress (PS), and local-nonlocal coupling using a splice.

Chapter 3

Blending-Based Coupling Approach

3.1 Introduction

Techniques for coupling local and nonlocal models can greatly expand the application space of peridynamics (PD). A foremost concern is computational expense, which in practice limits the use of PD in large-scale, geometrically complex simulations. The meshfree approach proposed in [63] is the most widely used discretization method in PD to date. For discretizations of this type, the computational cost and memory requirements are strongly tied to the number of interactions in a model, which depends on the ratio between the horizon and the distance between neighboring nodes. When this ratio becomes large, simulations can be intractable. The computational burden of PD is also evident in the structure of tangent stiffness matrices for implicit time integration. The number of nonzero elements in a PD stiffness matrix grows rapidly as the above-mentioned ratio increases, resulting in a bandwidth that is typically much larger than that of the stiffness matrix associated with a corresponding classical continuum mechanics (CCM) model. The same observation applies to finite element discretizations of PD models, when the horizon is large relative to the mesh size [58]. A second motivation for local-nonlocal coupling is the desire to combine the strengths of PD with those of CCM, for example as implemented in a traditional finite-element analysis code. The most obvious strength of PD models is their ability to capture pervasive material failure. Other traits of PD models may or may not be desirable in practice; for example, PD models introduce wave dispersion not always represented in CCM models [61, 57]. In addition, many classical finite element codes contain an array of features not widely available in PD codes, for example structural elements such as beams and joints. A third motivation for concurrent coupling of local and nonlocal models is the challenge posed by the imposition of nonlocal boundary conditions. Nonlocal models require the extension of classical boundary conditions, so that instead of these conditions being imposed on boundary surfaces, they are imposed in volumetric regions [54, 19, 1]. Many times, such extension is not well-defined. Concurrent coupling methods, however, offer the possibility to solve nonlocal problems equipped with classical local boundary conditions.

In [68], it was shown that PD converges to CCM in the limit of vanishing nonlocality, under proper regularity assumptions. In fact, it can be shown that for a certain class of problems, characterized by smooth deformations, PD and corresponding CCM models exhibit the same material response, as demonstrated below. As a consequence, it seems reasonable to replace PD governing equations with corresponding CCM equations in domains where the models behave similarly. In

that case, PD models could be applied in regions where discontinuities may be present, and CCM models could be used far from such regions, where displacement fields are smooth. Simulations based on a coupled PD/CCM model can result in efficient and accurate solutions of PD problems. The main challenge lies in the design of algorithms that properly couple the two models across interfaces.

There is a vast literature in the field of concurrent multiscale material modeling concerning methods for coupling nonlocal and local models. Specifically, approaches to concurrently couple nonlocal atomistic (discrete) models and local continuum models have been proposed. Such approaches are commonly referred to as atomistic-to-continuum (AtC) coupling methods. Common examples of AtC coupling methods include the Arlequin method [5, 49, 7, 18], the quasicontinuum method [29, 60, 69], blending methods [3, 4, 12, 23], and bridging domain methods [6, 75, 53], among others. A known problem, commonly present in these types of methods, is the appearance of spurious effects across transition regions connecting the nonlocal and local domains. These effects include the following: presence of "ghost forces" (i.e., forces acting on particles in equilibrium positions), failure to pass "patch tests" defined by uniform strain solutions, lack of energy preservation, breakdown of Newton's third law, and appearance of artificial wave reflections. Such effects are not present when using either of the reference models and are a result of the enforced coupling. In the case of AtC coupling, the atomistic and continuum models possess very disparate mathematical natures: the atomistic model is discrete, whereas the other model is continuum; the atomistic model is nonlocal, whereas the other model is local. Furthermore, the length and time scales at which atomistic and continuum models are typically applied differ by orders of magnitude. The situation is different in the coupling of PD and CCM models. First, both PD and CCM are continuum theories. Second, nonlocal PD models can be clearly connected to local CCM counterparts through a limiting process. Third, many of the problems that PD models are applied to are characterized by the same length and time scales as in CCM. These properties facilitate the derivation and analysis of coupling schemes involving PD and CCM models.

The coupling approach presented here belongs to the class of *blending methods*. In those methods, the domain of interest is decomposed into subdomains described by different models and a blending region where the models are blended. A blending function is then introduced to characterize each domain as well as to weight the contribution of each model across the blending region. Blending approaches typically appear in two flavors. In *energy-based blending schemes*, blended energy partitions are employed, possibly with certain constraints. In contrast, in *force-based blending schemes* the coupling is performed directly at the force level, using blended governing equations. The method presented here is a force-based blending approach.

3.2 Connections between peridynamic and classical models

For simplicity, we focus on linear isotropic microelastic bond-based PD models with a pairwise equilibrated reference configuration [61]. Let $\mathscr{B}$ be a continuum body. The corresponding PD

equilibrium equation for a point $\mathbf{x} \in \mathscr{B}$ is

$$\int_{\mathscr{B}} \lambda(\|\boldsymbol{\xi}\|)(\boldsymbol{\xi} \otimes \boldsymbol{\xi}) \left(\mathbf{u}(\mathbf{x}') - \mathbf{u}(\mathbf{x})\right) dV_{\mathbf{x}'} = -\mathbf{b}(\mathbf{x}), \tag{3.1}$$

where $\mathbf{u}$ is the displacement field, $\boldsymbol{\xi} := \mathbf{x}' - \mathbf{x}$ is the relative reference position vector or *bond*, $\mathbf{b}$ is a prescribed body force density field, and λ is a scalar-valued function depending on the bond length. It is assumed that each point in a body directly interacts with other points in that body within its neighborhood; the neighborhood of $\mathbf{x}$ is defined as

$$\mathscr{H}(\mathbf{x}, \delta) := \left\{\mathbf{x}' \in \mathbb{R}^d : \|\mathbf{x}' - \mathbf{x}\| \leqslant \delta\right\}, \tag{3.2}$$

where δ is referred to as the *PD horizon* and $d = 1, 2, \text{or } 3$ is the dimension, so that $\lambda(\|\boldsymbol{\xi}\|) = 0$ for $\|\boldsymbol{\xi}\| > \delta$ [61].

We now demonstrate that under proper regularity assumptions on the deformation, the PD equilibrium equation (3.1) reduces to the Navier-Cauchy equation of classical elasticity. Such connection is established for points in the bulk of a material, i.e., far from boundaries, and it is later employed as part of the derivation of the blended model. Let the internal subregion of $\mathscr{B}$ be defined as

$$\mathscr{B}^{0,\delta} := \{\mathbf{x} \in \mathscr{B} : \mathscr{H}(\mathbf{x}, \delta) \subset \mathscr{B}\} \tag{3.3}$$

and assume that for $\mathbf{x} \in \mathscr{B}^{0,\delta}$ the displacement field $\mathbf{u}$ is smooth, so that for $\|\boldsymbol{\xi}\| \leqslant \delta$ the following Taylor expansion holds:

$$\mathbf{u}(\mathbf{x}') = \mathbf{u}(\mathbf{x}) + (\boldsymbol{\xi} \cdot \nabla)\mathbf{u}(\mathbf{x}) + \frac{1}{2}(\boldsymbol{\xi} \cdot \nabla)(\boldsymbol{\xi} \cdot \nabla)\mathbf{u}(\mathbf{x}) + \mathscr{O}(\|\boldsymbol{\xi}\|^3). \tag{3.4}$$

We can then write (3.1) as

$$\left[\int_{\mathscr{H}(\mathbf{0},\delta)} \lambda(\|\boldsymbol{\xi}\|)\xi_i\xi_j\xi_k dV_{\boldsymbol{\xi}}\right] \frac{\partial u_j}{\partial x_k}(\mathbf{x})\hat{\mathbf{e}}_i + \frac{1}{2}\left[\int_{\mathscr{H}(\mathbf{0},\delta)} \lambda(\|\boldsymbol{\xi}\|)\xi_i\xi_j\xi_k\xi_\ell dV_{\boldsymbol{\xi}}\right] \frac{\partial^2 u_j}{\partial x_k \partial x_\ell}(\mathbf{x})\hat{\mathbf{e}}_i + \mathscr{O}(\delta^2) = -\mathbf{b}(\mathbf{x}), \tag{3.5}$$

where we used a change of integration variable, the Einstein summation convention for repeated indices, and $\hat{\mathbf{e}}_i$ as a unit vector in the ith direction. Due to the symmetry of the integration range, the first term on the left-hand side of (3.5) vanishes, because its integrand is antisymmetric. In a further Taylor expansion, the term containing third partial derivatives vanishes as well. Therefore, the leading term contributing to the truncation error is the one containing fourth partial derivatives of the displacement field, giving the $\mathscr{O}(\delta^2)$ error in (3.5). We observe that [55]

$$C_{ijk\ell} := \frac{1}{2}\int_{\mathscr{H}(\mathbf{0},\delta)} \lambda(\|\boldsymbol{\xi}\|)\xi_i\xi_j\xi_k\xi_\ell dV_{\boldsymbol{\xi}} = \left(\delta_{ij}\delta_{k\ell} + \delta_{ik}\delta_{j\ell} + \delta_{i\ell}\delta_{jk}\right)\frac{\Lambda}{3}, \tag{3.6}$$

where δ_{ij} is the Kronecker delta, $|\mathscr{H}(\mathbf{0}, 1)|$ is the size of a neighborhood of unit horizon, i.e., its volume, area, or length for $d = 3, 2$, or 1, respectively, and

$$\Lambda := \frac{3}{2}\frac{|\mathscr{H}(\mathbf{0}, 1)|}{d+2}\int_0^\delta \lambda(r) r^{d+3} dr. \tag{3.7}$$

In the limit as $\delta \to 0$, assuming $\Lambda < \infty$, Eq. (3.5) becomes

$$\frac{2\Lambda}{3}\left(\frac{\partial^2 u_j}{\partial x_i \partial x_j}(\mathbf{x}) + \frac{1}{2}\frac{\partial^2 u_i}{\partial x_k \partial x_k}(\mathbf{x})\right)\hat{\mathbf{e}}_i = -\mathbf{b}(\mathbf{x}). \tag{3.8}$$

Equation (3.8) is the Navier-Cauchy equation of classical elasticity, for a fixed Poisson's ratio of $\nu = 1/4$ in 3D or $\nu = 1/3$ in 2D with Young's modulus $E = 5\Lambda/6$ in 3D, $E = 8\Lambda/9$ in 2D, or $E = \Lambda$ in 1D. The restriction on the Poisson's ratio is due to the choice of a bond-based PD model. A general isotropic linear elastic state-based PD model would converge instead to a classical elastic model with two independent elastic moduli [61, 64].

3.3 A consistent force-based blending scheme

The derivation here is based on the work presented in [55]. Let the domain $\mathscr{B}$ be divided into three non-overlapping regions: $\mathscr{B}_{\text{PD}}$, $\mathscr{B}_{\text{CCM}}$, and $\mathscr{B}_{\text{b}}$, so that $\overline{\mathscr{B}} = \overline{\mathscr{B}_{\text{PD}}} \cup \overline{\mathscr{B}_{\text{CCM}}} \cup \overline{\mathscr{B}_{\text{b}}}$. A scalar-valued *blending function* is introduced, satisfying

$$\beta(\mathbf{x}) = \begin{cases} 1 & \mathbf{x} \in \mathscr{B}_{\text{PD}}, \\ 0 & \mathbf{x} \in \mathscr{B}_{\text{CCM}}, \\ \hat{\beta}(\mathbf{x}) & \mathbf{x} \in \mathscr{B}_{\text{b}}, \end{cases} \tag{3.9}$$

where $\hat{\beta} : \mathbb{R}^d \to (0,1)$ is taken as a continuous polynomial. We define the mean value of the blending function at $\mathbf{x} \in \mathscr{B}$ as

$$\langle\beta\rangle(\mathbf{x}) := \frac{\displaystyle\int_{\mathscr{H}(\mathbf{x},\delta)\cap\mathscr{B}} \beta(\mathbf{x}')\,dV_{\mathbf{x}'}}{\displaystyle\int_{\mathscr{H}(\mathbf{x},\delta)\cap\mathscr{B}} dV_{\mathbf{x}'}}. \tag{3.10}$$

The function $\langle\beta\rangle$ takes a value of 1 in $\mathscr{B}_{\text{PD}}^{0,\delta}$ and a value of 0 in $\mathscr{B}_{\text{CCM}}^{0,\delta}$. Let the *transition region* be defined as

$$\mathscr{B}_{\text{t}} := \{\mathbf{x} \in \mathscr{B} : 0 < \langle\beta\rangle(\mathbf{x}) < 1\}. \tag{3.11}$$

We assume the material response in $\mathscr{B}_{\text{PD}} \setminus \mathscr{B}_{\text{t}}$ to be described by the PD model (3.1). In $\mathscr{B}_{\text{CCM}} \setminus \mathscr{B}_{\text{t}}$, we assume displacement fields are smooth, so that we can use instead the Navier-Cauchy equation of classical elasticity (3.8). These two regions do not interact directly; they communicate through the transition region, $\mathscr{B}_{\text{t}}$.

To derive a force-based blending scheme, we take the PD governing equation (3.1) and begin by splitting the contribution of the internal force into two terms, through the introduction of symmetric weights based on the blending function, to obtain the equation

$$\begin{aligned} &\int_{\mathscr{B}} \frac{\beta(\mathbf{x}) + \beta(\mathbf{x}')}{2}\lambda(\|\boldsymbol{\xi}\|)(\boldsymbol{\xi}\otimes\boldsymbol{\xi})\left(\mathbf{u}(\mathbf{x}') - \mathbf{u}(\mathbf{x})\right)dV_{\mathbf{x}'} \\ &+ \int_{\mathscr{B}} \left(1 - \frac{\beta(\mathbf{x}) + \beta(\mathbf{x}')}{2}\right)\lambda(\|\boldsymbol{\xi}\|)(\boldsymbol{\xi}\otimes\boldsymbol{\xi})\left(\mathbf{u}(\mathbf{x}') - \mathbf{u}(\mathbf{x})\right)dV_{\mathbf{x}'} = -\mathbf{b}(\mathbf{x}). \end{aligned} \tag{3.12}$$

By introducing symmetric weights with respect to interchanging $\mathbf{x}$ and $\mathbf{x}'$, we preserve the antisymmetry of the integrand in each of the two terms on the left-hand side of (3.12). We now observe that the second term on the left-hand side of (3.12) vanishes for $\mathbf{x} \in \mathscr{B}_{\mathrm{PD}}^{0,\delta}$, because $\beta(\mathbf{x}) = \beta(\mathbf{x}') = 1, \forall \mathbf{x}' \in \mathscr{H}(\mathbf{x}, \delta)$. Let us assume that the displacement field in $\mathscr{B} \setminus \mathscr{B}_{\mathrm{PD}}^{0,\delta}$ is smooth enough so that the Taylor expansion (3.4) holds for all points in that region and $\|\boldsymbol{\xi}\| \leqslant \delta$. In this case, we can write (3.12) as

$$\begin{aligned}
&\int_{\mathscr{B}} \frac{\beta(\mathbf{x}) + \beta(\mathbf{x}')}{2} \lambda(\|\boldsymbol{\xi}\|)(\boldsymbol{\xi} \otimes \boldsymbol{\xi}) \left(\mathbf{u}(\mathbf{x}') - \mathbf{u}(\mathbf{x})\right) dV_{\mathbf{x}'} \\
&+ \int_{\mathscr{B}} \left(1 - \frac{\beta(\mathbf{x}) + \beta(\mathbf{x}')}{2}\right) \lambda(\|\boldsymbol{\xi}\|)(\boldsymbol{\xi} \otimes \boldsymbol{\xi}) \left[(\boldsymbol{\xi} \cdot \nabla)\mathbf{u}(\mathbf{x}) + \frac{1}{2}(\boldsymbol{\xi} \cdot \nabla)(\boldsymbol{\xi} \cdot \nabla)\mathbf{u}(\mathbf{x})\right] dV_{\mathbf{x}'} + \mathbf{E}(\mathbf{x}) \\
&= -\mathbf{b}(\mathbf{x}).
\end{aligned} \tag{3.13}$$

The term $\mathbf{E}(\mathbf{x})$ in (3.13) contains higher-order gradients of the displacement field originated in the Taylor expansion (3.4). We assume this term to be negligible; a bound for its magnitude will be provided in Remark 1 below. Reordering terms, we obtain the blending scheme

$$\begin{aligned}
&\int_{\mathscr{B}} \frac{\beta(\mathbf{x}) + \beta(\mathbf{x}')}{2} \lambda(\|\boldsymbol{\xi}\|)(\boldsymbol{\xi} \otimes \boldsymbol{\xi}) \left(\mathbf{u}(\mathbf{x}') - \mathbf{u}(\mathbf{x})\right) dV_{\mathbf{x}'} \\
&+ \left[\int_{\mathscr{B}} \left(1 - \frac{\beta(\mathbf{x}) + \beta(\mathbf{x}')}{2}\right) \lambda(\|\boldsymbol{\xi}\|)\, \xi_i \xi_j \xi_k dV_{\mathbf{x}'}\right] \frac{\partial u_j}{\partial x_k}(\mathbf{x})\, \hat{\mathbf{e}}_i \\
&+ \left[\int_{\mathscr{B}} \left(1 - \frac{\beta(\mathbf{x}) + \beta(\mathbf{x}')}{2}\right) \lambda(\|\boldsymbol{\xi}\|)\, \xi_i \xi_j \xi_k \xi_\ell\, dV_{\mathbf{x}'}\right] \frac{1}{2} \frac{\partial^2 u_j}{\partial x_k \partial x_\ell}(\mathbf{x})\, \hat{\mathbf{e}}_i = -\mathbf{b}(\mathbf{x}).
\end{aligned} \tag{3.14}$$

We observe that for $\mathbf{x} \in \mathscr{B}_{\mathrm{PD}}^{0,\delta}$, Eq. (3.14) reduces to the PD model (3.1), and for $\mathbf{x} \in \mathscr{B}_{\mathrm{CCM}}^{0,\delta}$, Eq. (3.14) reduces to the Navier-Cauchy equation of classical elasticity (3.8).

A model is said to be *patch-test consistent* if homogeneous deformations represent solutions to static problems in that model, in the absence of external loads. We demonstrate now that the blending scheme (3.14) is patch-test consistent. Let $\mathbf{u} = \mathbf{G}\mathbf{x}$ with $\mathbf{G}$ a constant displacement gradient. In this case,

$$\mathbf{u}(\mathbf{x}') - \mathbf{u}(\mathbf{x}) = \mathbf{G}\boldsymbol{\xi} \quad , \quad \frac{\partial u_j}{\partial x_k}(\mathbf{x}) = G_{jk} \quad , \quad \frac{\partial^2 u_j}{\partial x_\ell \partial x_k}(\mathbf{x}) = 0.$$

A direct substitution shows that the blending scheme (3.14) is patch-test consistent.

Remark 1. *The truncation error* $\mathbf{E}(\mathbf{x})$ *in* (3.13) *at* $\mathbf{x} \in \mathscr{B}^{0,\delta}$ *can be bounded, given a PD model with* $\lambda(\|\boldsymbol{\xi}\|) \geqslant 0 \ \ \forall \boldsymbol{\xi} \in \mathbb{R}^d$*, by considering higher-order gradients in the Taylor expansion* (3.4)*, as [55]*

$$\begin{aligned}
\|\mathbf{E}(\mathbf{x})\| \leqslant &\frac{d^6(d+2)}{12} \frac{\Lambda}{3} \Bigg\{ \left[\, \overline{\beta}(\mathbf{x}) - \underline{\beta}(\mathbf{x}) \,\right] \delta \sup_{j,k,\ell,m} \left| \frac{\partial^3 u_j}{\partial x_m \partial x_\ell \partial x_k}(\mathbf{x}) \right| \\
&+ \left[1 - \frac{\beta(\mathbf{x}) + \underline{\beta}(\mathbf{x})}{2}\right] d\, \delta^2 \sup_{\substack{\mathbf{x}' \in \mathscr{H}(\mathbf{x},\delta) \\ j,k,\ell,m,n}} \left| \frac{\partial^4 u_j}{\partial x_n \partial x_m \partial x_\ell \partial x_k}(\mathbf{x}') \right| \Bigg\},
\end{aligned} \tag{3.15}$$

where Λ *is given in* (3.7) *and*

$$\overline{\beta}(\mathbf{x}) := \max_{\mathbf{x}' \in \mathscr{H}(\mathbf{x},\delta)} \beta(\mathbf{x}') \quad , \quad \underline{\beta}(\mathbf{x}) := \min_{\mathbf{x}' \in \mathscr{H}(\mathbf{x},\delta)} \beta(\mathbf{x}').$$

The error estimate (3.15) *provides two pieces of information. First, it bounds the error incurred across transition regions, due to the truncation of the Taylor expansion in* (3.4)*. Second, it quantifies the suitability of the classical local model to describe the material response in the classical region. The first term inside the curly brackets, on the right-hand side of* (3.15)*, only contributes for points* $\mathbf{x}$ *in transition regions for which* $\overline{\beta}(\mathbf{x}) - \underline{\beta}(\mathbf{x}) \neq 0$*. The second term inside those curly brackets, in contrast, may also give a nonzero contribution in the classical region, outside transition regions. However, wherever displacement fields can be approximated by a quadratic profile within the neighborhood of a point, both of these terms are small.*

3.4 A numerical example

We demonstrate numerically the performance of the blended model through a two-dimensional example. Related one-dimensional examples are given in [52], and additional two-dimensional examples can be found in [55]. We look at a square plate with a horizontal rectangular slit at its center under both tensile and shear loading. We assume a PD model given by (3.1) with $\lambda(\|\boldsymbol{\xi}\|) = c/\|\boldsymbol{\xi}\|^3$ and $c = 9E/\pi\delta^3$. Let the square plate be given by $\mathscr{B}_{\text{plate}} = (-\frac{1}{2}, \frac{1}{2}) \times (-\frac{1}{2}, \frac{1}{2})$ and the rectangular slit by $\mathscr{B}_{\text{slit}} = (-\frac{1}{10}, \frac{1}{10}) \times (-\frac{1}{120}, \frac{1}{120})$. The domain of interest is thus $\mathscr{B} = \mathscr{B}_{\text{plate}} \setminus \mathscr{B}_{\text{slit}}$. In this case, the domain has two boundaries: the outer boundary, $\partial\mathscr{B}_{\text{plate}}$, and the inner boundary, $\partial\mathscr{B}_{\text{slit}}$. An illustration is given in Figure 3.1(a). The domain decomposition in the blended problem is illustrated in Figure 3.1(c).

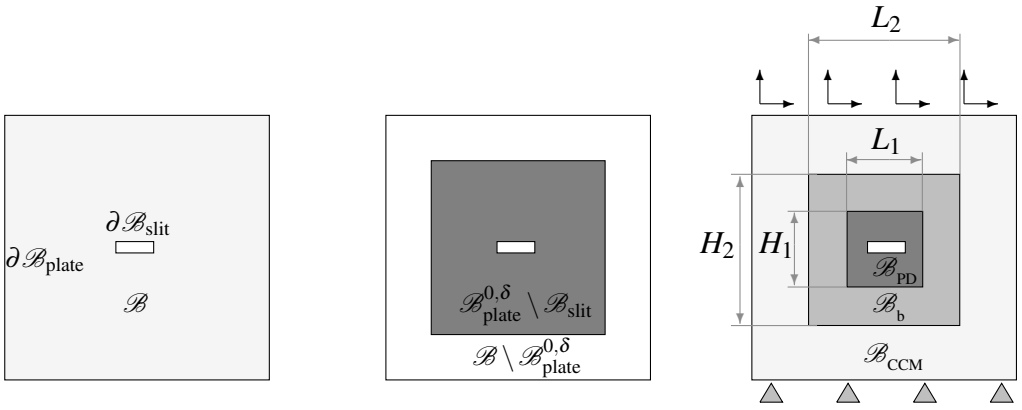

(a) Square plate with rectangular slit (b) PD problem (c) Blended problem

Figure 3.1: (a) Geometry of a square plate with a horizontal rectangular slit. (b) Domain decomposition in the PD problem into the solution domain and the boundary layer. (c) Domain decomposition and boundary conditions in the blended problem.

The boundary conditions in the blended problem combine classical (local) boundary conditions for the outer boundary, given by zero displacements on the bottom edge and $\mathbf{u} = (0.05, 0.05)$

on the top edge, and nonlocal boundary conditions for the inner boundary, given by free-surface conditions. In the PD problem, we also employ free-surface boundary conditions for the inner boundary. To prevent surface effects in the PD problem, and to obtain consistent solutions between the PD and blended problems, we use the numerical solution of the blended problem to impose displacement boundary conditions in the boundary layer $\mathscr{B} \setminus \mathscr{B}^{0,\delta}_{\text{plate}}$, adjacent to the outer boundary (*cf.* Figure 3.1(b)).

We use a meshfree method [63] to discretize the PD model and a combined meshfree/finite-difference approach to discretize the blended model. The blending function is chosen as piecewise constant with $\hat{\beta} = 0.5$ in $\mathscr{B}_{\text{b}}$ (*cf.* (3.9)). The simulation results, using the parameters given in Table 3.1, are presented in Figure 3.2, where deformed configurations are colored using the values of the strain component ε_{xx}. The numerical results demonstrate that the blended model reproduces the solution of the PD model at a reduced computational cost. In this case, the blended simulation achieves a speedup of approximately $11\times$ over the PD simulation. The efficiency of the blended model can be further improved both by model adaptivity techniques, aimed at optimizing the domain decomposition geometry and/or the functional form of the blending function, and by adaptive grid refinement, which can generate a discretization with a fine grid in the PD and transition regions and a coarse grid in the classical region, as demonstrated in [52].

Table 3.1: Parameters for the rectangular slit simulations.

E	δ	Δx	L_1	L_2	H_1	H_2
1	0.05	$1/120$	$1/5+4\delta$	$1/5+6\delta$	$1/60+4\delta$	$1/60+6\delta$

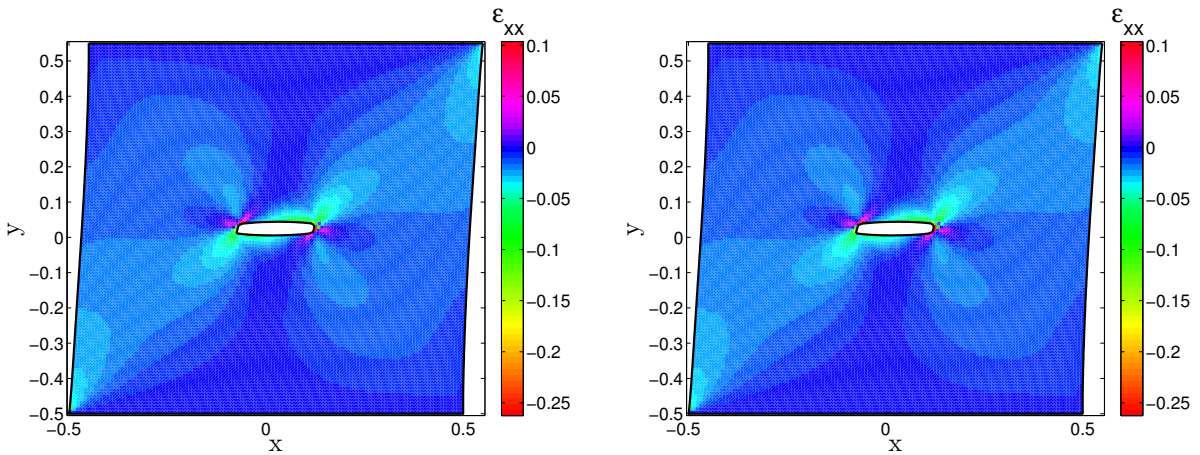

(a) Strain profile for the PD model.

(b) Strain profile for the blended model.

Figure 3.2: Profiles for the strain component ε_{xx} in the deformed configuration.

3.5 Concluding remarks

We derived a blending scheme to concurrently couple bond-based peridynamic and classical elasticity models. The method proposed extends the work done for one-dimensional linear peridynamic models in [52] to bond-based peridynamic models in higher dimensions. For simplicity of exposition, the results here were presented using linear bond-based PD models.

As opposed to other blending methods in the literature, the proposed method derives a blending scheme from a single reference model. As a consequence, spurious effects, common in this type of methods, are not present in this blended model. Specifically, the blended model proposed does not exhibit ghost forces and is patch-test consistent. Numerical simulations demonstrated that the blended model can be used to accurately reproduce solutions of peridynamic problems with great computational savings. In the numerical results presented here, for instance, a speedup of approximately $11\times$ over the PD simulation is achieved by the blended model. Blended models may provide a tool to simulate problems in peridynamics, where fully peridynamic simulations are computationally too expensive, whereas solutions to classical elasticity significantly differ from the peridynamic ones.

The blending scheme here was derived for elastic material models. As a result, peridynamics was coupled to classical elasticity. However, many problems of interest in peridynamics concern not only fracture, but also inelastic behavior. Although blending methods may ensure that regions with discontinuities in displacement fields are contained within a peridynamic subdomain, this may not be the case for inelastic material response. Extensions of the blending scheme proposed to treat problems beyond elasticity, such as those involving plasticity or visco-elasticity/plasticity, are thus required. Furthermore, applications of the blending scheme to time-dependent problems may require additional studies to ensure that no significant wave reflection occurs, across transition regions, in dynamic simulations.

Chapter 4

Position-Aware Peridynamic Constitutive Models

4.1 Introduction to Surface Effects

This chapter discusses progress toward handling surface effects for ordinary peridynamic constitutive models. Without surface correction, discretized models of the peridynamic equations can lead to an inconsistency with local models making this work an especially important aspect of local-nolocal coupling. Under this LDRD, research in this area led to a new class of ordinary peridynamic constitutive models referred to as position aware. A key advance was the development of a position-aware linear solid (PALS) model (Mitchell, Silling and Littlewood) [37]. The PALS model was extended to include linear viscoelasticity (Mitchell) [39] and significant progress was made toward plasticity.

The PALS model is a state-based constitutive model [64] that improves upon the performance of material models currently available in the literature. The primary motivation is the undesirable behavior of certain peridynamic material models in the vicinity of free surfaces. This difficulty appears, for example, in a peridynamic simulation of a uniaxial tension test, using the linear peridynamic solid (LPS) constitutive model and the meshfree discretization approach of Silling and Askari [63]; see Figure 4.1 for schematic/illustration of test. In this simulation, the displacements at the end portions of the bar are prescribed, and the forces on the grips, G_y, are computed, along with the engineering strain in the gauge, ε. The Young's modulus may then be computed as

$$E = \frac{G_y}{A_g \varepsilon},$$

where A_g is the undeformed cross-sectional area of the bar in the vicinity of the gauge. The expected value of Young's modulus is the slope of the green curve in Figure 4.2. Modern three-dimensional finite element codes can accurately reproduce the Young's modulus in a simulation of the uniaxial tension test for a linear elastic material. However, a typical three-dimensional peridynamic simulation using the LPS material model predicts the red curve in Figure 4.2. The difference in slope between the two curves shows that the peridynamic model under-predicts the load on the grips for a given value of strain. The LPS material parameters are calibrated for points in the interior of a body and do not take into account whether a point is near a boundary [64]. Due to the nonlocality of the peridynamic equations, the LPS material model becomes inaccurate

at points near a free surface. Here, some of the peridynamic bonds that would be present in the interior are missing (Figure 4.3). Because bonds are missing, they do not contribute to the net force on the cross-section of the gauge, hence the total force is under-predicted. While this effect manifests for a number of constitutive models, it it not present for all models; correspondence models are an exception because missing bonds are compensated for by the shape tensor K.

The under-prediction of force at material points near a free surface is often referred to as the *surface effect* in peridynamics. This effect presents a practical difficulty in applying bond-based models and ordinary state-based models such as the LPS. Approaches for mitigating the surface effect have been proposed by Kikic, Macek and Silling, and Mitchell. Following a bond-based approach, Kilic [28] proposed a position-aware correction that is computed iteratively for each material point. Macek and Silling [35] developed a position-aware force normalization that scales the stiffness of points near a surface using a ratio of eigenvalues from local 3×3 stiffness matrices, where eigenvalues are computed (with the same material properties) for points near a free surface and on the interior. Mitchell [38] developed a position-aware scaling of moduli for the LPS model, but its efficacy was found to be somewhat sensitive to complex surface geometries.

The peridynamic theory of solid mechanics allows for great flexibility in the development of constitutive models. In contrast to classical, local models, which rely on a kinematic description of material deformation at a point such as the deformation gradient, material models in the peridynamic theory determine pairwise force densities based on the deformations of a nonlocal family of neighboring material points [61, 65, 36]. This enrichment of kinematic information greatly expands the range of possible constitutive laws. Peridynamic material models developed to date fall into one of three categories: bond-based, ordinary state-based, and non-ordinary state-based. Bond-based peridynamic models determine the pairwise force density that acts between two material points based only on the histories of those points (*e.g.*, initial and current positions). The prototype micro-elastic brittle material model was the first peridynamic constitutive law to appear in the literature [61]. This model served as the foundation for a subsequently developed bond-based plasticity model [35]. The state-based theory for peridynamic constitutive models represents a significant generalization of the bond-based approach [64]. The theory of peridynamic states allows for constitutive models in which pairwise force densities are functions of not only the material points in question, but also the full set of material points within the nonlocal neighborhoods of those material points. State-based constitutive models in which pairwise force densities act in the direction of the corresponding bond in the deformed configuration are referred to as *ordinary* state-based models. Examples include the linear peridynamic solid (LPS) [64] and the plasticity and viscoelasticity models developed by Mitchell [41, 40]. The third class of material models, non-ordinary state-based, is comprised of constitutive models in which pairwise force densities are not restricted to act in the bond direction. The correspondence model approach, in which classical (local) constitutive models are adapted for use within peridynamics, falls into this category [64, 24, 71].

The PALS model is an alternative approach to peridynamic constitutive modeling in which model parameters at a point reflect the point's location within the body, removing the need for auxiliary surface correction techniques. This position-aware approach is a significant departure from previously developed constitutive models in that the constitutive model parameters are linked

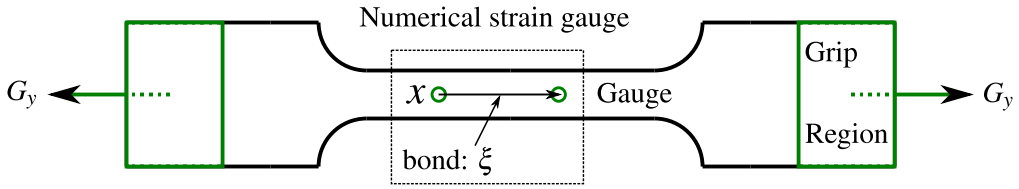

Figure 4.1: Uniaxial tension test schematic.

directly with the geometry of the body. The position-aware linear solid (PALS) model presented herein is an extension of the LPS model that substantially reduces the surface effect. This is accomplished by introducing influence functions that are calibrated according to the bulk elastic properties at each material point, resulting in influence functions that differ for points near a free surface and points on the interior of the body. Identification of the influence functions for each point in the body is accomplished by solving a constrained minimization problem. Determination of the influence functions within a computational simulation does not require an iterative process and is instead achieved through the solution of a linear system of equations.

The PALS approach is unique with respect to the construction and use of position-aware influence functions. As very recently pointed out by Bessa, Foster, Belytschko, and Liu [8], only constant valued influence functions have been studied. Apparently, the two exceptions are the study by Seleson and Parks [59], and the approach for incorporating classical damage models into state-based peridynamics by Tupek, Rimoli, and Radovitzky [72]. Seleson and Parks [59] used influence functions to establish relationships between bond-based and state based peridynamics models and did not consider position-aware influence functions. Influence functions developed by Tupek et al. [72] are a product of a Gaussian and a binary valued function (0 or 1) depending upon the state of damage between two points defining a bond; this is a position aware concept but is not contextually related to the position aware concepts discussed here.

4.2 PALS Model

This section introduces the PALS model, including the elastic energy density, the scalar force state, and construction of position aware influence functions; all of these elements are key aspects of the PALS model. For a full accounting of the details, see [37].

The peridynamic theory of solid mechanics [61, 64, 65] is an extension of classical continuum mechanics theory [13]. The peridynamics extension permits discontinuities in displacements by replacing the stress divergence in the momentum equation with a volume integral

$$\rho(\mathbf{x})\ddot{\mathbf{y}}(\mathbf{x},t) = \int_{\mathscr{B}} \mathbf{f}(\mathbf{x}',\mathbf{x},t)\mathrm{d}V_{\mathbf{x}'} + \mathbf{b}(\mathbf{x},t), \tag{4.1}$$

where $\mathbf{y}(x)$ is the current position vector of a material point $\mathbf{x}$ at time t, ρ is mass density in the undeformed body $\mathscr{B}$, $\mathbf{f}$ is a pairwise bond force density per unit volume, $\mathbf{b}$ is the usual body force density, and $\mathbf{x}'$ is an arbitrary material point within the neighborhood $\mathscr{H}_{\mathbf{x}}$ of the point $\mathbf{x}$.

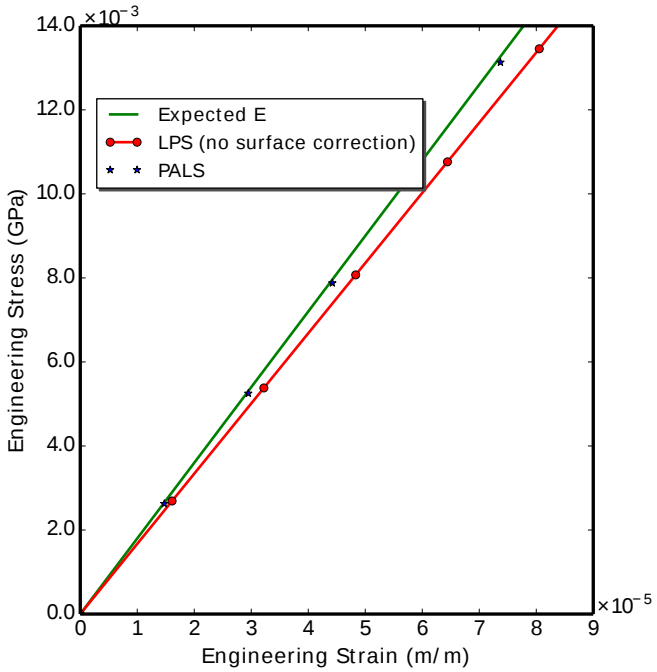

Figure 4.2: Stress-strain curve for a full 3D peridynamic model of the uniaxial tension test with PALS and LPS, both on the same discretization.

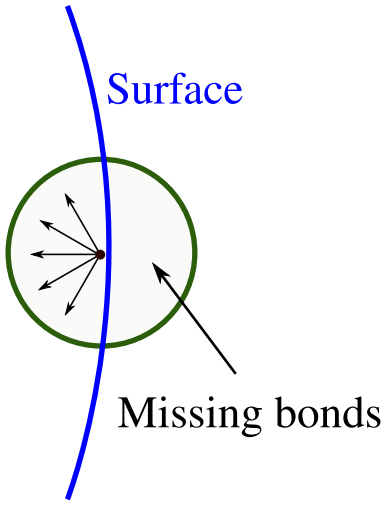

Figure 4.3: Schematic of missing peridynamic bonds.

A *bond* vector is defined by

$$\xi = \mathbf{x}' - \mathbf{x}, \qquad 0 < |\boldsymbol{\xi}| \leq \delta,$$

where δ is the *horizon* of the material. Conceptually, δ is a relevant length scale and defines a spherical neighborhood $\mathscr{H}_{\mathbf{x}}$; it represents the maximum distance for nonlocal interactions in the material model. Material points within the neighborhood $\mathscr{H}_{\mathbf{x}}$ are referred to as the *family* of $\mathbf{x}$. It will be assumed throughout this chapter that δ is independent of $\mathbf{x}$.

The deformed image of a bond $\boldsymbol{\xi} = \mathbf{x}' - \mathbf{x}$ is given by the *deformation state* $\underline{\mathbf{Y}}$:

$$\begin{aligned} \underline{\mathbf{Y}}[\mathbf{x},t]\langle\boldsymbol{\xi}\rangle &= \mathbf{y}(\mathbf{x}',t) - \mathbf{y}(\mathbf{x},t) \\ &= (\mathbf{x}' + \mathbf{u}(\mathbf{x}',t)) - (\mathbf{x} + \mathbf{u}(\mathbf{x},t)), \end{aligned} \tag{4.2}$$

where $\mathbf{u}$ is the displacement field. Further information on peridynamic states is given in [64].

The following scalar states are useful in material modeling:

- The *undeformed bond length state* $\underline{x}$:

$$\underline{x}\langle\boldsymbol{\xi}\rangle = |\boldsymbol{\xi}|.$$

- The *deformed bond length state* $|\underline{\mathbf{Y}}|$:

$$|\underline{\mathbf{Y}}|\langle\boldsymbol{\xi}\rangle = |\underline{\mathbf{Y}}\langle\boldsymbol{\xi}\rangle|. \tag{4.3}$$

- The *extension state* $\underline{e}$:

$$\underline{e}\langle\boldsymbol{\xi}\rangle = |\underline{\mathbf{Y}}|\langle\xi\rangle - \underline{x}\langle\boldsymbol{\xi}\rangle. \tag{4.4}$$

In this chapter, scalar states are underlined and written using italics, such as $\underline{e}$; vector states are written **using bold** and underlined, as in $\underline{\mathbf{Y}}$. The *dot product* of two scalar states $\underline{a}$ and $\underline{b}$ is defined by

$$\underline{a} \bullet \underline{b} = \int_{\mathscr{H}_{\mathbf{x}}} \underline{a}\langle\boldsymbol{\xi}\rangle \, \underline{b}\langle\boldsymbol{\xi}\rangle \, dV_{\boldsymbol{\xi}}.$$

Using the above quantities and definitions, the *deviatoric extension state* $\underline{\varepsilon}$ is constructed as

$$\underline{\varepsilon} = \underline{e} - \frac{\theta \underline{x}}{D}, \tag{4.5}$$

where θ is a scalar called the dilatation (see 4.10 below). below).

This chapter is concerned with state-based constitutive models in which the pairwise bond force density per unit volume $\mathbf{f}(\mathbf{x}',\mathbf{x},t)$ in (4.1) is given by

$$\mathbf{f}(\mathbf{x}',\mathbf{x},t) = \underline{\mathbf{T}}[\mathbf{x},t]\langle\mathbf{x}' - \mathbf{x}\rangle - \underline{\mathbf{T}}[\mathbf{x}',t]\langle\mathbf{x} - \mathbf{x}'\rangle. \tag{4.6}$$

The vector state $\underline{\mathbf{T}}[\mathbf{x}]$ is called the *force state*. In (4.6), $\mathbf{f}$ contains contributions from the force states at both $\mathbf{x}$ and $\mathbf{x}'$ (that is, both $\underline{\mathbf{T}}[\mathbf{x},t]$ and $\underline{\mathbf{T}}[\mathbf{x}',t]$).

In *ordinary* state-based constitutive models, the vector force state is always parallel to the deformed bond vector and written as

$$\underline{\mathbf{T}}\langle\boldsymbol{\xi}\rangle = \underline{t}\langle\boldsymbol{\xi}\rangle\underline{\mathbf{M}}\langle\boldsymbol{\xi}\rangle, \tag{4.7}$$

where $\underline{t}$ is a scalar state called the *scalar force state*, and $\underline{\mathbf{M}}$ is a vector state that produces unit vectors parallel to the deformed bond:

$$\underline{\mathbf{M}}\langle\boldsymbol{\xi}\rangle = \frac{\underline{\mathbf{Y}}\langle\boldsymbol{\xi}\rangle}{|\underline{\mathbf{Y}}|\langle\boldsymbol{\xi}\rangle}. \tag{4.8}$$

The *scalar force state* for the PALS model is derived from an elastic energy density functional defined at a point $\mathbf{x}$ as

$$W(\theta,\underline{\varepsilon}) = \frac{\kappa\theta^2}{2} + \mu(\underline{\sigma\varepsilon}) \bullet \underline{\varepsilon}, \tag{4.9}$$

where μ is the shear modulus and $\underline{\varepsilon}$ is defined in (4.5); $\underline{\sigma}$ is a called the *deviatoric* influence function; the dilatation θ is defined using the extension state $\underline{e}$

$$\theta = (\underline{\omega x}) \bullet \underline{e}, \tag{4.10}$$

where $\underline{\omega}$ is an influence function and normalized such that the weighted volume m used in the LPS is not needed (that is, $m = 3$). The scalar force state $\underline{t}$ is found by taking the Fréchet derivative of W with respect to $\underline{e}$ and is given by

$$\underline{t} = \left(\kappa\theta - \frac{2\mu}{3}(\underline{\sigma x}) \bullet \underline{\varepsilon}\right)\underline{\omega x} + 2\mu\underline{\sigma\varepsilon}. \tag{4.11}$$

Note that the PALS model uses two influence functions $\underline{\omega}$ and $\underline{\sigma}$, both of which are computed and largely depend upon proximity to a surface – hence the name position-aware; relative to the LPS model, they are conceptually a new approach to constitutive modeling. Details for computation of $\underline{\omega}$ and $\underline{\sigma}$ can be found in the PALS model paper [37].

4.3 A Position Aware Viscoelastic (PAV́E) Model

This section introduces and discusses elements of the isotropic viscoelastic model [40] extended to include the position-aware concepts presented in Section 4.2; the new model is called PAV́E [39]; for additional details, see the aforementioned references and the PALS model paper [37].

Extending PALS concepts to viscoelasticity begins with writing the elastic energy density functional

$$W(\theta,\underline{\varepsilon}) = \frac{\kappa\theta^2}{2} + \mu_\infty(\underline{\sigma\varepsilon}) \bullet \underline{\varepsilon} + \sum_i \mu_i(\underline{\varepsilon} - \underline{\varepsilon}^i)\underline{\sigma} \bullet (\underline{\varepsilon} - \underline{\varepsilon}^i), \tag{4.12}$$

where $\underline{\varepsilon}^i$ is an inelastic extension state. The sum over i includes an arbitrary number of Maxwell models (see Figure 4.4) in parallel with the peridynamics standard linear solid (see Figure 4.5). Shear moduli are denoted by μ_∞ and μ_i; a time constant $\tau_i = \frac{\eta_i}{\mu_i}$ is defined for the i^{th} mechanism.

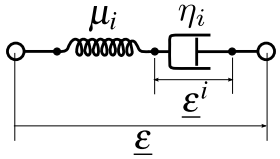

Figure 4.4: Maxwell model.

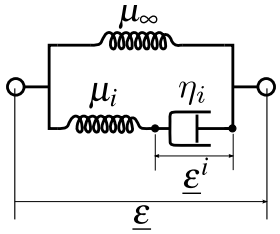

Figure 4.5: Standard linear solid.

The extension states $\underline{\varepsilon}^i$ are governed by an evolution equation that ultimately must be evolved forward in time for each bond; this equation is given by

$$\dot{\underline{\varepsilon}}^i\langle\xi\rangle + \frac{1}{\tau_i}\underline{\varepsilon}^i\langle\xi\rangle = \underline{\varepsilon}\langle\xi\rangle(t), \tag{4.13}$$

where the brackets $\langle\xi\rangle$ emphasize the evolution of the in-elastic extension state on each bond ξ.

The scalar force state $\underline{t}$ is given by

$$\underline{t} = p\underline{\omega x} + 2\mu_\infty\underline{\sigma\varepsilon} + 2\sum_i \mu_i\underline{\sigma}(\underline{\varepsilon} - \underline{\varepsilon}^i), \tag{4.14}$$

where the PALS pressure p is defined by

$$p = \kappa\theta - \frac{2\mu_\infty}{3}\underline{\sigma\varepsilon}\bullet\underline{x} - \sum_i \frac{2\mu_i}{3}\underline{\sigma}(\underline{\varepsilon} - \underline{\varepsilon}^i)\bullet\underline{x}. \tag{4.15}$$

Influence functions $\underline{\omega}$ and $\underline{\sigma}$ are computed as in the PALS model; time integration of this model is implemented indentically to the original viscoelasticity model [40].

4.4 Demonstration calculations

Two demonstration calculations are provided here – one each for the PALS and PAVE models. The first calculation demonstrates the efficacy of the PALS approach for surface correction; the second calculation uses the PAVE model and hence demonstrates both the visocelasticity model and the position-aware approach to surface correction. Additional demonstration calculations can be found in the PALS model paper [37] and the peridynamics viscoelasticity model report [40].

The simulations were carried out using the *Peridigm* [46, 48] code following the meshfree method of Silling and Askari [63]. All demonstration calculations are three-dimensional and results were obtained by solving the momentum equation under conditions of static equilibrium. The

Cubit code [17] was utilized to generate the discretization, and the *Paraview* code [44] was used for visualization of results. For further discussion of the numerical solution procedure, see Silling and Askari [63] and Littlewood [32].

4.4.1 Tension test

As a demonstration, the PALS model is applied to the motivation problem described in Section 4.1 (see Figure 4.1). A full three-dimensional model of the specimen was used. Improved accuracy in reproducing E using the PALS model, compared with the LPS model, is shown in Figure 4.2.

4.4.2 Simple shear

The simple shear calculation presented in Figures 4.6 and 4.7 is particularly effective at demonstrating the efficacy (or lack thereof) of correctly calculating energy density for homogeneous shear deformations at points near the surface of an ordinary isotropic peridynamic body. A schematic of the problem is shown in Figure 4.6 and a calculation of the elastic energy density as a function of time for both the PALS model and the PAV́E model is shown in Figure 4.7. Note that there are three calculations for the PAV́E model – one each for the PAV́E model parameters $\lambda = .01, .50, .99$; these parameters refer to the peridynamics standard linear solid (SLS) model [40]. For the peridynamics SLS model, $\mu_\infty = (1-\lambda)\mu$, and $\mu_1 = \lambda\mu$, where μ is the shear modulus of the material. For these calculations, and the calculations in the following section, a time constant $\tau_1 = 2$ seconds was used. Note that PAV́E reduces to the PALS model and elastic behavior as $\lambda \to 0$ and takes on a fully viscoelastic character as $\lambda \to 1.0$. The graphic on the left in Figure 4.7 illustrates the uniformity of energy density as calculated by the PALS model – this is the expected value which can be hand calculated based upon the local theory; although there are distinct colors illustrated on the mesh, the color bar shows that values are essentially constant (within 4 significant digits) across the $7 \times 7 \times 7$ mesh of points.

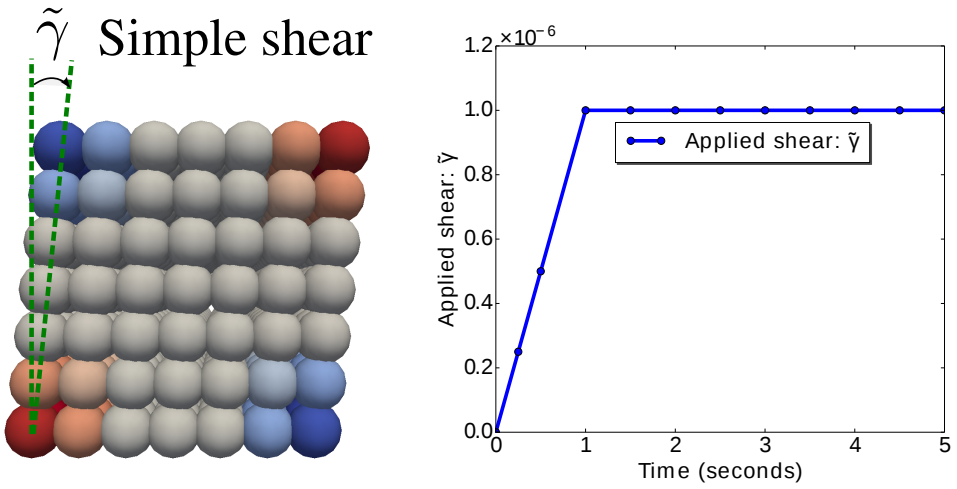

Figure 4.6: Simple shear schematic.

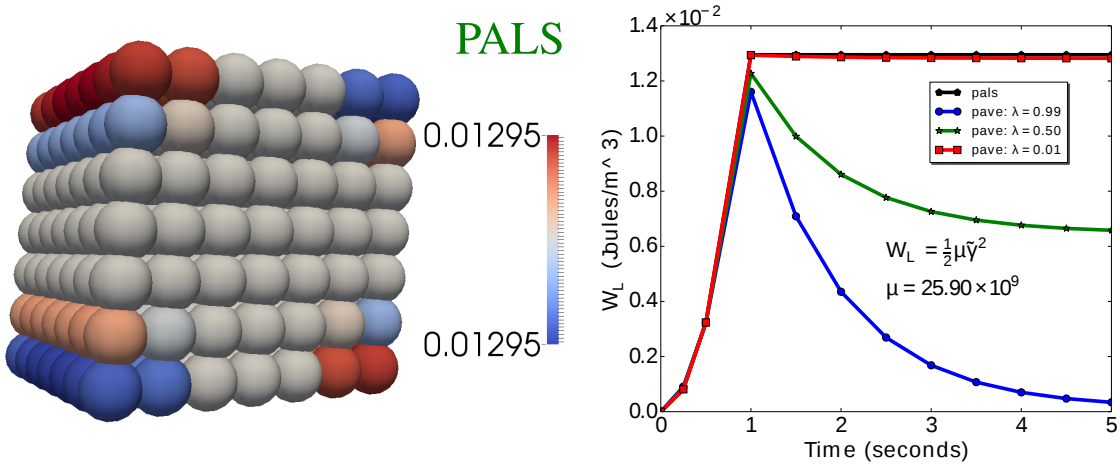

Figure 4.7: PALS and PAVE simple shear calculation.

Chapter 5

Convergence of Peridynamic Models

5.1 Introduction

Peridynamics is based on integro-differential equations, where spatial integration is employed to compute the contribution of internal forces in a body to the material response. Since governing equations in peridynamics are continuum models, they can be discretized in many ways [20]. Different discretization methods differ in software complexity, computational time and memory requirements, and accuracy and convergence of numerical solutions. A proper discretization choice may avoid polluting coupled local/nonlocal simulations with unnecessary discretization errors and convergence issues. We thus investigate methods to improve current discretizations of peridynamic models. A simple particle-based discretization for the strong form of peridynamic equations was introduced in [63], where a set of nodes with known volume in a reference configuration was utilized to discretize given domains. This discretization method is meshfree, because no elements or geometrical connections between nodes are used. This meshfree approach is the most widely used discretization method in engineering peridynamic simulations to date, due to its implementation simplicity and relatively low computational cost, in comparison to other discretization methods. As an example, finite element discretizations of governing equations are based on weak forms, which for peridynamic equations double the number of spatial dimensions that need to be discretized [15]. In peridynamics, each material point is assumed to directly interact with a surrounding neighborhood, and the interaction is computed through spatial integration. In meshfree discretizations, integrals in peridynamic equations are converted into weighted sums. In [63], summation weights are taken as nodal volumes.

The accuracy and convergence of the above-mentioned meshfree discretization depends on the choice of summation weights. It is common to take those weights as approximations of the volumes of the intersections between the neighborhood of a given node and the material regions or *cells* defining the nodal volumes of surrounding nodes [51]. For surrounding nodes near the boundary of the neighborhood of a given node, only a partial overlapping may exist between their cells and that neighborhood. In those cases, we refer to the volume of the corresponding intersection as a *partial volume*. Computing partial volumes requires, in general, highly complex geometrical calculations. For instance, partial volume calculations in meshfree discretizations of peridynamic equations with a set of nodes along a cubic grid, require the computation of intersections between a ball and arbitrary cubes. Algorithms for approximations of partial volumes appear in [47, 45, 9, 76]. In two or one dimensions, corresponding "partial volumes" are referred to as *partial areas*

or *partial lengths*, respectively. In [51], analytical calculations of partial areas for sets of nodes along a square grid were derived, resulting in improved accuracy and convergence of numerical integrations, for different peridynamic quantities of interest. Unless specified otherwise, we will use the term *partial volume* in a general sense, to refer to a partial volume, to a partial area, or to a partial length, in 3D, 2D, or 1D, respectively.

An alternative way to improve numerical integrations in peridynamics is to employ kernels which decay to zero at the boundary of the neighborhood of a given node. The idea behind this method is to reduce the contribution to the numerical integration of neighboring nodes near the boundary of the neighborhood of a given node, mitigating the discretization error induced by the inaccuracy of the approximation of partial volumes. This idea was briefly mentioned in [76] and implemented in [51], employing smooth influence functions with a finite support. Numerical studies in [51] suggested that this method could provide a means to improve the accuracy and convergence of numerical integrations in peridynamics.

We present here convergence studies of numerical solutions of static peridynamic problems, in all three dimensions, using meshfree discretizations. The material here is based on the work presented in [56]. We compute analytically partial lengths in 1D and partial areas in 2D, following [51]. In 3D, we estimate numerically partial volumes through a combined strategy of recursive subdivision and sampling. We also investigate the use of smooth influence functions with a finite support to improve the accuracy and convergence of numerical solutions in peridynamics.

5.2 The meshfree discretization of peridynamic models

Given a body $\mathscr{B} \subset \mathbb{R}^d$, $d = 1, 2$, or 3, the peridynamic (PD) equation of motion for a material point $\mathbf{x} \in \mathscr{B}$ at time $t \geqslant 0$ is

$$\rho(\mathbf{x}) \frac{\partial^2 \mathbf{u}}{\partial t^2}(\mathbf{x}, t) = \int_{\mathscr{B}} \left\{ \underline{\mathbf{T}}[\mathbf{x}, t] \langle \mathbf{x}' - \mathbf{x} \rangle - \underline{\mathbf{T}}[\mathbf{x}', t] \langle \mathbf{x} - \mathbf{x}' \rangle \right\} dV_{\mathbf{x}'} + \mathbf{b}(\mathbf{x}, t), \tag{5.1}$$

where ρ is the mass density, $\mathbf{u}$ is the displacement field, $\mathbf{b}$ is a prescribed body force density field, and $\underline{\mathbf{T}}$ is the *force state field* [64]. In PD, it is common to assume that a material point $\mathbf{x} \in \mathscr{B}$ interacts directly only with other material points within its *neighborhood*,

$$\mathscr{H}(\mathbf{x}, \delta) := \left\{ \mathbf{x}' \in \mathbb{R}^d : \|\mathbf{x}' - \mathbf{x}\| \leqslant \delta \right\}, \tag{5.2}$$

which represents a closed ball, disk, or line segment in 3D, 2D, or 1D, respectively, centered at $\mathbf{x}$, where δ is a length scale called the *PD horizon*. As a consequence,

$$\underline{\mathbf{T}}[\mathbf{x}, t] \langle \mathbf{x}' - \mathbf{x} \rangle = \mathbf{0} \quad \forall \mathbf{x}' \notin \mathscr{H}(\mathbf{x}, \delta). \tag{5.3}$$

For a static problem, the PD equilibrium equation is written as

$$-\int_{\mathscr{B}} \left\{ \underline{\mathbf{T}}[\mathbf{x}] \langle \mathbf{x}' - \mathbf{x} \rangle - \underline{\mathbf{T}}[\mathbf{x}'] \langle \mathbf{x} - \mathbf{x}' \rangle \right\} dV_{\mathbf{x}'} = \mathbf{b}(\mathbf{x}). \tag{5.4}$$

Let $\mathscr{L}_{\mathscr{B}}$ be a set of nodes discretizing the body $\mathscr{B}$ and let τ_k be a material region or *cell* represented by the node k. We assume that cells form a tessellation of the body, so that $\bigcup_k \overline{\tau_k} = \overline{\mathscr{B}}$ and $\tau_k \cap \tau_\ell = \emptyset$ for $k \neq \ell$. In meshfree discretizations of PD equations, one can take the dynamics of the node k as representative of the evolution of the entire cell τ_k. Following derivations in [56], a discretization of (5.1) can be written as

$$\rho_i \frac{d^2\mathbf{u}_i}{dt^2} = \sum_{j \in \mathscr{F}_i} \left\{ \underline{\mathbf{T}}[\mathbf{x}_i, t]\langle \mathbf{x}_j - \mathbf{x}_i \rangle - \underline{\mathbf{T}}[\mathbf{x}_j, t]\langle \mathbf{x}_i - \mathbf{x}_j \rangle \right\} V_j^{(i)} + \mathbf{b}_i, \tag{5.5}$$

where $\rho_i := \rho(\mathbf{x}_i)$, $\mathbf{u}_i := \mathbf{u}(\mathbf{x}_i, t)$, $\mathbf{b}_i := \mathbf{b}(\mathbf{x}_i, t)$, $\mathbf{x}_j$ is the reference position of the node i, $V_j^{(i)}$ is a quadrature weight, and $\mathscr{F}_i$ is the *family of* i, representing the set of all nodes in $\mathscr{L}_{\mathscr{B}}$ interacting with the node i. We take the quadrature weight $V_j^{(i)}$ as an approximation to the volume (in 3D), area (in 2D), or length (in 1D) of the intersection between the cell τ_j and the neighborhood of $\mathbf{x}_i$ [51]. For a node j with a cell inside the neighborhood of $\mathbf{x}_i$, $V_j^{(i)}$ is taken as the full nodal volume; for a node j near the boundary of the neighborhood of $\mathbf{x}_i$, however, $V_j^{(i)}$ is taken as a partial volume. Further details regarding $\mathscr{F}_i$ and $V_j^{(i)}$ are provided in Section 5.2.1 below.

Remark 2. *To accurately compute partial volumes, a reference mesh needs to be generated. In dynamic simulations, partial volumes can be pre-computed and stored per bond, and the mesh discarded afterwards. Consequently, the discretization approach in* (5.5) *can be still referred to as "meshfree".*

5.2.1 Algorithms for the computation of partial volumes

We review three algorithms from the literature for the computation of partial volumes. These algorithms assume a uniform grid with grid spacing h.

Algorithm FL, FA, FV (1D, 2D, 3D). The first algorithm was proposed in [63] as a simple algorithm with

$$\mathscr{F}_i = \{ j \neq i : \mathbf{x}_j \in \mathscr{B} \,;\, \|\mathbf{x}_j - \mathbf{x}_i\| \leqslant \delta \} \tag{5.6}$$

and the partial volumes approximated as full nodal volumes. We refer to this algorithm as FL (in 1D), FA (in 2D), or FV (in 3D), where "FL", "FA", and "FV" stand for *Full Length*, *Full Area*, and *Full Volume*, respectively.

Algorithm PL-PDLAMMPS, PA-PDLAMMPS, PV-PDLAMMPS (1D, 2D, 3D). The second algorithm appeared in [47, 45]. This algorithm uses the same definition (5.6) for the family of i, but modifies the computation of partial volumes as follows: If $\|\boldsymbol{\xi}\| + \frac{h}{2} > \delta$, then $V_j^{(i)} = \frac{1}{h}\left[\delta - \left(\|\boldsymbol{\xi}\| - \frac{h}{2}\right)\right] V_j$ with V_j the nodal volume of the node j. We refer to this algorithm as PL-PDLAMMPS (in 1D), PA-PDLAMMPS (in 2D), or PV-PDLAMMPS (in 3D), where "PL", "PA", and "PV" stand for *Partial Length*, *Partial Area*, and *Partial Volume*, respectively, and PDLAMMPS is the name of a PD software [47].

Algorithm PL-HHB, PA-HHB, PV-HHB (1D, 2D, 3D). The third algorithm, presented in [27, 9], extends the family of i in (5.6) as

$$\mathscr{F}_i = \{ j \neq i : \mathbf{x}_j \in \mathscr{B} \,;\, \|\mathbf{x}_j - \mathbf{x}_i\| - \tfrac{h}{2} \leqslant \delta \}. \tag{5.7}$$

Note that the family of i in (5.7) may include nodes j such that $\|\mathbf{x}_j - \mathbf{x}_i\| > \delta$. For such nodes, the force state vanishes (*cf.* (5.3)). In that case, we relax the restriction (5.3) to allow for a non-zero force state, even when it operates on a bond of length larger than δ. The same correction for partial volumes as in the second algorithm is used. We refer to this algorithm as PL-HHB (in 1D), PA-HHB (in 2D), or PV-HHB (in 3D), where "HHB" refers to the initials of the authors of [27]: Hu, Ha, and Bobaru.

5.2.2 Influence functions in peridynamics

Influence functions are scalar-valued functions commonly used to determine the support of force states. These functions have been introduced in [64] and their role in PD has been studied in [59]. In [51], it was demonstrated that employing smooth influence functions with a finite support mitigates the integration inaccuracy caused by neighboring nodes near the boundary of the neighborhood of a given node. We employ influence functions of the form

$$\omega(\|\boldsymbol{\xi}\|) = \begin{cases} \frac{P_n(\|\boldsymbol{\xi}\|)}{\|\boldsymbol{\xi}\|^\alpha} & \|\boldsymbol{\xi}\| \leqslant \delta, \\ 0 & \text{else}, \end{cases} \tag{5.8}$$

where $\alpha = 0, 1$ is a model parameter and $P_n(r)$ is a polynomial of order $n \in \mathbb{N}_0$, satisfying $P_n(0) = 1$ and $P_n(\delta) = 0$ for $n > 0$, and $P_n'(r) = P_n''(r) = \ldots = P_n^{(k)}(r) = 0$ at $r = 0, \delta$ with $k = (n-1)/2$ for $n > 1$. In Figure 5.1, we plot the different influence functions, in a one-dimensional system, for each of the above polynomial choices.

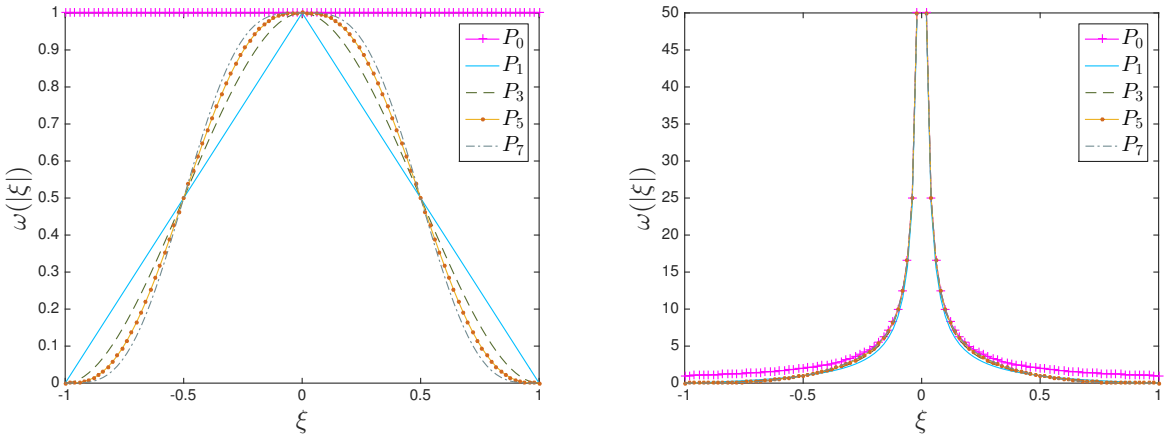

(a) $\alpha = 0$. (b) $\alpha = 1$.

Figure 5.1: Influence functions in one dimension for (a) $\alpha = 0$ and (b) $\alpha = 1$, with different choices of polynomial $P_n(r)$ (*cf.* (5.8)) and $\delta = 1$.

5.3 A one-dimensional peridynamic problem

Let a linear bond-based PD model be given (in 1D) by the force state

$$\underline{\mathrm{T}}[x,t]\langle\xi\rangle = \frac{1}{2} c\, \omega(|\xi|)(u(x+\xi,t)-u(x,t)),$$

and let a one-dimensional static PD problem be

$$\begin{cases} -\displaystyle\int_{x-\delta}^{x+\delta} c\, \omega(|x'-x|)(u(x')-u(x))dx' = b(x), & x \in \mathscr{B}, \quad (5.9a) \\ u(x) = g(x), & x \in \overline{\overline{\mathscr{B}}} \setminus \mathscr{B}, \quad (5.9b) \end{cases}$$

where c is a constitutive constant, ω is an influence function, and g is a given function providing displacement boundary conditions. We choose the computational domain as a unit line segment: $\overline{\overline{\mathscr{B}}} = [0,1]$ and the inner domain as $\mathscr{B} = (\delta, 1-\delta)$. Displacement boundary conditions are imposed in the boundary layer $\overline{\overline{\mathscr{B}}} \setminus \mathscr{B}$. An illustration is given in Figure 5.2.

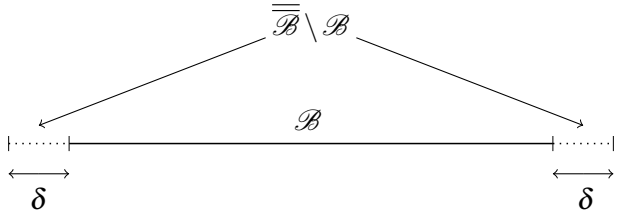

Figure 5.2: One-dimensional domain $\overline{\overline{\mathscr{B}}}$ composed of two non-overlapping subdomains: the inner domain $\mathscr{B}$ and the boundary layer $\overline{\overline{\mathscr{B}}} \setminus \mathscr{B}$.

The PD constant c is chosen using a connection between the PD equation (5.9a) and the classical (local) equation

$$-K\frac{d^2u}{dx^2}(x) = b(x) \tag{5.10}$$

with K a constant, assuming quadratic displacement field, as

$$c = \frac{2K}{m}, \tag{5.11}$$

where m is the weighted volume (*cf.* (5.18)) in 1D:

$$m = \int_{-\delta}^{\delta} \omega(|\xi|)\xi^2 d\xi. \tag{5.12}$$

We assume a one-dimensional static PD problem given by (5.9) with $K = 1$, $\delta = 0.04$, $b = -2$, and $g(x) = x^2$. The value of b is found using the method of manufactured solutions, to ensure consistency with the imposed boundary conditions. We discretize the problem with the discretization scheme (5.5).

We investigate the convergence of numerical solutions of Problem (5.9). We compute the PD constant c by (5.11) with $K = 1$. The convergence study is performed as follows: we choose an initial number of computational nodes $N = 75$ ($\delta/h = 3$) and gradually increase this number by one until we reach $N = 150$ ($\delta/h = 6$). We compare the algorithm FL in combination with different influence functions with the algorithms PL-PDLAMMPS and PL-HHB. Unless specified otherwise, it is assumed that a given algorithm is used in combination with an influence function with $P_0(r)$. We would like to compare the effect obtained by improving the computation of partial lengths with the one obtained by using influence functions with increasing regularity. The convergence results for different algorithms and influence functions are presented in Figure 5.3 for (a) $\alpha = 0$ and (b) $\alpha = 1$, where the error in the numerical solution is computed using an L^2-norm.

We conclude that using the algorithm PL-HHB or the algorithm FL in combination with a smooth influence function, improves the accuracy of the numerical solutions, for most grid spacings, in comparison to utilizing the algorithms FL or PL-PDLAMMPS. The quality of the convergence results for the algorithm PL-PDLAMMPS is as poor as for the algorithm FL. Using the algorithm FL in combination with an influence function with $P_5(r)$ (PWQ) or $P_7(r)$ (PWS) gives an asymptotic convergence rate of $r \approx 1.00$ for $\alpha = 0$, while resulting in convergence rates with values $r > 1$ for $\alpha = 1$. The convergence profile obtained with the algorithm PL-HHB, in contrast, is oscillatory; however, the amplitude of its oscillation is significantly smaller than the one observed with the algorithms FL and PL-PDLAMMPS.

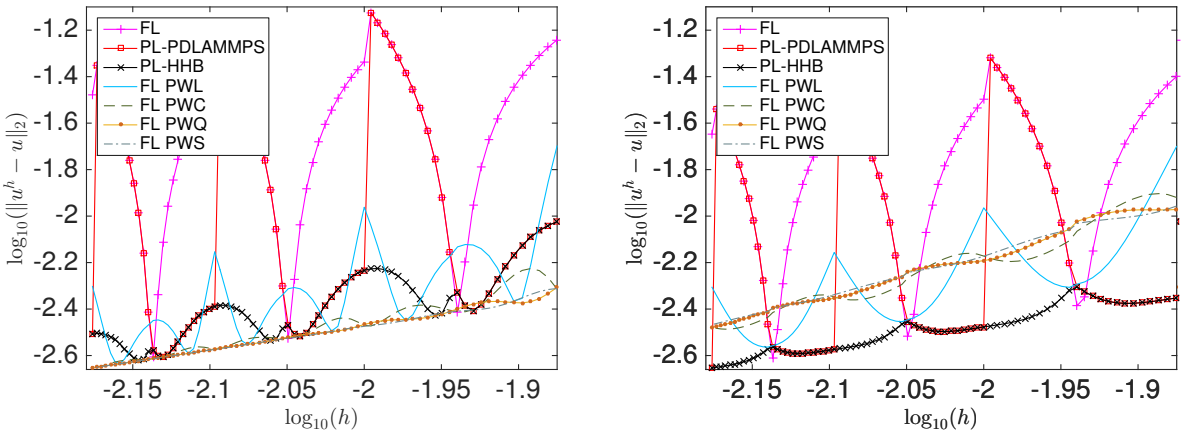

(a) $\alpha = 0$. (b) $\alpha = 1$.

Figure 5.3: Convergence of the numerical solution of Problem (5.9) using different algorithms for approximation of partial lengths and different influence functions. The notation PWL, PWC, PWQ, and PWS refers, respectively, to the choice of influence function with polynomial $P_1(r)$, $P_3(r)$, $P_5(r)$, and $P_7(r)$.

5.4 A two-dimensional peridynamic problem

Let a linear bond-based PD model be given by the force state

$$\underline{\mathbf{T}}[\mathbf{x},t]\langle\boldsymbol{\xi}\rangle = \frac{1}{2} c\, \omega(\|\boldsymbol{\xi}\|) \frac{\boldsymbol{\xi}\otimes\boldsymbol{\xi}}{\|\boldsymbol{\xi}\|^2} \left(\mathbf{u}(\mathbf{x}+\boldsymbol{\xi},t) - \mathbf{u}(\mathbf{x},t)\right),$$

and let a two-dimensional static PD problem be

$$\begin{cases} -\displaystyle\int_{\mathscr{H}(\mathbf{x},\delta)} c\, \omega(\|\boldsymbol{\xi}\|) \frac{\boldsymbol{\xi}\otimes\boldsymbol{\xi}}{\|\boldsymbol{\xi}\|^2} \left(\mathbf{u}(\mathbf{x}') - \mathbf{u}(\mathbf{x})\right) dA_{\mathbf{x}'} = \mathbf{b}(\mathbf{x}), & \mathbf{x} \in \mathscr{B}, \qquad (5.13a) \\ \mathbf{u}(\mathbf{x}) = \mathbf{g}(\mathbf{x}), & \mathbf{x} \in \overline{\overline{\mathscr{B}}} \setminus \mathscr{B}, \qquad (5.13b) \end{cases}$$

where $\boldsymbol{\xi} = \mathbf{x}' - \mathbf{x}$, ω is an influence function, and $\mathbf{g}$ is a given function providing displacement boundary conditions. We choose the computational domain as a unit square: $\overline{\overline{\mathscr{B}}} = [0,1]\times[0,1]$. The solution $\mathbf{u}(\mathbf{x})$ to Problem (5.13) is sought in the inner domain $\mathscr{B} = (\delta, 1-\delta)\times(\delta, 1-\delta)$. An illustration of the inner domain and the boundary layer $\overline{\overline{\mathscr{B}}} \setminus \mathscr{B}$ is given in Figure 5.4.

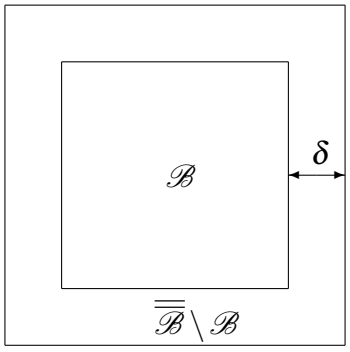

Figure 5.4: Two-dimensional domain $\overline{\overline{\mathscr{B}}}$ composed of two non-overlapping subdomains: the inner domain $\mathscr{B}$ and the boundary layer $\overline{\overline{\mathscr{B}}} \setminus \mathscr{B}$.

We find the PD constant c using a connection between the PD equation (5.13a) and the Navier-Cauchy equation of classical elasticity

$$-\frac{3}{4} E \left[\nabla(\nabla\cdot\mathbf{u})(\mathbf{x}) + \frac{1}{2}\nabla^2\mathbf{u}(\mathbf{x})\right] = \mathbf{b}(\mathbf{x}), \qquad (5.14)$$

with Young's modulus E and Poisson's ratio $\nu = 1/3$, assuming a quadratic displacement field, as

$$c = \frac{6E}{m}, \qquad (5.15)$$

where m is the weighted volume (*cf.* (5.18)) in 2D.

We assume a two-dimensional static PD problem given by (5.13) with $E = 1$, $\delta = 0.04$, $\mathbf{b} = (-\frac{9}{4}, 0)$, and $\mathbf{g}(\mathbf{x}) = (x^2, 0)$ with $\mathbf{x} = (x, y)$. The value of $\mathbf{b}$ is found using the method of manufactured solutions, to ensure consistency with the imposed boundary conditions. We discretize the problem with the discretization scheme (5.5).

We investigate the convergence of numerical solutions of Problem (5.13). We compare the performance of the algorithm FA in combination with different influence functions with the algorithms PA-PDLAMMPS, PA-HHB, and PA-AC, which denotes *Partial Area - Analytical Calculation*, that calculates partial areas analytically following [51]. The grid refinement is performed as in the one-dimensional problem: we begin with an initial $N \times N$ square grid with $N = 75$ ($\delta/h = 3$), a total of $5,625$ computational nodes, and gradually increase N by one until we reach $N = 150$ ($\delta/h = 6$), a total of $22,500$ computational nodes. The convergence results for different algorithms and influence functions are presented in Figure 5.5 for (a) $\alpha = 0$ and (b) $\alpha = 1$, where the error in the numerical solution is computed using an L^2-norm.

We conclude that using the algorithms PA-HHB or PA-AC, or using the algorithm FA in combination with a smooth influence function, improves the accuracy of the numerical solutions, for most grid spacings, in comparison to utilizing the algorithms FA or PA-PDLAMMPS. The quality of the convergence of the algorithm PA-PDLAMMPS is as poor as the one of the algorithm FA. As opposed to the one-dimensional results, here a first-order convergence is achieved for both $\alpha = 0$ and $\alpha = 1$, when using the algorithm FA in combination with an influence function with $P_5(r)$ (PWQ) or $P_7(r)$ (PWS). The convergence profile for the algorithm PA-AC is also oscillatory, but better than the one of the algorithm PA-HHB, and much better than the ones of the algorithms FA and PA-PDLAMMPS.

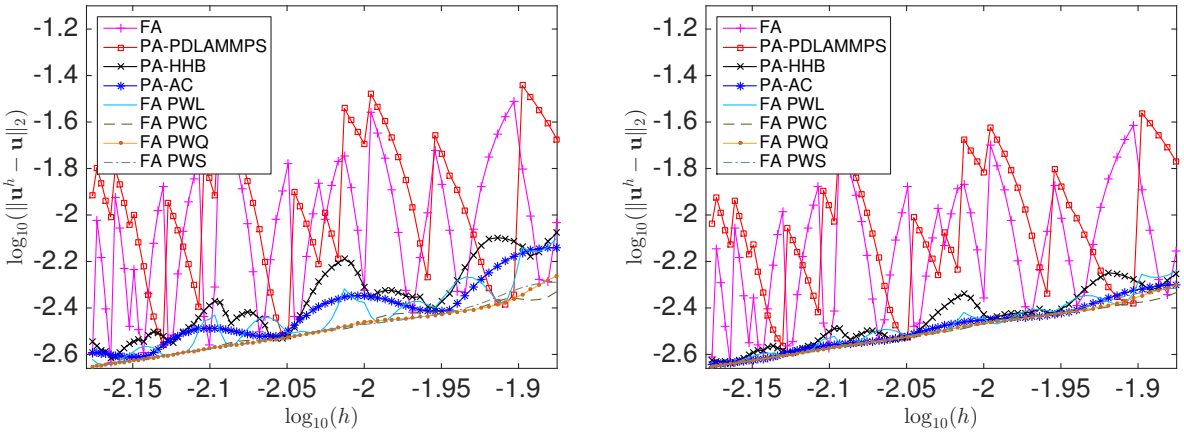

(a) $\alpha = 0$. (b) $\alpha = 1$.

Figure 5.5: Convergence of the numerical solution of Problem (5.13) using different algorithms for approximation of partial areas and different influence functions. The notation PWL, PWC, PWQ, and PWS refers, respectively, to the choice of influence function with polynomial $P_1(r)$, $P_3(r)$, $P_5(r)$, and $P_7(r)$.

5.5 A three-dimensional peridynamic problem

Let a PD model be given by a *linearized* linear peridynamic solid (LPS) constitutive model with force state [62]

$$\underline{\mathbf{T}}[\mathbf{x},t]\langle\boldsymbol{\xi}\rangle = \frac{3K-5G}{m}\omega(\|\boldsymbol{\xi}\|)\theta^{\text{lin}}(\mathbf{x},t)\boldsymbol{\xi} + \frac{15G}{m}\omega(\|\boldsymbol{\xi}\|)\frac{\boldsymbol{\xi}\otimes\boldsymbol{\xi}}{\|\boldsymbol{\xi}\|^2}(\mathbf{u}(\mathbf{x}+\boldsymbol{\xi},t)-\mathbf{u}(\mathbf{x},t)), \tag{5.16}$$

where the *linearized* nonlocal dilatation is given (in 3D) by

$$\theta^{\text{lin}}(\mathbf{x},t) = \frac{3}{m}\int_{\mathscr{H}(\mathbf{0},\delta)}\omega(\|\boldsymbol{\zeta}\|)\boldsymbol{\zeta}\cdot(\mathbf{u}(\mathbf{x}+\boldsymbol{\zeta},t)-\mathbf{u}(\mathbf{x},t))dV_{\boldsymbol{\zeta}}, \tag{5.17}$$

and where ω is an influence function, K is the bulk modulus, G is the shear modulus, and m is the weighted volume defined by

$$m := \int_{\mathscr{H}(\mathbf{0},\delta)}\omega(\|\boldsymbol{\xi}\|)\|\boldsymbol{\xi}\|^2 dV_{\boldsymbol{\xi}}. \tag{5.18}$$

Let a three-dimensional static PD problem be given by (*cf.* (5.1))

$$\begin{cases} -\displaystyle\int_{\mathscr{H}(\mathbf{x},\delta)}\frac{3K-5G}{m}\omega(\|\boldsymbol{\xi}\|)\left[\theta^{\text{lin}}(\mathbf{x})+\theta^{\text{lin}}(\mathbf{x}')\right]\boldsymbol{\xi} \\ \qquad\qquad +\dfrac{30G}{m}\omega(\|\boldsymbol{\xi}\|)\dfrac{\boldsymbol{\xi}\otimes\boldsymbol{\xi}}{\|\boldsymbol{\xi}\|^2}(\mathbf{u}(\mathbf{x}')-\mathbf{u}(\mathbf{x}))dV_{\mathbf{x}'} = \mathbf{b}(\mathbf{x}), \qquad \mathbf{x}\in\mathscr{B}, & \text{(5.19a)} \\ \qquad\qquad\qquad\qquad \mathbf{u}(\mathbf{x}) = \mathbf{g}(\mathbf{x}), \qquad \mathbf{x}\in\overline{\overline{\mathscr{B}}}\setminus\mathscr{B}, & \text{(5.19b)} \end{cases}$$

where $\boldsymbol{\xi} = \mathbf{x}'-\mathbf{x}$ and $\mathbf{g}$ is a given function providing displacement boundary conditions. We choose the computational domain as a unit cube: $\overline{\overline{\mathscr{B}}} = [0,1]\times[0,1]\times[0,1]$. The solution $\mathbf{u}(\mathbf{x})$ to Problem (5.19) is sought in the inner domain $\mathscr{B} = (2\delta,1-2\delta)\times(2\delta,1-2\delta)\times(2\delta,1-2\delta)$. Note that, in this case, the boundary layer $\overline{\overline{\mathscr{B}}}\setminus\mathscr{B}$ is chosen of width 2δ. The reason for that is the need to compute the linearized nonlocal dilatation (5.17) for each node in a layer of width δ around $\mathscr{B}$. An illustration of the inner domain and the boundary layer is given in Figure 5.6.

As opposed to the one- and two-dimensional problems, we do not employ here analytical calculations for partial volumes but instead estimate those quantities numerically. The numerical approximation method utilizes a combined strategy of recursive subdivision and sampling. Although the present study is restricted to uniform grids, the numerical method for computing partial volumes has been generalized and successfully applied to arbitrary nonuniform grids with hexahedral cells. As expected, the computational cost of approximating partial volumes in three dimensions increases with the desired accuracy of the calculation. For the present study, it was found that six levels of recursive subdivision and 64 sample points per subcube produced sufficiently accurate partial volume approximations. This approach is equivalent to employing a pure sampling approach with $(256)^3$ sample points per cubic cell. Further details about this methods can be found in [56].

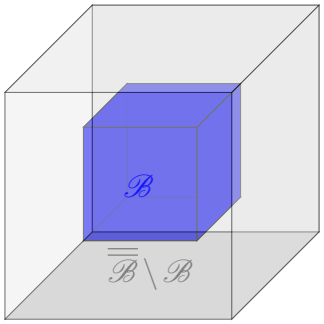

Figure 5.6: Three-dimensional domain $\overline{\overline{\mathscr{B}}}$ (large gray cube). The domain is composed of two non-overlapping subdomains: the inner domain $\mathscr{B}$ (small blue cube) and the boundary layer $\overline{\overline{\mathscr{B}}} \setminus \mathscr{B}$.

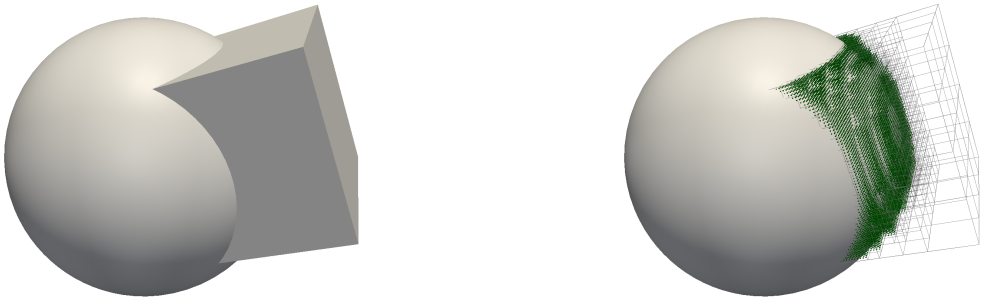

(a) Ball-cube intersection.

(b) Illustration of the partial volume algorithm.

Figure 5.7: Illustration of the algorithm for approximation of partial volumes. The algorithm utilizes recursive subdivision (gray wireframe) and sampling (green points). A large value of the mesh spacing, h, relative to the PD horizon, δ, is used here only to improve the clarity of the illustration; in practice, cubic cells are small relative to the neighborhood of a given node.

As in previous sections, we use the method of manufactured solutions for the convergence studies. However, in this case, we use a classical (local) equation to determine the appropriate body force density to prescribe in the PD problem. This is possible, due to the Proposition 1 below, based on Lemma 1.

Lemma 1. *For a quadratic displacement field, the linearized nonlocal dilatation* (5.17) *reduces to the dilatation in classical elasticity, i.e.,*

$$\theta^{\text{lin}}(\mathbf{x}) = \nabla \cdot \mathbf{u}(\mathbf{x}).$$

Proposition 1. *Let a PD model be given by the linearized LPS force state* (5.16)*. Then, for a quadratic displacement field, the peridynamic equilibrium equation* (5.4) *reduces to the Navier-Cauchy equation of classical elasticity.*

The proofs of Lemma 1 and Proposition 1 use a direct substitution of a quadratic displacement field and the symmetry of the integration range; more details can be found in [56].

We assume a three-dimensional static PD problem given by (5.19) with $K = 1$, $G = 0.5$, $\delta = 0.04$, $\mathbf{b} = (-\frac{10}{3}, 0, 0)$, and $\mathbf{g}(\mathbf{x}) = (x^2, 0, 0)$ with $\mathbf{x} = (x, y, z)$. The value of $\mathbf{b}$ is found using the method of manufactured solutions, based on Proposition 1, to ensure consistency with the imposed boundary conditions. We discretize the problem with the discretization scheme (5.5).

We investigate the convergence of numerical solutions of Problem (5.19). We compare the performance of the algorithm FV in combination with different influence functions with the algorithms PV-PDLAMMPS, PV-HHB, and PV-NC. The PV-NC algorithm, which denotes *Partial Volume - Numerical Calculation*, utilizes the numerical approximation method for partial volumes described above. The same grid refinement as in the one- and two-dimensional problems is used: we begin with an initial $N \times N \times N$ cubic grid with $N = 75$ ($\delta/h = 3$), a total of $421,875$ computational nodes, and gradually increase N by one until we reach $N = 150$, a total of $3,375,000$ computational nodes. The three-dimensional computational simulations were carried out using the *Peridigm* code, developed at Sandia National Laboratories [46]. The use of a parallel code, executed across multiple processors, was required due to the large computational expense associated with nonlocal calculations as the grid spacing, h, is reduced relative to the PD horizon, δ. The convergence results are presented in Figure 5.8 for (a) $\alpha = 0$ and (b) $\alpha = 1$, where the error in the numerical solution is computed using an L^2-norm.

We conclude that the algorithms PV-HHB and PV-NC, and the algorithm FV in combination with a smooth influence function, improve the accuracy of numerical solutions, for most grid spacings, relative to the algorithms FV and PV-PDLAMMPS. Of all the algorithms considered, the algorithm FV in combination with an influence function with $P_3(r)$ (PWC), $P_5(r)$ (PWQ), or $P_7(r)$ (PWS) yielded the best agreement with a first-order convergence for both values of α. The algorithm PV-NC produced an oscillatory profile, especially for $\alpha = 0$, which is smoother and of lower amplitude, however, than the profile for the algorithm PV-HHB, and definitely than the profiles for the algorithms FV and PV-PDLAMMPS. It should be mentioned, on the other hand, that the algorithm PV-NC is significantly more computationally expensive than the other algorithms.

5.6 Concluding remarks

We performed convergence studies of numerical solutions of static peridynamic problems. We explored two methods to reduce the discretization error in meshfree discretizations. The first method attempts to accurately compute intersections between neighbor cells and the neighborhood of a given node (referred to as *partial volumes*) and use those as quadrature weights. In standard meshfree discretizations of peridynamic models, partial volumes are taken as full nodal volumes. The second method attempts instead to minimize the contribution to the internal force density of nodes near the boundary of a given node, by incorporating smooth influence functions within peridynamic kernels. Our numerical results demonstrated that both methods improve the accuracy and convergence of numerical solutions, in comparison to the current practice. In particular, we showed that the oscillatory behavior of the convergence profile obtained in the current practice can be mitigated, and smoothed out, using accurate computations of partial volumes, and mostly eliminated,

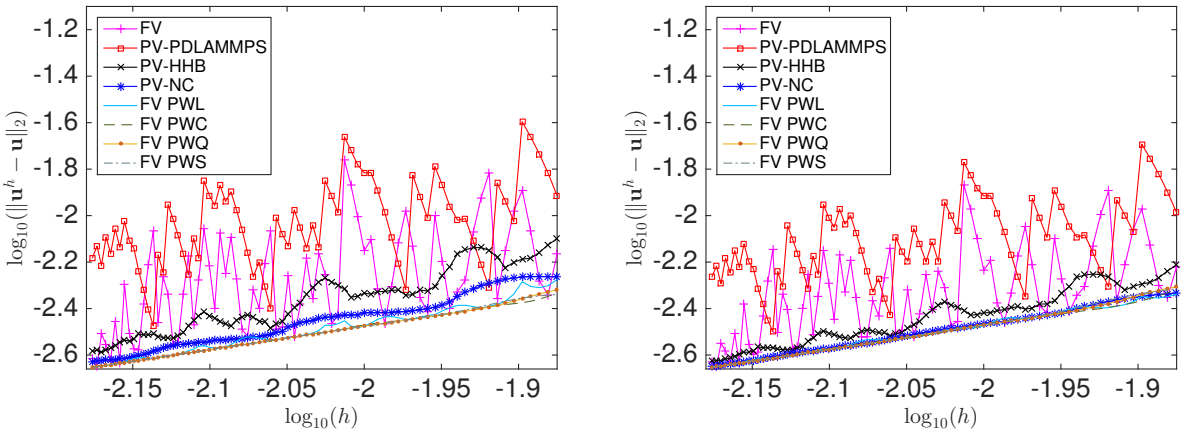

(a) $\alpha = 0$. (b) $\alpha = 1$.

Figure 5.8: Convergence of the numerical solution of Problem (5.19) using different algorithms for approximation of partial volumes and different influence functions. The notation PWL, PWC, PWQ, and PWS refers, respectively, to the choice of influence function with polynomial $P_1(r)$, $P_3(r)$, $P_5(r)$, and $P_7(r)$.

leading to a first-order convergence, when incorporating smooth influence functions. Extensions of the current study to non-uniform grids is of the essence toward reliable general peridynamic simulations.

Performing convergence studies of the type presented in this study is challenging, in particular with respect to the proper choice of peridynamic horizon. We found that, especially in higher dimensions, the peridynamic horizon cannot be so small as to make computations intractable, but it cannot be too large either as to result in that the boundary layer, where displacement boundary conditions are imposed, would represent the majority of the simulation domain. Under the current constrains, we concluded that choosing $\delta = 0.04$ and performing a grid refinement from $N_{\text{neig}} = 3$ to $N_{\text{neig}} = 6$ was a proper choice for the purpose of this study.

Chapter 6

Ductile Failure Models for Peridynamics

6.1 Introduction

It has been known for several years that any material model from the classical (local) theory of solid mechanics can be used directly within the peridynamic formulation [64, 73, 24]. The purpose of the work described in this chapter is to adapt *damage* models from the local theory to peridynamics. By doing so, we enable the numerical methods for local-to-nonlocal coupling described elsewhere in this report to use consistent damage models as well as consistent material models in both the local and the nonlocal regions.

Two types of local damage models are addressed in this work. The first is the *continuum damage mechanics* (CDM) class of models, which soften the elastic response of a material according to a predicted accumulation of damage. A comprehensive treatment of CDM may be found in the book by Krajcinovic [30]. In the present study, it is shown that, by embedding it in the peridynamic theory, CDM can be used to nucleate and grow cracks, an extension of traditional damage mechanics that was not previously possible.

The second type of damage model considered here is a ductile failure model, specifically the Tearing Parameter Model (TPM) proposed by Wellman [74]. This model has achieved success in predicting the failure of highly ductile metals in reasonably complex geometries and loading conditions. Previous implementations of the TPM used it only to initiate failure, while relying on supplemental techniques such as element death to propagate failure through the specimen. By incorporating TPM within peridynamics, we demonstrate that TPM can be used to model the growth as well as nucleation of failure in ductile metals, without these supplemental techniques.

6.2 Continuum damage mechanics

This section describes the use of continuum damage mechanics to determine the damage in peridynamic bonds. This allows CDM to nucleate and grow cracks in a simulation. First, the relevant aspects of peridynamics are reviewed, including the thermodynamic framework needed to apply CDM concepts in a consistent way.

6.2.1 Peridynamics review

The peridynamic theory [61, 65, 36] is an extension the classical theory of solid mechanics in which the field equations can be applied directly to evolving surfaces of discontinuity, especially cracks. In a peridynamic body $\mathscr{B}$, the equation of motion is written

$$\rho(\mathbf{x})\ddot{\mathbf{y}}(\mathbf{x},t) = \int_{\mathscr{H}_\mathbf{x}} \mathbf{f}(\mathbf{q},\mathbf{x},t)\, dV_\mathbf{q} + \mathbf{b}(\mathbf{x},t) \qquad \forall \mathbf{x} \in \mathscr{B} \tag{6.1}$$

where ρ is the density, $\mathbf{y}$ is the deformation map, $\mathbf{b}$ is the external body force density field, and $\mathbf{f}$ is a force density determined by the material model as described below. The equilibrium equation is

$$\int_{\mathscr{H}_\mathbf{x}} \mathbf{f}(\mathbf{q},\mathbf{x})\, dV_\mathbf{q} + \mathbf{b}(\mathbf{x}) = \mathbf{0} \qquad \forall \mathbf{x} \in \mathscr{B} \tag{6.2}$$

where $\mathscr{H}_\mathbf{x}$ is a neighborhood of $\mathbf{x}$ called the *family* of $\mathbf{x}$. The radius of this neighborhood is called the *horizon* of the material, denoted by δ. The vector valued function $\mathbf{f}(\mathbf{q},\mathbf{x})$ represents the force density (per unit volume squared) at $\mathbf{x}$ associated with the *bond* from $\mathbf{x}$ to each $\mathbf{q} \in \mathscr{H}_\mathbf{x}$. The values of $\mathbf{f}(\cdot,\mathbf{x})$ are determined by the material model as a function of the deformation of $\mathscr{H}_\mathbf{x}$.

In determining the force in each bond in a family, the bonds do not necessarily respond independently of each other, although such springlike material models are an important special case called *bond-based* material models. In general, the force density in each bond connected to $\mathbf{x}$ depends collectively on deformation of all the bonds connected to it. This more general case is represented mathematically by *state-based* material models. An example of a state-based model is a fluid, in which the force density in each bond connected to $\mathbf{x}$ depends only on the volume change of $\mathscr{H}_\mathbf{x}$.

To write down a state-based material model, it is helpful to use mathematical objects called *states*, which are simply mappings from the bonds in a family to some other quantity. The value of a state $\underline{A}$ at $\mathbf{x}$ operating on the bond $\mathbf{q}-\mathbf{x}$ is written as

$$\underline{A}[\mathbf{x}]\langle \mathbf{q}-\mathbf{x}\rangle.$$

Quantities in angle brackets are bonds; quantities in square brackets are the location of the family on whose bonds $\underline{A}[\mathbf{x}]$ operates. If a state is scalar valued, it is called a *scalar state*, denoted $\underline{A}$. If it is vector valued, it is called a *vector state*, denoted $\underline{\mathbf{A}}$.

Let $\mathbf{y}$ denote the deformation of $\mathscr{B}$. For any bond $\boldsymbol{\xi} \in \mathscr{H}_\mathbf{x}$, let

$$\underline{\mathbf{Y}}[\mathbf{x}]\langle \mathbf{q}-\mathbf{x}\rangle = \mathbf{y}(\mathbf{q}) - \mathbf{y}(\mathbf{x}).$$

$\underline{\mathbf{Y}}$ is called the *deformation state*. The deformation state is the basic kinematical quantity for purposes of material modeling and in this role is analogous to the deformation gradient $\mathbf{F} = \partial\mathbf{y}/\partial\mathbf{x}$ in the standard theory.

The pairwise force density $\mathbf{f}(\mathbf{q},\mathbf{x})$ depends on both the deformations of $\mathscr{H}_\mathbf{x}$ and $\mathscr{H}_\mathbf{q}$ through the *force states* $\underline{\mathbf{T}}[\mathbf{x}]$ and $\underline{\mathbf{T}}[\mathbf{q}]$:

$$\mathbf{f}(\mathbf{q},\mathbf{x}) = \underline{\mathbf{T}}[\mathbf{x}]\langle \mathbf{q}-\mathbf{x}\rangle - \underline{\mathbf{T}}[\mathbf{q}]\langle \mathbf{x}-\mathbf{q}\rangle. \tag{6.3}$$

From this expression it is immediate that $\mathbf{f}$ possesses the following antisymmetry:

$$\mathbf{f}(\mathbf{x},\mathbf{q}) = -\mathbf{f}(\mathbf{q},\mathbf{x}).$$

From this antisymmetry it is easily shown that a bounded peridynamic body has zero rate of change of total linear momentum in the absence of body forces.

States on a family $\mathscr{H}$ have a scalar product called the *dot product* defined by

$$\underline{A} \bullet \underline{B} = \int_{\mathscr{H}} \underline{A}\langle\boldsymbol{\xi}\rangle \underline{B}\langle\boldsymbol{\xi}\rangle \, dV_{\boldsymbol{\xi}}, \qquad \underline{\mathbf{A}} \bullet \underline{\mathbf{B}} = \int_{\mathscr{H}} \underline{\mathbf{A}}\langle\boldsymbol{\xi}\rangle \cdot \underline{\mathbf{B}}\langle\boldsymbol{\xi}\rangle \, dV_{\boldsymbol{\xi}}$$

for scalar states and vector states, respectively. Here, the small dot $\cdot$ denotes the usual scalar product of two vectors, $\mathbf{a}\cdot\mathbf{b} = a_i b_i$. The norm of two states is defined by

$$\|\underline{A}\| = \sqrt{\underline{A} \bullet \underline{A}}, \qquad \|\underline{\mathbf{A}}\| = \sqrt{\underline{\mathbf{A}} \bullet \underline{\mathbf{A}}}.$$

The *point product* of two scalar states is a scalar state defined by

$$(\underline{AB})\langle\boldsymbol{\xi}\rangle = \underline{A}\langle\boldsymbol{\xi}\rangle \underline{B}\langle\boldsymbol{\xi}\rangle \qquad \forall \boldsymbol{\xi} \in \mathscr{H}.$$

Let $\Psi(\underline{A})$ be a scalar valued function of a state $\underline{A}$. Suppose that for a given $\underline{A}$, there is a state $\Psi_{\underline{A}}(\underline{A})$ such that for any differential state $d\underline{A}$,

$$\Psi(\underline{A} + d\underline{A}) - \Psi(\underline{A}) = \Psi_{\underline{A}}(\underline{A}) \bullet d\underline{A}.$$

Then $\Psi_{\underline{A}}(\underline{A})$ is called the *Fréchet derivative* of Ψ at $\underline{A}$. The same definition applies to functions of a vector state:

$$\Psi(\underline{\mathbf{A}} + d\underline{\mathbf{A}}) - \Psi(\underline{\mathbf{A}}) = \Psi_{\underline{\mathbf{A}}}(\underline{\mathbf{A}}) \bullet d\underline{\mathbf{A}}.$$

Fréchet derivatives have many properties similar to ordinary and partial derivatives. For example, if $\underline{A}(\underline{B})$ is a state valued function, the following chain rule applies:

$$\Psi_{\underline{B}} = \Psi_{\underline{A}} \bullet \underline{A}_{\underline{B}},$$

which means

$$\Psi_{\underline{B}}\langle\boldsymbol{\xi}\rangle = \int_{\mathscr{H}} \Psi_{\underline{A}}\langle\boldsymbol{\zeta}\rangle \underline{A}_{\underline{B}}\langle\boldsymbol{\zeta},\boldsymbol{\xi}\rangle \, dV_{\boldsymbol{\zeta}}.$$

Here, the Fréchet derivative $\underline{A}_{\underline{B}}$ is an example of a *double state*, that is, a state that is a function of two bonds. Double states have the property that

$$d\underline{A}\langle\boldsymbol{\zeta}\rangle = \int_{\mathscr{H}} \underline{A}_{\underline{B}}\langle\boldsymbol{\zeta},\boldsymbol{\xi}\rangle d\underline{B}\langle\boldsymbol{\xi}\rangle \, dV_{\boldsymbol{\xi}}.$$

The *unit state* $\underline{1}$ is defined by

$$\underline{1}\langle\boldsymbol{\xi}\rangle = 1 \qquad \forall \boldsymbol{\xi} \in \mathscr{H}.$$

Note that $\underline{1} \bullet \underline{1} = V$, where V is the volume of $\mathscr{H}$. The *identity double state* $\underline{\Delta}$ is defined by

$$\underline{\Delta}\langle\boldsymbol{\zeta},\boldsymbol{\xi}\rangle = \Delta(\boldsymbol{\xi} - \boldsymbol{\zeta})$$

where Δ is the Dirac delta function on $\mathbb{R}^3$, that is,

$$(\underline{A} \bullet \underline{\Delta})\langle\boldsymbol{\xi}\rangle = \int_{\mathscr{H}} \underline{A}\langle\boldsymbol{\zeta}\rangle \underline{\Delta}\langle\boldsymbol{\zeta},\boldsymbol{\xi}\rangle \, dV_{\boldsymbol{\zeta}} = \underline{A}\langle\boldsymbol{\xi}\rangle$$

for any state $\underline{A}$.

6.2.2 Thermodynamic form of peridynamics

The peridynamic statement of the first law of thermodynamics at a point $\mathbf{x} \in \mathscr{H}$ is given by

$$\dot{\varepsilon} = \underline{\mathbf{T}} \bullet \underline{\dot{\mathbf{Y}}} + r + h \tag{6.4}$$

where ε is the internal energy density, r is the energy source rate (per unit volume), and h is the rate of energy transport to the point $\mathbf{x}$ [65]. Although a local model of heat conduction can be used to determine h, (6.4) is also compatible with nonlocal heat transport laws [10, 11, 42].

The appropriate statement of the second law is given by

$$\theta \dot{\eta} \geq r + h \tag{6.5}$$

where θ is the absolute temperature and η is the entropy density. The free energy is defined by

$$\psi = \varepsilon - \theta \eta \tag{6.6}$$

As described in [65], combining (6.4), (6.5), and (6.6) leads to

$$\underline{\mathbf{T}} \bullet \underline{\dot{\mathbf{Y}}} - \dot{\theta} \eta - \dot{\psi} \geq 0. \tag{6.7}$$

Suppose the material model for free energy density depends only on the deformation state and temperature:

$$\psi(\underline{\mathbf{Y}}, \theta). \tag{6.8}$$

From (6.7) and (6.8), reasoning similar to Coleman and Noll [16] leads to the conclusion that the force state and the entropy are related to the free energy density through

$$\underline{\mathbf{T}} = \psi_{\underline{\mathbf{Y}}}, \qquad \eta = \psi_{\theta}. \tag{6.9}$$

(The first equation is a Fréchet derivative; the second is a partial derivative.) Thus, in the absence dependence on history, rate, or other variables, a material model may be expressed completely in the form of a free energy function.

Damage may be included within the thermodynamic framework by introducing the *damage state* $\underline{\phi}$. This is a scalar state such that

$$\underline{\phi}\langle \boldsymbol{\xi} \rangle \geq 0, \qquad \underline{\dot{\phi}}\langle \boldsymbol{\xi} \rangle \geq 0 \qquad \forall \boldsymbol{\xi} \in \mathscr{H}. \tag{6.10}$$

By convention $\underline{\phi} = 0$ corresponds to undamaged material. It is often convenient, but not essential, to assume that $\underline{\phi} = 1$ corresponds to "fully damaged" material. As shown in [65], Coleman-Noll type reasoning for a material model in which the free energy density depends explicitly on the damage state,

$$\psi(\underline{\mathbf{Y}}, \theta, \underline{\phi}), \tag{6.11}$$

leads to the restriction on the material model

$$\psi_{\underline{\phi}}\langle \boldsymbol{\xi} \rangle \leq 0 \qquad \forall \boldsymbol{\xi} \in \mathscr{H} \tag{6.12}$$

as well as the entropy generation rate and dissipation inequality given by

$$\dot{\eta} = \frac{\dot{\psi}^{\mathrm{d}}}{\theta}, \qquad \dot{\psi}^{\mathrm{d}} = -\psi_{\underline{\phi}} \bullet \underline{\dot{\phi}} \tag{6.13}$$

where $\dot{\psi}^{\mathrm{d}}$ is the rate of energy dissipation due to damage progression.

6.2.3 Ordinary mechanical material model

In the previous section it was shown how the damage state, when incorporated into a material model through the dependence of free energy on it, interacts with the other thermodynamic variables. These interactions result in the restriction on the material model (6.12) as a result of the second law of thermodynamics. Having established these relationships, we are now free to assume a particular thermodynamic path that all deformations follow a given thermodynamic path, such as isothermal. In this case it is not necessary to explicitly retain dependence of ψ on temperature, because this is uniquely determined by the deformation. By convention, under this assumption, the free energy is then renamed the *strain energy* density is denoted by $W(\underline{\mathbf{Y}}, \underline{\phi})$.

For purposes of investigating continuum damage mechanics, it will further be assumed that the dependence of W on $\underline{\mathbf{Y}}$ is exclusively through changes in length of the bonds, not their rotation. In this case we write

$$W(\underline{e}, \underline{\phi})$$

where $\underline{e}$ is the scalar valued *extension state* defined by

$$\underline{e}\langle\boldsymbol{\xi}\rangle = |\underline{\mathbf{Y}}\langle\boldsymbol{\xi}\rangle| - |\boldsymbol{\xi}| \qquad \forall \boldsymbol{\xi} \in \mathscr{H}. \tag{6.14}$$

Evaluation of the necessary Fréchet derivative shows that the bond force vectors are always parallel to the direction of the deformed bonds:

$$\underline{\mathbf{T}}\langle\boldsymbol{\xi}\rangle = \underline{t}\langle\boldsymbol{\xi}\rangle\underline{\mathbf{M}}\langle\boldsymbol{\xi}\rangle, \qquad \underline{\mathbf{M}}\langle\boldsymbol{\xi}\rangle = \frac{\underline{\mathbf{Y}}\langle\boldsymbol{\xi}\rangle}{|\underline{\mathbf{Y}}\langle\boldsymbol{\xi}\rangle|}$$

where $\underline{t}$ is the scalar force state,

$$\underline{t} = W_{\underline{e}}. \tag{6.15}$$

The *thermodynamic force state* is defined by

$$\underline{z} = -W_{\underline{\phi}}. \tag{6.16}$$

The value of $\underline{z}\langle\boldsymbol{\xi}\rangle$ for any bond $\boldsymbol{\xi}$ represents the rate of decrease of strain energy density at $\mathbf{x}$ as the bond damage increases. In this sense it represents a driving force for damage in the bond, although not a mechanical force. However, in general, there is no compelling reason to assume that bonds with the greatest value of $\underline{z}\langle\boldsymbol{\xi}\rangle$ accumulate damage it the highest rate, although this is plausible.

In keeping with the assumption that is usually made in thermodynamic treatments of continuum damage mechanics, it will be assumed for present purposes that there exists a function

$$S(\underline{z}, \underline{\phi})$$

such that damage does not increase in any of the bonds whenever conditions at $\mathbf{x}$ are such that $S < 0$. Damage can increase when $S = 0$. However, it evolves in such a way that at all times $S \leq 0$, a requirement called the *consistency condition*.

Also in keeping with traditional treatments of damage mechanics, it will be assumed that if $S = 0$, the damage state changes in response to an incremental change in the extension state $d\underline{e}$ such that for some small non-negative scalar $d\lambda$,

$$d\underline{\phi} = S_{\underline{\phi}} d\lambda \tag{6.17}$$

This assumption together with monotonicity requirement stated in the second of (6.10) implies the following condition on S:

$$S_{\underline{\phi}}\langle \boldsymbol{\xi} \rangle \geq 0 \qquad \forall \boldsymbol{\xi} \in \mathscr{H}$$

which, geometrically, is a type of convexity condition on the surface $S = 0$ which resides in the infinite-dimensional space of scalar states.

The next question is how to compute the change in damage state resulting from a given incremental deformation of a family resulting in $d\underline{e}$. In view of (6.17), this task is the same as computing $d\lambda$. To do this, the consistency condition is applied to the total differential of $S(\underline{z}, \underline{\phi})$:

$$0 = dS = S_{\underline{z}} \bullet d\underline{z} + S_{\underline{\phi}} \bullet d\underline{\phi}.$$

Using (6.17), this implies

$$0 = S_{\underline{z}} \bullet d\underline{z} + S_{\underline{\phi}} \bullet S_{\underline{\phi}} d\lambda. \tag{6.18}$$

Recalling (6.16) and the material model $W(\underline{e}, \underline{\phi})$ leads to the following expression for the total differential of the thermodynamic force state:

$$d\underline{z} = -W_{\underline{\phi e}} \bullet d\underline{e} - W_{\underline{\phi\phi}} \bullet d\underline{\phi} = -W_{\underline{\phi e}} \bullet d\underline{e} - W_{\underline{\phi\phi}} \bullet S_{\underline{\phi}} d\lambda.$$

in which the second Fréchet derivatives $W_{\underline{\phi e}}$ and $W_{\underline{\phi\phi}}$ are double states. Using this last expression in (6.18) to eliminate $\underline{z}$ and solving for $d\lambda$ yields

$$d\lambda = \frac{S_{\underline{z}} \bullet W_{\underline{\phi e}} \bullet d\underline{e}}{S_{\underline{z}} \bullet S_{\underline{\phi}} - S_{\underline{z}} \bullet W_{\underline{\phi\phi}} \bullet S_{\underline{z}}},$$

hence, from (6.17),

$$d\underline{\phi} = S_{\underline{z}} \frac{S_{\underline{z}} \bullet W_{\underline{\phi e}} \bullet d\underline{e}}{S_{\underline{z}} \bullet S_{\underline{\phi}} - S_{\underline{z}} \bullet W_{\underline{\phi\phi}} \bullet S_{\underline{z}}}. \tag{6.19}$$

This equation provides the increment of the damage state in response to any incremental deformation such that $S = 0$ and the normality condition holds.

6.2.4 CDM with a bond-based material model

In this section, a bond-based, microelastic material is modified to include damage. The assumed strain energy density function is as follows:

$$W(\underline{e}, \underline{\phi}) = \int_{\mathscr{H}} w(\underline{e}\langle \boldsymbol{\xi} \rangle)(1 - \underline{\phi}\langle \boldsymbol{\xi} \rangle)\, dV_{\boldsymbol{\xi}} = \underline{w} \bullet (\underline{1} - \underline{\phi}) \tag{6.20}$$

where w is the micropotential of an undamaged bond and the scalar state $\underline{w}$ is defined by

$$\underline{w}\langle\boldsymbol{\xi}\rangle = w(\underline{e}\langle\boldsymbol{\xi}\rangle)$$

for all $\boldsymbol{\xi} \in \mathscr{H}$. The assumed form of w implies that the micropotential is necessarily isotropic in the absence of damage. Evaluating the Fréchet derivatives indicated in (6.15) and (6.16) leads to

$$\underline{t} = (\underline{1} - \underline{\phi})w', \qquad \underline{z} = \underline{w} \tag{6.21}$$

where w' is the first derivative of w, that is, the bond force density. The following double states are found directly from the second Fréchet derivatives of (6.20):

$$W_{\underline{\phi e}} = w'\underline{\Delta}, \qquad W_{\underline{\phi\phi}} = 0. \tag{6.22}$$

Let the failure surface be given by

$$S(\underline{z}, \underline{\phi}) = \underline{\mu} \bullet \underline{z} - \kappa(1 + \eta D), \qquad D = \underline{\tau} \bullet \underline{\phi}. \tag{6.23}$$

where κ and η are constants and $\underline{\mu}$ and $\underline{\tau}$ are given scalar states normalized such that

$$\underline{\mu} \bullet \underline{1} = \underline{\tau} \bullet \underline{1} = 1.$$

The scalar D can be thought of as a scalar damage variable derived from the damage state $\underline{\phi}$. The choices

$$\underline{\mu}\langle\boldsymbol{\xi}\rangle = \underline{\tau}\langle\boldsymbol{\xi}\rangle = 1/V \tag{6.24}$$

for all $\boldsymbol{\xi}$, where V is the volume of $\mathscr{H}$, result in isotropic response. From (6.21) and (6.23), the condition $S = 0$ for damage growth implies that damage can increase only when the deformation is large enough that

$$\underline{\tau} \bullet \underline{w} = \kappa(1 + \eta D).$$

From this expression, it can be observed that η represents a "hardening" coefficient for damage. (This term does not literally result in material hardening because w is the *undamaged* micropotential.) From the form of left side of this last equation, evidently damage can increase when the weighted average of the undamaged micropotentials among the bonds in a family exceed a threshhold that depends on the scalar damage.

From (6.23), the following Fréchet derivatives used in the normality condition are found:

$$S_{\underline{z}} = \underline{\mu}, \qquad S_{\underline{\phi}} = -\kappa\eta\,\underline{\tau}. \tag{6.25}$$

From (6.19), using (6.21), (6.22), and (6.25), the damage state increment in response to an increment in the extension state $d\underline{e}$ is given by

$$d\underline{\phi} = \begin{cases} \dfrac{(w'\underline{\tau}) \bullet d\underline{e}}{\kappa\eta\ \underline{\tau} \bullet \underline{\mu}}\ \underline{\mu} & \text{if } S = 0, \\ 0 & \text{if } S < 0. \end{cases} \tag{6.26}$$

The denominator in this expression does not depend on the deformation. The numerator can be thought of as the increment in work done by the bond extensions acting against the undamaged bond force densities. Another observation is that the damage state increment is always parallel (in the sense of states) to $\underline{\mu}$. Therefore, damage would tend to grow preferentially in bonds with larger values of $\underline{\mu}$, allowing planes of weakness to be included in a material model for damage.

6.2.5 CDM example

The development up to this point has shown how CDM, a tool from the local theory, can be used to damage and ultimately break nonlocal bonds. In this section, it is demonstrated by a computational example that this approach allows CDM to predict the nucleation and growth of discrete cracks.

A brittle plate with dimensions 50mm $\times$ 150mm $\times$ 5mm contains a hole with diameter 20mm. The Young's modulus is E=140GPa, the Poisson ratio is ν=0.25, and the density is 8000kg-m^{-3}. The peridynamic CDM model used in this example is as given in (6.23) and (6.24), with parameters

$$\eta = 10, \qquad \kappa = \frac{E\varepsilon_0^2}{3V}, \qquad \varepsilon_0 = 0.01$$

where V is the volume of the family. The Emu grid had a nominal spacing of 1.0mm and used about 38,000 nodes. A strain rate of 45s^{-1} is initialized in the grid with constant velocity boundary conditions at the ends.

Figure 6.1 shows the predicted progression of damage after nucleation at the sites of the stress concentrations. A key feature of the results are the gradual accumulation of damage at these sites, followed by a sudden transition to unstable dynamic fracture, as shown in Figure 6.2. This general pattern of an abrupt transition from stable to unstable crack growth is often observed experimentally in materials such as composites. This pattern is not reproduced by peridynamics with a simple bond strain criterion for bond failure with isotropic materials, without CDM. To illustrate this, the figure compares the damage growth using CDM and the *prototype microelastic brittle* (PMB) model [63], which uses a simple bond breakage criterion. With the PMB model, there is no stable phase of damage growth, and dynamic fracture occurs almost immediately after the nucleation of damage.

6.2.6 Using a classical CDM model

Suppose that a classical material model (that is, from the local theory) is provided together with an appropriate failure surface within the traditional thermodynamic CDM framework. We want to use this CDM model directly in peridynamics to break bonds according to the method described above. The strain energy density function and failure surface have the following forms:

$$W_{\text{local}}(\mathbf{F}, D), \qquad S_{\text{local}}(Z, D)$$

where $\mathbf{F} = \partial\mathbf{y}/\partial\mathbf{x}$ is the deformation gradient tensor, D is the scalar damage variable, and Z is the (scalar) thermodynamic force, defined by

$$Z = -\frac{\partial W_{\text{local}}}{\partial D}. \tag{6.27}$$

D is assumed to be related to the damage state by

$$D = \underline{\tau} \bullet \underline{\phi} \tag{6.28}$$

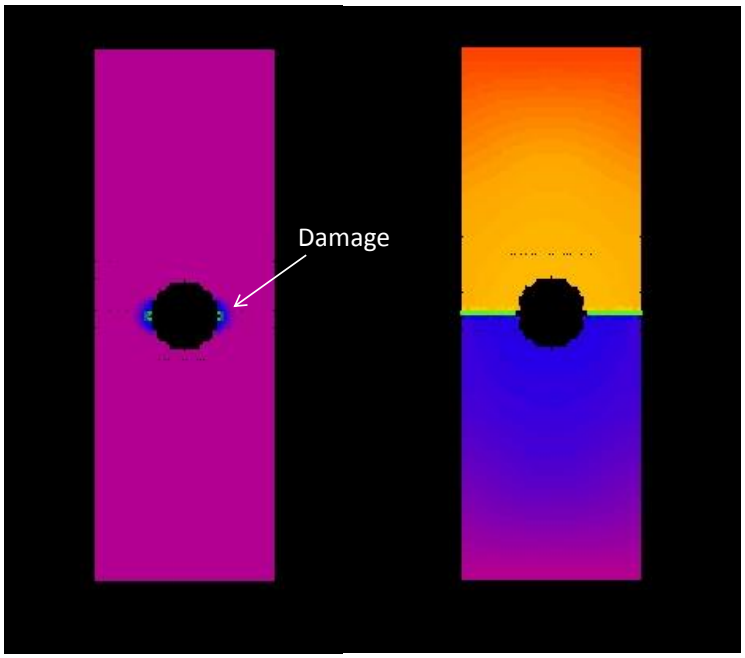

Figure 6.1: Damage accumulation followed by dynamic fracture using CDM. Left: contours of the stable damage when the nominal strain is 0.0057. Right: contours of displacement showing the fully formed cracks when the nominal strain is 0.009.

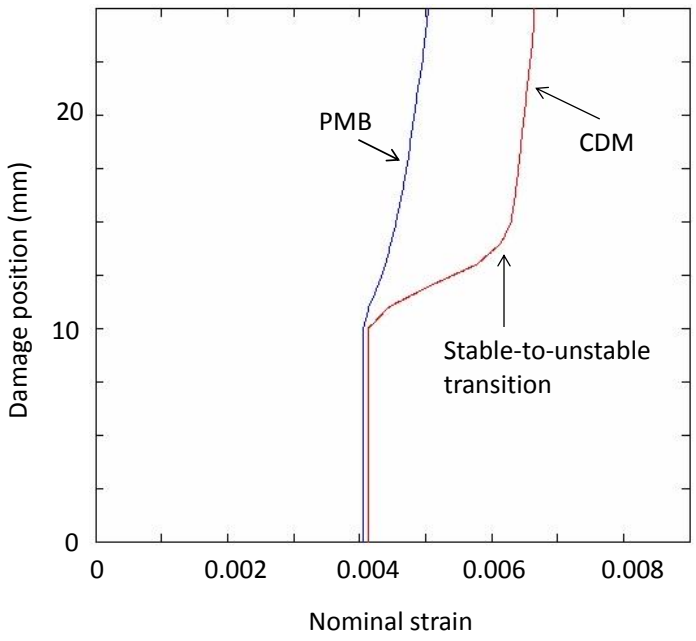

Figure 6.2: Position of the damaged region as a function of nominal strain in the CDM example problem, using both the CDM and PMB peridynamic damage models.

where $\underline{\tau}$ is a prescibed scalar state normalized such that $\underline{\tau} \bullet \underline{1} = 1$.

To use this model in peridynamics, it may be treated as a correspondence material [64]. Define the peridynamic strain energy density function by

$$W(\underline{\mathbf{Y}}, \underline{\phi}) = W_{\text{local}}(\mathbf{F}, D), \qquad S(\underline{z}, \underline{\phi}) = S_{\text{local}}(Z, D) \tag{6.29}$$

where $\mathbf{F}$ is the approximate deformation gradient tensor, given by

$$\mathbf{F} = \left(\int_{\mathscr{H}} \underline{\omega}\langle \boldsymbol{\xi} \rangle \underline{\mathbf{Y}}\langle \boldsymbol{\xi} \rangle \otimes \boldsymbol{\xi} \, dV_{\boldsymbol{\xi}} \right) \mathbf{K}^{-1}, \qquad \mathbf{K} = \int_{\mathscr{H}} \underline{\omega}\langle \boldsymbol{\xi} \rangle \boldsymbol{\xi} \otimes \boldsymbol{\xi} \, dV_{\boldsymbol{\xi}}, \tag{6.30}$$

where $\underline{\omega}$ is a non-negative valued influence function. From (6.16), (6.27), (6.28), and the chain rule for Fréchet derivatives,

$$\underline{z} = -W_{\underline{\phi}} = -\frac{\partial W_{\text{local}}}{\partial D} D_{\underline{\phi}} = Z\underline{\tau}.$$

Taking the dot product of both sides of this equation with $\underline{1}$ yields

$$Z = \underline{z} \bullet \underline{1}. \tag{6.31}$$

As derived in [64], the force state associated with this correspondence model is given by

$$\underline{\mathbf{T}}\langle \boldsymbol{\xi} \rangle = W_{\underline{\mathbf{Y}}}\langle \boldsymbol{\xi} \rangle = \underline{\omega}\langle \boldsymbol{\xi} \rangle \boldsymbol{\sigma} \mathbf{K}^{-1} \boldsymbol{\xi} \tag{6.32}$$

for all $\boldsymbol{\xi} \in \mathscr{H}$, where $\boldsymbol{\sigma}$ is the Piola stress tensor given by

$$\boldsymbol{\sigma}(\mathbf{F}, D) = \frac{\partial W_{\text{local}}}{\partial \mathbf{F}}(\mathbf{F}, D).$$

In summary, the peridynamic implementation of the classical material model is accomplished by the definitions in (6.29) with D, $\mathbf{F}$, and Z given by (6.28), (6.30), and (6.31) respectively. The force state is given by (6.32), which includes the effect of damage through the stress tensor.

6.3 Implementation of a ductile failure model

The preceding discussion concerned a thermodynamically consistent framework in which to model the accumulated effect of material damage on bond forces, under the assumption that damage is the only history-dependent variable. While this concept could be extended to include plasticity, it is worthwhile to investigate a simpler phenomenological approach to the prediction of failure in ductile metals.

In brittle materials, the salient feature of fracture in most cases is the constant rate of energy consumption per unit area of crack growth, an approximation proposed by Griffith and confirmed by extensive experimentation. In the Griffith concept of a brittle crack, a crack grows when there is sufficient energy available from boundary loading and stored energy in the body to supply the

critical energy release rate. The peridynamic theory reproduces this constant rate of energy consumption using the simplest damage model: bond breakage at a critical prescribed bond strain. This critical bond strain can be related by a simple formula to the critical energy release rate [63] and varies with the horizon.

However, the critical strain approach to peridynamic bond damage is not effective in modeling ductile failure, mainly because it fails to account for the strong effect of triaxiality. This creates a need for a workable approach to modeling ductile failure that is compatible with peridynamics and with the local theory, as a tool in local-to-nonlocal coupling.

To fulfill this need, a ductile failure model called the *Tearing Parameter Model* [74] (TPM) was adapted to peridynamics in the present work. The TPM is attractive because it encompasses the main experimentally observed effect, the cumulative effect of tensile hydrostatic stress as shear deformation progresses, in a simple form. The following discussion mainly concerns the practical, rather than theoretical, aspects of implementing the TPM in the most commonly used discretization technique for peridynamics.

In the TPM (as implemented in the local theory), a scalar P call the *tearing parameter* is computed from the following relation:

$$P = \int_0^t \left(\max\left\{ 0, \frac{2\sigma_1}{3(\sigma_1 - \bar{\sigma})} \right\} \right)^4 \dot{\varepsilon}_p \, dt' \tag{6.33}$$

where ε_p is the equivalent plastic strain, σ_1 is the largest (most tensile) of the three principal stresses, and $\bar{\sigma} = \text{Trace}\,\boldsymbol{\sigma}/3$ is the hydrostatic stress. Failure occurs with P reaches a critical value P_c.

In a uniaxial tensile test with applied stress $\sigma_0 > 0$, one finds that $\sigma_1 = \sigma_0$ and $\bar{\sigma} = \sigma_0/3$; therefore P_c equals the equivalent plastic strain at failure. This test therefore provides the only required material parameter for the TPM.

Post-failure response is not addressed by the TPM. In a typical finite element implementation, post-failure response is modeled with the help of element death. In the peridynamic implementation, because of its inherent compatibility with discontinuities, we hope to avoid the need for element death and similar strategies.

Since peridynamics is a nonlocal theory, implementation of the TPM requires the identification of the variables σ_1, $\bar{\sigma}$, and ε_p. These quantities are provided as part of the correspondence models for plasticity in peridynamics [73, 24]. The correspondence approach to peridynamic material modeling uses a local model directly, with intermediate quantities derived from the family of a point. The basic relations are given in (6.30) and (6.32). Correspondence material models using a particle discretization [63] tend to exhibit zero energy modes of deformation which require corrective forces to suppress them [34, 14].

In applying the TPM in this particle discretization, it is helpful to associate a value of P with the bond connecting $\mathbf{x}$ to $\mathbf{x}'$:

$$P(\mathbf{x}, \mathbf{x}') = (P(\mathbf{x}) + P(\mathbf{x}'))/2.$$

The bond $\boldsymbol{\xi}$ breaks irreversibly when this value of P for the bond exceeds the critical value for the material:

$$P(\mathbf{x},\mathbf{x}') \geq P_c \quad \Longrightarrow \quad \underline{\phi}[\mathbf{x}]\langle \mathbf{x}'-\mathbf{x}\rangle = 1.$$

Because of the power 4 in the integrand in (6.33), experience with numerical implementation has shown that P can be very sensitive to discretization errors and inevitable oscillations. To help reduce this sensitivity, it is helpful to perform the time integration in (6.33) using averaged quantities for the integrand. Define

$$Q(\mathbf{x}) = \frac{1}{V}\int_{\mathscr{H}} S(\mathbf{x}')\frac{2\sigma_1(\mathbf{x}')}{3(\sigma_1(\mathbf{x}')-\bar{\sigma}(\mathbf{x}'))}\,dV_{\mathbf{x}'}, \qquad R(\mathbf{x}) = \frac{1}{V}\int_{\mathscr{H}} \dot{\varepsilon}_p(\mathbf{x}')\,dV_{\mathbf{x}'}$$

where V is the volume of $\mathscr{H}$ and $S(\mathbf{x}')$ is a surface factor defined below. Then

$$P(\mathbf{x}) = \int_0^t Q(\mathbf{x})R(\mathbf{x})dt'.$$

In practice, it is important that the Q and R variables be averaged separately, rather than combined into one averaged variable.

The form of the integrand in (6.33) also tends to result in excessive sensitivity of P to irregulaties on the surface of a grid. To help reduce this sensitivity, a surface factor S is introduced that modifies the integrand. $S(\mathbf{x})$ is defined to by

$$S(\mathbf{x}) = \frac{V_m(\mathbf{x})}{V(\mathbf{x})}$$

where $V(\mathbf{x})$ is the volume of $\mathscr{H}$, and $V_m(\mathbf{x})$ is the volume of $\mathscr{H}$ that is occupied by the ductile material (not void).

In the particle discretization, zero energy modes create difficulties when modeling ductile material response because of the long time scales that are typically involved in simulating laboratory tests, and because of the use of correspondence material models. A number of techniques for controlling zero energy modes are helpful in this application. Among these are the following.

- A method due to Littlewood [34] applies forces to material particles that tend to make each family deform in a way that closely approximates a homogeneous deformation with deformation gradient $\mathbf{F}$, where $\mathbf{F}$ is found from (6.30). In the present study, these forces are computed from

  $$\underline{\mathbf{T}}_L\langle \mathbf{x}'-\mathbf{x}\rangle = \beta_L C\Big(|\mathbf{F}(\mathbf{x}'-\mathbf{x})| - |\underline{\mathbf{Y}}\langle \mathbf{x}'-\mathbf{x}\rangle|\Big)\mathbf{M}$$

  where β_L is a constant on the order of 0.02, $\underline{\mathbf{Y}}$ is the deformation state, $\mathbf{M}$ is the deformed bond direction vector, and C is an equivalent micromodulus:

  $$\mathbf{M} = \frac{\underline{\mathbf{Y}}\langle \mathbf{x}'-\mathbf{x}\rangle}{|\underline{\mathbf{Y}}\langle \mathbf{x}'-\mathbf{x}\rangle|}, \qquad C = \frac{18k}{\pi\delta^5}.$$

The force state from the material model $\underline{\hat{\mathbf{T}}}$ is modified by

$$\underline{\mathbf{T}} = \underline{\hat{\mathbf{T}}}(\underline{\mathbf{Y}}) + \underline{\mathbf{T}}_L.$$

This modified force state is used in (6.3).

- The main limitation of using $\underline{\mathbf{T}}_L$ by itself as a method for controlling zero energy modes is that it does not resist rotations of bonds. Therefore, it is helpful to add an additional "drag" term to the equation of motion that tends to smooth out variations in velocity within each family. To do this, define the weighted internal force density at $\mathbf{x}$ by

$$\mathbf{L}_f(\mathbf{x}) = \frac{\int_{\mathscr{H}_\mathbf{x}} \mathbf{L}(\mathbf{x}')(1 - \underline{\phi}\langle \mathbf{x}' - \mathbf{x} \rangle)\, dV_{\mathbf{x}'}}{\int_{\mathscr{H}_\mathbf{x}} (1 - \underline{\phi}\langle \mathbf{x}' - \mathbf{x} \rangle)\, dV_{\mathbf{x}'}}$$

where $\mathbf{L}$ is the internal force density field determined from the material model, as it appears in (6.1):

$$\mathbf{L}_0(\mathbf{x}') = \int_{\mathscr{H}_{\mathbf{x}'}} \mathbf{f}(\mathbf{q}, \mathbf{x}')\, dV_\mathbf{q}.$$

The internal force density at $\mathbf{x}$ is modified according to

$$\mathbf{L}(\mathbf{x}) = (1 - \beta_D)\mathbf{L}_0(\mathbf{x}) + \beta_D \mathbf{L}_f(\mathbf{x})$$

where β_D is a constant on the order of 0.005. The modified equation of motion, omitting time from the notation, is then written as

$$\rho(\mathbf{x})\ddot{\mathbf{y}}(\mathbf{x}) = \mathbf{L}(\mathbf{x}) + \mathbf{b}(\mathbf{x}).$$

Because broken bonds are not included in $\mathbf{L}_f$, the drag forces do not suppress the formation of cracks.

Littlewood's method and drag forces, when used together, are effective in controlling zero energy modes in typical ductile failure simulations using the TPM in peridynamics when using the particle discretization.

Damage affects correspondence materials in peridynamics in two ways:

- The influence function $\underline{\omega}$ that appears in (6.30) is assumed to vanish for broken bonds:

$$\underline{\omega} = (\underline{1} - \underline{\phi})\underline{\omega}_0$$

where $\underline{\omega}_0$ is an influence function independent of the damage state. Since $\underline{\omega}$ appears in (6.32), it follows that

$$\underline{\phi}\langle \boldsymbol{\xi} \rangle = 1 \quad \Longrightarrow \quad \underline{\mathbf{T}}\langle \boldsymbol{\xi} \rangle = 0.$$

- It is assumed that the underlying correspondence material model incorporates stress reduction due to damage. One way of including damage is by setting

$$\boldsymbol{\sigma}(\mathbf{F},D) = (1-D)\boldsymbol{\sigma}_0(\mathbf{F})$$

where D is given by (6.28) and $\sigma_0(\mathbf{F})$ is the stress tensor computed by the local material model, without damage. Such a reduction in stress is essential in correspondence material models, because without it, the breakage of a bond would have the undesired effect of increasing the force densities in other bonds (because $\underline{\omega}$ appears in the expressions for both $\mathbf{F}$ and $\mathbf{K}$ in (6.30)).

6.3.1 Ductile failure example

The TPM was applied to modeling the failure of a notched tensile specimen with 6061-T6 aluminum alloy. The specimen has an outer diameter of 22mm and a semicircular notch radius of 5mm. The Emu discretization has a nominal grid spacing of 0.3mm with a total of about 344,000 nodes. The Johnson-Cook plasticity model is used with the material parameters shown in Table 6.1. The value of E is scaled down from the physically correct value of 70GPa to allow a larger time step to be used. A velocity gradient of 200s^{-1} is initialized in the numerical grid with constant velocity boundary conditions at the ends.

The simulation results are shown in Figure 6.3. Because the notch results in high tensile pressures near the central axis, the TPM correctly predicts the nucleation of damage near the center. After the nucleation of damage, these strongly tensile pressures no longer exist, and further progression of the crack to the free surface involves larger plastic strains. The net effect of this transition in failure mechanism is to form a cup-like failure surface, reminiscent of the cup-and-cone features often seen in ductile failure of rods in tension. The figure also shows that for three values of discretization spacing, the method predicts about the same load at failure.

Parameter	*Value*	*Units*
Young's modulus, E	15	GPa
Poisson ratio, ν	0.333	
Johnson-Cook A	324	MPa
Johnson-Cook B	114	MPa
Johnson-Cook n	0.42	
Johnson-Cook C	0	
Johnson-Cook m	1.34	
Tearing parameter P_c	1.57	

Table 6.1: Material properties used for 6061-T6 Al with the Johnson-Cook plasiticity and tearing parameter ductile failure models.

In summary, the implementation of CDM and the TPM within peridynamics allows damage modeling to be performed consistently between local and nonlocal regions within a body. The

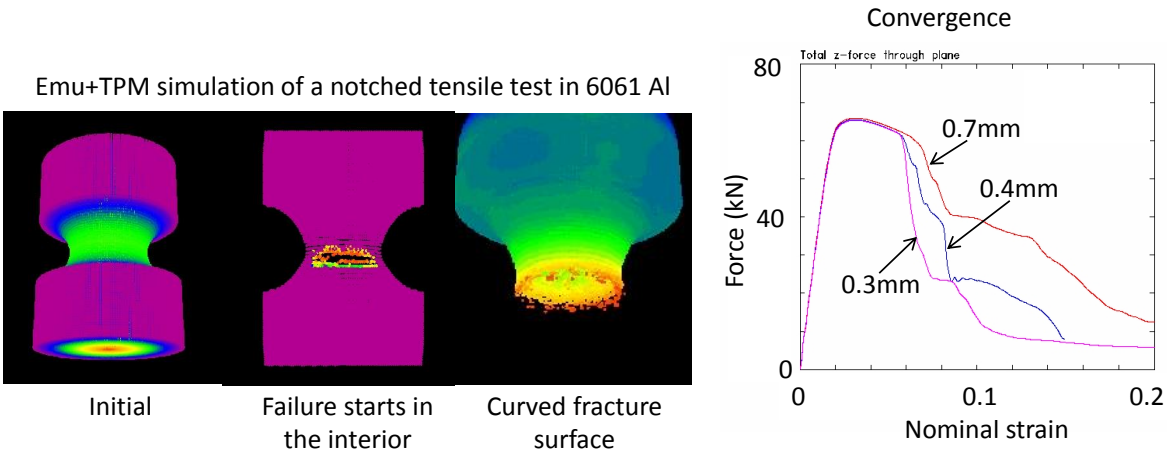

Figure 6.3: Left: grid plots showing the nucleation of damage and the cup-like shape of the failure surface. Right: load vs. nominal strain for three different grid spacings.

adaptation of these techniques to degrade and break peridynamic bonds is the primary research contribution of this portion of the LDRD project.

Chapter 7

Software Implementation of Local-Nonlocal Coupling

7.1 Introduction

A primary motivation for the coupling strategies and extensions to peridynamic theory developed in this project was the advancement of peridynamics as an engineering analysis tool. The ability to couple nonlocal peridynamic models and classical local models enables peridynamics to be integrated directly within existing analyst workflows. This approach leverages the large investment in existing analysis codes, mitigates the computational expense of nonlocal models, and can reduce or eliminate difficulties associated with the application of boundary conditions to nonlocal models [2, 32, 43]. To be effective in these respects, strategies for coupling local and nonlocal models must themselves be computationally efficient and amenable to implementation in mainstream analysis codes.

This chapter summarizes the implementation of the partial-stress approach for local-nonlocal coupling within the *Peridigm* [46, 48] peridynamics code and the *Albany* [50] computational mechanics code, which is based on the classical (local) theory. Implementation of the partial-stress approach within a pure peridynamics code is presented first, followed by a discussion of coupling independent codes for the integration of local and nonlocal models within a single executable. The software engineering follows an *agile components* strategy and utilizes numerous packages from the *Trilinos* [25, 26, 70] software project to enable efficient, massively parallel computational simulations. Local-nonlocal coupling is demonstrated though a set of test cases designed to verify the effectiveness of the partial-stress approach for the solution of boundary-value problems with known solutions.

7.2 Implementation of Partial Stress Models in *Peridigm*

Initial implementation of the partial-stress formulation was carried out in the *Peridigm* peridynamics code. This required modifications to the constitutive models, and the implementation of a divergence operator. Modifications to the constitutive models enabled calculation of the partial stress, defined in Equation (2.19), in addition to the standard peridynamic force state. Implemen-

tation of a divergence operator was required for evaluation of the partial internal force density, given by Equation (2.20). Note that while the divergence operator is a standard component of finite-element codes, it was not previously implemented in *Peridigm* because peridynamic models operate directly on displacements and forces, as opposed to the stress-strain relations utilized in mainstream finite-element codes.

To illustrate the process of extending a peridynamic constitutive model for calculation of partial stress, the internal force routine for the *linear peridynamic solid* material model is presented in Algorithm 1 [64, 32]. Here, $\mathbf{f}$ denotes force density, θ represents dilatation, $\mathbf{x}$ denotes position in the undeformed configuration, $\mathbf{u}$ denotes displacement, ξ is an undeformed bond, η is a change in bond length, δ is the peridynamic horizon, $\underline{\omega}$ is the influence function, $\underline{e}$ denotes extension state, m denotes weighted volume, ΔV is the volume associated with a material point, $\underline{e}^d$ denotes deviatoric extension state, k and μ are the bulk and shear moduli, respectively, $\underline{t}$ is the force state, $\underline{\mathbf{M}}$ is the vector connecting two material points in the deformed configuration, and $\boldsymbol{\nu}^{\text{ps}}$ is the partial stress. The extensions to the constitutive model, highlighted in red, are straightforward and results in very little increase in computational expense.

An implementation of the divergence operator is required for calculation of nodal forces based on the partial stress. Following Equation (2.20), the partial internal force density is found as

$$\mathbf{L}(\mathbf{x}) = \nabla \cdot \nu(\mathbf{x}) = \text{Tr}\big(\nabla \nu(\mathbf{x})\big).$$

For the meshfree discretization of Silling and Askari [63], the partial internal force density may be computed using an approach similar to that of the correspondence model formulation given in [64],

$$\nabla \cdot \nu(\mathbf{x}) = \text{Tr}\left(\left(\sum_{n=1}^{N} \underline{\omega}\langle \xi^n \rangle \{\nu(\mathbf{x}^n) - \nu(\mathbf{x})\} \otimes \xi^n \Delta V^n\right) \mathbf{K}^{-1}\right),$$

where N is the number of neighbors for the material point at $\mathbf{x}$ and $\mathbf{K}$ is the *shape tensor*,

$$\mathbf{K} = \sum_{i=0}^{N} \underline{\omega}_i \underline{\mathbf{x}}_i \otimes \underline{\mathbf{x}}_i \Delta V_{\mathbf{x}_i}.$$

The *Peridigm* implementation of the partial stress was verified using test cases in which a rectangular bar with a varying horizon is subjected to a prescribed displacement field. The value of the horizon over the length of the bar is illustrated in Figure 7.1. The horizon is large over the central region of the bar, and is reduced to a smaller value near the ends of the bar. The small horizon value near the ends of the bar facilitates coupling to a local model, whereas the large horizon value applied elsewhere allows for the modeling of nonlocal effects. Tests were carried out using both the standard peridynamic constitutive model formulation, and the partial stress formulation. The test simulations utilized an elastic correspondence material model [64] with a Young's modulus of 200.0 GPa and a Poisson's ratio of zero.

Figure 7.2 presents results for a prescribed linear displacement field. As shown in Figure 7.2a, the conventional peridynamic model produces so-called ghost forces in the region of the model over which the horizon is varying. The partial stress solution, shown in Figure 7.2b, produces the

Algorithm 1 Routine for calculation of the internal force density for a *linear peridynamic solid* material with a Gaussian influence function.

procedure LINEAR PERIDYNAMIC SOLID INTERNAL FORCE
    ▷ Initialize global force density vector to zero
    for each node i **do**
        $\mathbf{f}_i \leftarrow 0$
        $\boldsymbol{\nu}^{\mathrm{ps}}{}_i \leftarrow \mathbf{0}$
    end for
    ▷ Compute the dilatation for each node
    for each node i **do**
        $\theta_i \leftarrow 0$
        for each node j in neighbor list for node i **do**
            $\xi \leftarrow \mathbf{x}_j - \mathbf{x}_i$
            $\eta \leftarrow \mathbf{u}_j - \mathbf{u}_i$
            $\underline{\omega} \leftarrow \exp\left(-\frac{|\xi|^2}{\delta^2}\right)$
            $\underline{e} \leftarrow |\xi + \eta| - |\xi|$
            $\theta_i \leftarrow \theta_i + \frac{3}{m_i}\,\underline{\omega}\,|\xi|\,\underline{e}\,\Delta V_j$
        end for
    end for
    ▷ Compute pairwise contribution to global force density vector
    for each node i **do**
        for each node j in neighbor list for node i **do**
            $\xi \leftarrow \mathbf{x}_j - \mathbf{x}_i$
            $\eta \leftarrow \mathbf{u}_j - \mathbf{u}_i$
            $\underline{\omega} \leftarrow \exp\left(-\frac{|\xi|^2}{\delta^2}\right)$
            $\underline{e} \leftarrow |\xi + \eta| - |\xi|$
            $\underline{e}^d \leftarrow \underline{e} - \frac{\theta_i |\xi|}{3}$
            $\underline{t} \leftarrow \frac{3}{m_i}\,k\,\theta_i\,\underline{\omega}\,|\xi| + \frac{15\mu}{m_i}\,\underline{\omega}\,\underline{e}^d$
            $\underline{\mathbf{M}} \leftarrow \frac{\xi+\eta}{|\xi+\eta|}$
            $\mathbf{f}_i \leftarrow \mathbf{f}_i + \underline{t}\,\underline{\mathbf{M}}\,\Delta V_j$
            $\mathbf{f}_j \leftarrow \mathbf{f}_j - \underline{t}\,\underline{\mathbf{M}}\,\Delta V_i$
            ▷ Compute pairwise contribution to the partial stress
            $\boldsymbol{\nu}^{\mathrm{ps}}{}_i \leftarrow \boldsymbol{\nu}^{\mathrm{ps}}{}_i + (\underline{t} \otimes \xi)\,\Delta V_j$
        end for
    end for
end procedure

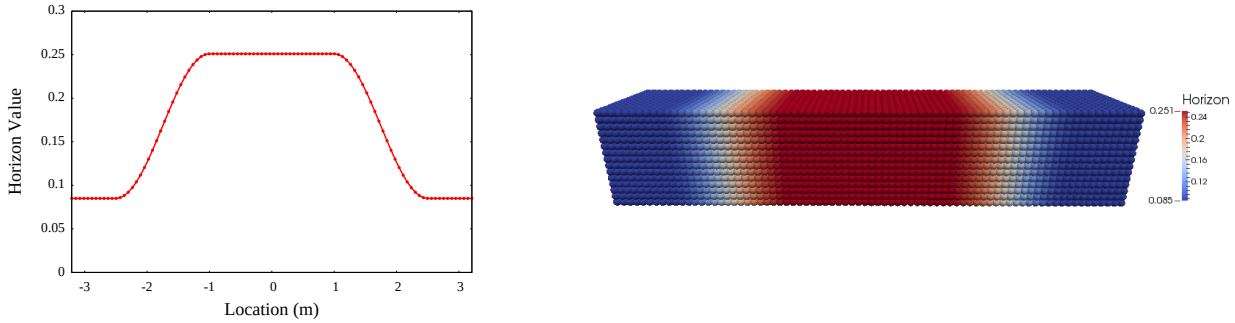

(a) Horizon as a function of position.

(b) Computational model.

Figure 7.1: Configuration for test simulations using a variable horizon.

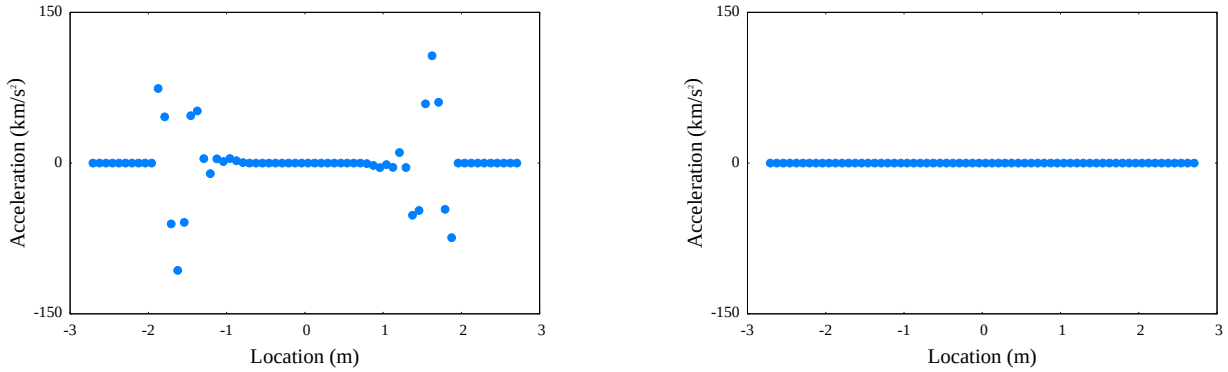

(a) Standard peridynamic model.

(b) Peridynamic partial stress model.

Figure 7.2: Acceleration values along the length of the bar under an imposed linear displacement field.

expected result of zero acceleration over the bar. Results are similar for the test case involving a prescribed quadratic displacement field, shown in Figure 7.3; the standard peridynamic formulation yields ghost forces, while the partial stress formulation yields the expected constant acceleration. For clarity, nodes near the ends of the bar, which experience nonzero reaction forces, are omitted from Figures 7.2 and 7.3.

The use of a smaller horizon value near the ends of the bar affects computational expense by reducing the total number of bonds in the model. The test case illustrated in Figure 7.1 contains 46.5 million bonds. In the case in which a constant horizon value of 0.25 is applied over the entirety of the domain, the total number of bonds increases to 92.6 million, resulting in a significant increase in computational cost for evaluation of the internal force density. For solutions employing implicit time integration, the reduction in the number of bonds also decreases the computational expense of solving the global linear system, if applicable.

An additional effect on computational expense pertains to the maximum stable time step for explicit transient dynamic simulations [33, 32]. The maximum stable time step was found to be

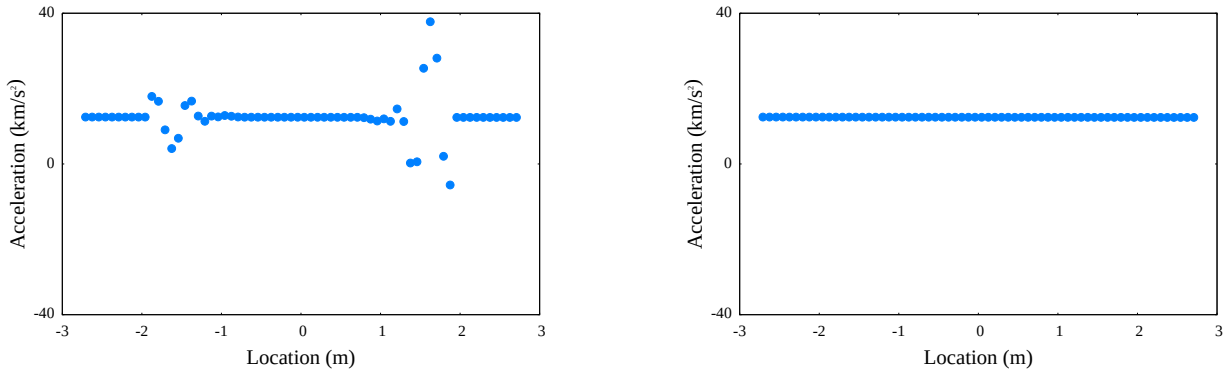

(a) Standard peridynamic model.

(b) Peridynamic partial stress model.

Figure 7.3: Acceleration values along the length of the bar under an imposed quadratic displacement field.

2.03e-5 s for the constant-horizon case, and 7.15e-6 s for the varying-horizon case. Thus the use of a smaller horizon near the ends of the bar decreases the cost of an internal force evaluation, but may reduce the maximum stable time step, resulting in an increase in the total number of time steps required to complete a simulation. It is often the case, however, that for simulations involving both local and nonlocal models, the maximum stable time step is determined by the local model. In this case, the maximum stable time step associated with the nonlocal model has no effect on computational expense.

7.3 Coupling *Peridigm* and *Albany*

The partial-stress approach was applied to directly couple a meshfree peridynamic model and a standard (local) finite-element model though integration of the *Peridigm* and *Albany* codes. The goal was to enable simulations in which a meshfree peridynamic model is applied only in regions susceptible to material failure. Connection to the remainder of the domain, modeled using a standard local model, is achieved using a transition region in which a peridynamic partial stress model is applied. This configuration, illustrated in Figure 7.7, allows for reduction of the peridynamic horizon, and hence the degree of nonlocality, from a relatively large value in the meshfree peridynamic domain, to a small value at the interface to the standard local model.

The software design for coupling the *Peridigm* and *Albany* codes is illustrated in Figure 7.4. The required *Peridigm* components were compiled as a library and linked directly into *Albany*, creating a single, unified executable. Under this approach, *Albany* acts as the primary driver of the simulation. An preliminary call to the *Peridigm* library is made at the onset of the simulation to initialize the meshfree discretization and execute the proximity search required for identification of peridynamic bonds. Subsequent calls to *Peridigm* are made for evaluation of the internal force. For meshfree peridynamic domains, *Peridigm* computes nodal forces directly. For peridynamic partial stress domains, *Peridigm* computes a stress tensor at peridynamic material points that serve

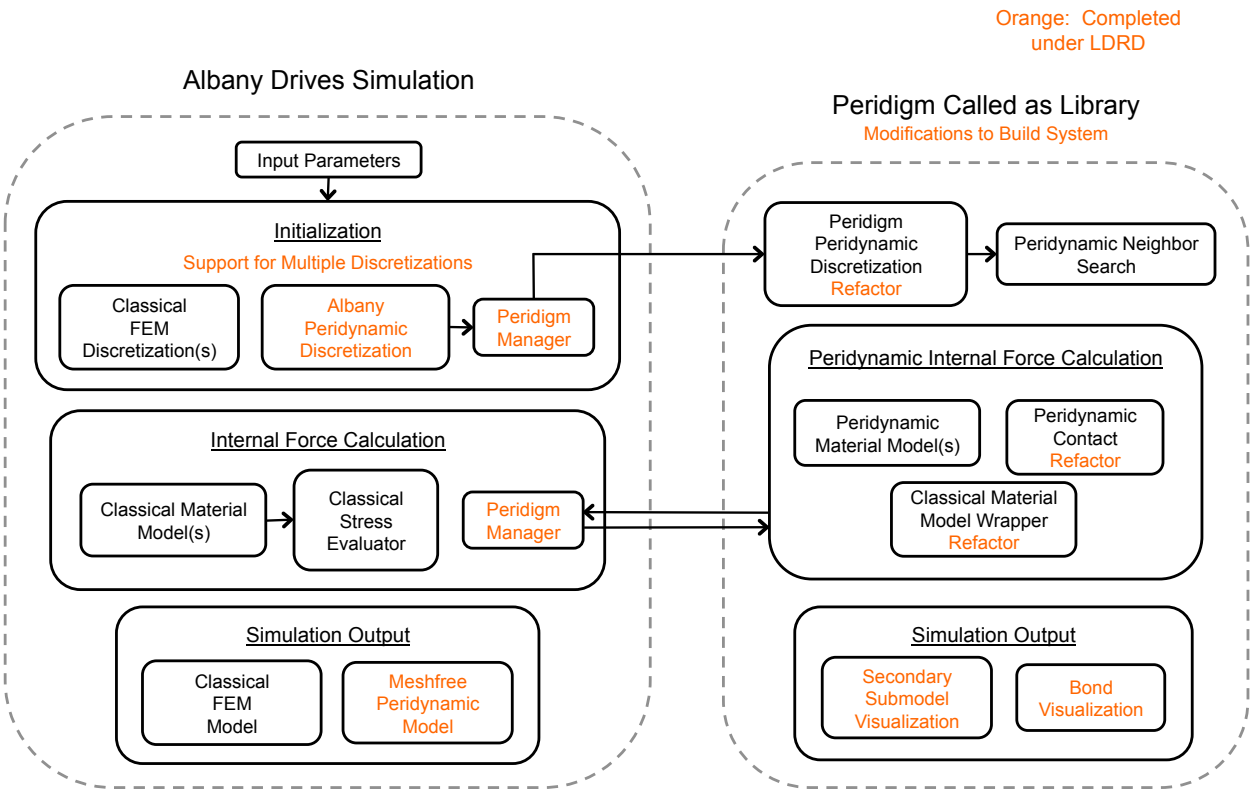

Figure 7.4: Schematic illustration of the software interfaces between the *Peridigm* and *Albany* codes. Software development completed specifically for the coupling effort is highlighted in orange.

as integration points in the *Albany* discretization. This approach allows for a straightforward transition from a peridynamic partial stress domain to a domain modeled with classical continuum mechanics. Transitions from meshfree peridynamic domains to partial stress domains discretized with standard finite elements requires special treatment, as described below.

Calculation of nodal forces for meshfree peridynamic simulations carried out within the coupled *Albany-Peridigm* framework is handled entirely by the *Peridigm* library. At the onset of each time step, *Albany* sends to the *Peridigm* library the current nodal displacements and velocities, as determined by the time integration routine. Based on this kinematic information, the *Peridigm* library computes nodal forces via the specified peridynamic constitutive model, optional peridynamic damage model, and optional peridynamic contact model. The nodal forces are passed back to *Albany* and applied within the time integrator to advance the simulation to the next time step.

Calculation of nodal forces for peridynamic partial stress domains discretized with standard finite elements is achieved using a combination of *Albany* and *Peridigm* routines. As illustrated in Figures 7.5 and 7.6, the peridynamic material points are situated at the locations of Gauss integration points over a set of elements which are managed by *Albany*. At the onset of each time step, element-level interpolation routines are called within *Albany* to compute displacements and velocities at the peridynamic material points. This data is then sent to the *Peridigm* library, which computes the peridynamic partial stress. The partial stress values are then treated by *Albany* fol-

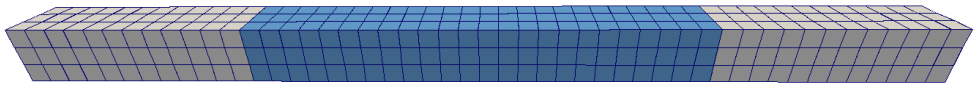

(a) Element configuration containing (local) classical continuum mechanics, shown in gray, and (nonlocal) peridynamic partial stress, shown in blue.

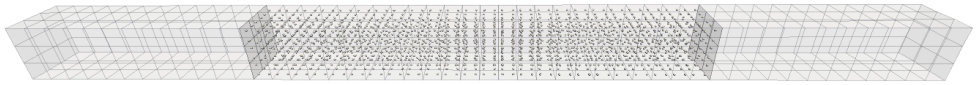

(b) Illustration of peridynamic material points positioned within the partial-stress elements.

Figure 7.5: Configuration utilizing both classical continuum mechanics and peridynamic partial stress.

lowing the standard finite-element procedure: the element-level divergence operator is applied over the integration points (peridynamic material points) to compute contributions to the nodal forces. Following this approach, the peridynamic partial stress material points are not co-located with nodes in the *Albany* discretization, and peridynamic bonds pass across multiple elements, as shown in Figure 7.6.

One difficulty with the *Albany-Peridigm* coupling approach described above is treatment of the element surface directly adjacent to the meshfree discretization. Here, the *Albany* elements produce nodal forces that are not balanced by the meshfree model, which acts only on peridynamic material points. In effect, surfaces adjacent to the meshfree domains are treated, by default, as free surfaces. To resolve this issue, a constraint may be imposed on the nodes located on the affected element surfaces to fully prescribe their displacement as a function of the displacements of nodes and peridynamic material points in their vicinity. Specifically, a quadratic function approximating the displacement field in the vicinity of the interface between the finite-element discretization and the meshfree discretization may be constructed via a least-squares fit. The nodes and peridynamic material points within a distance equal to the peridynamic horizon of the mesh-meshfree interface are used as fitting data, and the resulting approximation of the displacement field is used to specify the displacements of the nodes located on the *Albany* element faces at the mesh-meshfree interface.

Coupling of the *Albany* and *Peridigm* codes is demonstrated in Figures 7.7 and 7.8 for a bar under tension. As shown in Figure 7.7, the bar is discretized into five domains: meshfree peridynamics at the center of the bar, coupled at both ends to peridynamic partial stress regions, which are in turn coupled to classical continuum mechanics regions. Boundary conditions are applied

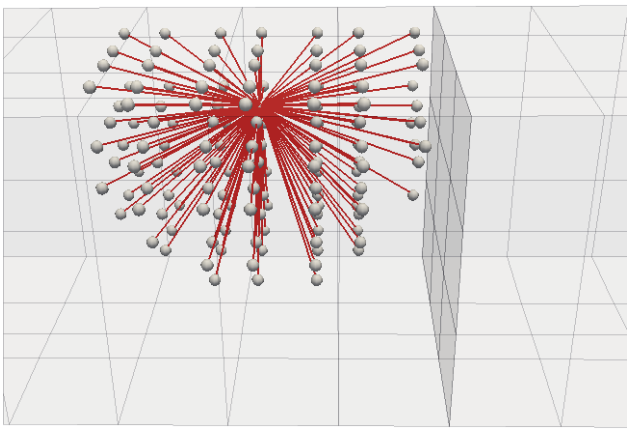

Figure 7.6: The peridynamic partial stress formulation requires communication between material points across multiple elements. Peridynamic bonds are shown in red.

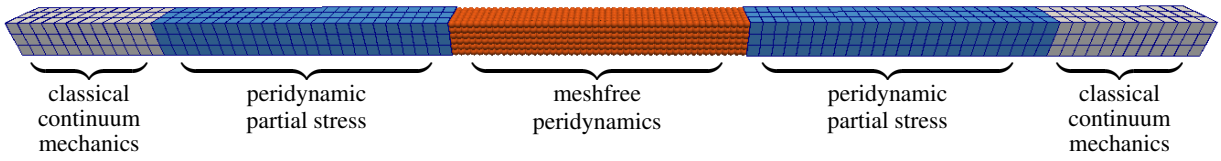

Figure 7.7: Configuration for coupled simulation including classical continuum mechanics, a partial-stress peridynamic model, and a standard meshfree peridynamic model.

only at the free surfaces at the ends of the bar, which avoids the need to apply constraints directly to the nonlocal model. The simulation was carried out as a static problem using the Newton-free Jacobian Krylov solver available in *Albany*. The computational solution successfully recovers the expected linear displacement, as shown in Figure 7.8.

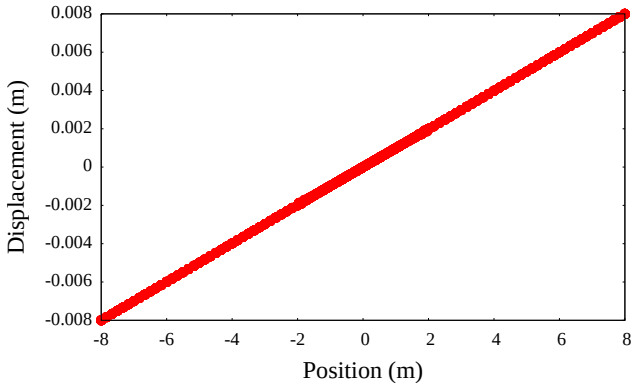

(a) Displacement as a function of location along the length of the bar for the simulation of a bar under tension.

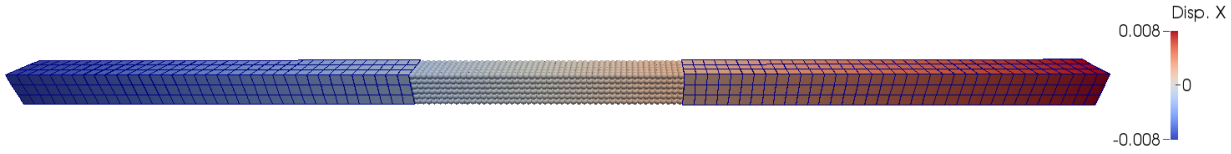

(b) Displacement in the longitudinal direction for the simulation of a bar under tension.

Figure 7.8: Results for the simulation of a bar under tension.

Chapter 8

Summary

Peridynamics is a nonlocal extension of continuum mechanics that provides a consistent mathematical framework for modeling material failure and fragmentation [61, 64, 65, 43]. This is in contrast to the partial differential equations of the Cauchy theory, which do not apply directly on these mathematical singularities because the necessary partial derivatives of the deformation are not defined there. The foremost advantage of peridynamics is that it does not require specialization for the treatment of discontinuities, and instead aims to incorporate directly phenomena such as cracks, dislocations, and voids. Further, the meshfree discretization of peridynamics developed by Silling and Askari [63] provides a means to simulate propagating cracks and large deformations. Limitations of peridynamics for engineering analyses include computational expense and the need to apply boundary conditions over a nonlocal volumetric region [2, 43]. This motivates the development of strategies for combined simulations in which peridynamics is employed only in regions susceptible to material failure, and a local model is applied elsewhere.

This report is an overview of the LDRD project "Strong Local-Nonlocal Coupling for Integrated Fracture Modeling," completed within the CIS Investment Area at Sandia National Laboratories. The principal goal of this project was the development of novel local-nonlocal coupling formulations to enable direct integration of peridynamic models within analysis codes based on classical continuum mechanics. In addition to the treatment of local-nonlocal interfaces, effective integration of peridynamics and classical continuum mechanics required advances in peridynamic modeling, including improved constitutive models, failure models, and discretization strategies.

The most significant research and development accomplishments of this project are:

- The *partial-stress* and *splice* formulations for peridynamic models that enable the use of a variable nonlocal length scale, greatly reducing the mathematical incompatibility between local and nonlocal equations [67, 66].
- A novel blending-based coupling strategy for the coupling of peridynamics and classical continuum mechanics [55].
- A class of *position-aware* peridynamic constitutive models that dramatically reduce surface effects at domain boundaries [37].
- Strategies for improved performance and convergence behavior of meshfree peridynamic models [51, 56].

- A novel approach to modeling ductile failure within the peridynamic framework.
- Software implementations within the *Peridigm* [46, 48] and *Albany* [50] codes of the partial-stress coupling strategy, the position-aware constitutive models, and the enhancements to meshfree peridynamic models for improved performance and convergence behavior.

The accomplishments of this project have been disseminated through journal articles, book chapters, and conference presentations, as detailed in Appendix A.

Development of local-nonlocal coupling strategies for integrated fracture modeling has drawn on expertise at the forefront of mathematics, computational mechanics, scientific computing, and engineering. The resulting approaches for combined local and nonlocal simulations have application to a broad class of problems in the areas of nuclear and conventional weapon safety and surety. Improving peridynamics as an engineering tool and better enabling its integration within existing analyst workflows provide a path forward for predictive simulation of material failure and fracture.

References

[1] B. Aksoylu and M. L. Parks. Variational theory and domain decomposition for nonlocal problems. *Applied Mathematics and Computation*, 217:6498–6515, 2011.

[2] Y. Azdoud, F. Han, D. Littlewood, G. Lubineau, and P. Seleson. Coupling local and non-local models. In F. Bobaru, J.T. Foster, P. Geubelle, and S.A. Silling, editors, *Handbook of Peridynamic Modeling*. Taylor & Francis / CRC Press, Expected publication 2015.

[3] S. Badia, P. Bochev, R. Lehoucq, M. Parks, J. Fish, M. A. Nuggehally, and M. Gunzburger. A force-based blending model for atomistic-to-continuum coupling. *International Journal for Multiscale Computational Engineering*, 5:387–406, 2007.

[4] S. Badia, M. Parks, P. Bochev, M. Gunzburger, and R. Lehoucq. On atomistic-to-continuum coupling by blending. *Multiscale Model. Simul.*, 7(1):381–406, 2008.

[5] P. T. Bauman, H. Ben Dhia, N. Elkhodja, J. T. Oden, and S. Prudhomme. On the application of the Arlequin method to the coupling of particle and continuum models. *Comput. Mech.*, 42:511–530, 2008.

[6] T. Belytschko and S. P. Xiao. Coupling methods for continuum model with molecular model. *International Journal for Multiscale Computational Engineering*, 1(1):115–126, 2003.

[7] H. Ben Dhia. Multiscale mechanical problems: the Arlequin method. *C. R. Acad. Sci. Paris - Séries IIB - Mechanics-Physics-Astronomy*, 326:899–904, 1998.

[8] A. Bessa, J.T. Foster, T. Belytschko, and Wing Kam Liu. A meshfree unification: reproducing kernel peridynamics. *Computational Mechanics*, 53(6):1251–1264, June 2014.

[9] F. Bobaru and Y. Doh Ha. Adaptive refinement and multiscale modeling in 2D peridynamics. *International Journal for Multiscale Computational Engineering*, 9(6):635–660, 2011.

[10] Florin Bobaru and Monchai Duangpanya. The peridynamic formulation for transient heat conduction. *International Journal of Heat and Mass Transfer*, 53(19):4047–4059, 2010.

[11] Florin Bobaru and Monchai Duangpanya. A peridynamic formulation for transient heat conduction in bodies with evolving discontinuities. *Journal of Computational Physics*, 231(7):2764–2785, 2012.

[12] P. Bochev, R. Lehoucq, M. Parks, S. Badia, and M. Gunzburger. Blending methods for coupling atomistic and continuum models. In J. Fish, editor, *Multiscale Methods: Bridging the Scales in Science and Engineering*, chapter 6, pages 165–189. Oxford University Press, Oxford, 2009.

[13] Javier Bonet and Richard D. Wood. *Nonlinear continuum mechanics for finite element analysis*. Cambridge University Press, 1st edition, 1997.

[14] MS Breitenfeld, PH Geubelle, O Weckner, and SA Silling. Non-ordinary state-based peridynamic analysis of stationary crack problems. *Computer Methods in Applied Mechanics and Engineering*, 272:233–250, 2014.

[15] X. Chen and M. Gunzburger. Continuous and discontinuous finite element methods for a peridynamics model of mechanics. *Comput. Methods Appl. Mech. Engrg.*, 200:1237–1250, 2011.

[16] B. D. Coleman and W. Noll. The thermodynamics of elastic materials with heat conduction and viscosity. *Archive for Rational Mechanics and Analysis*, 13:167–178, 1963.

[17] *Cubit* mesh generation code, 2014. `http://cubit.sandia.gov`.

[18] H. Ben Dhia. Numerical modelling of multiscale problems: the Arlequin method. In *CD Proceedings of ECCM'99, Munchen*, 1999.

[19] Q. Du, M. Gunzburger, R. B. Lehoucq, and K. Zhou. A nonlocal vector calculus, nonlocal volume-constrained problems, and nonlocal balance laws. *Math. Models Methods Appl. Sci.*, 23:493–540, 2013.

[20] E. Emmrich and O. Weckner. The peridynamic equation and its spatial discretisation. *Math. Model. Anal.*, 12(1):17–27, 2007.

[21] Etienne Emmrich and Olaf Weckner. On the well-posedness of the linear peridynamic model and its convergence towards the Navier equation of linear elasticity. *Communications in Mathematical Sciences*, 5:851–864, 2007.

[22] JE Field, SM Walley, WG Proud, HT Goldrein, and CR Siviour. Review of experimental techniques for high rate deformation and shock studies. *International Journal of Impact Engineering*, 30:725–775, 2004.

[23] J. Fish, M. A. Nuggehally, M. S. Shephard, C. R. Picu, S. Badia, M. L. Parks, and M. Gunzburger. Concurrent AtC coupling based on a blend of the continuum stress and the atomistic force. *Comput. Methods Appl. Mech. Engrg.*, 196:4548–4560, 2007.

[24] J. T. Foster, S. A. Silling, and W. W. Chen. Viscoplasticity using peridynamics. *International Journal for Numerical Methods In Engineering*, 81:1242–1258, 2010.

[25] Michael Heroux, Roscoe Bartlett, Vicki Howle Robert Hoekstra, Jonathan Hu, Tamara Kolda, Richard Lehoucq, Kevin Long, Roger Pawlowski, Eric Phipps, Andrew Salinger, Heidi Thornquist, Ray Tuminaro, James Willenbring, and Alan Williams. An Overview of Trilinos. Technical Report SAND2003-2927, Sandia National Laboratories, 2003.

[26] Michael A. Heroux, Roscoe A. Bartlett, Vicki E. Howle, Robert J. Hoekstra, Jonathan J. Hu, Tamara G. Kolda, Richard B. Lehoucq, Kevin R. Long, Roger P. Pawlowski, Eric T. Phipps, Andrew G. Salinger, Heidi K. Thornquist, Ray S. Tuminaro, James M. Willenbring, Alan

Williams, and Kendall S. Stanley. An overview of the trilinos project. *ACM Trans. Math. Softw.*, 31(3):397–423, 2005.

[27] W. Hu, Y. D. Ha, and F. Bobaru. Numerical integration in peridynamics. Technical report, University of Nebraska-Lincoln, September 2010.

[28] Bahattin Kilic. *Peridynamic theory for progressive failure prediction in homogeneous and heterogeneous materials*. PhD thesis, The University of Arizona, 2008.

[29] J. Knap and M. Ortiz. An analysis of the quasicontinuum method. *J. Mech. Phys. Solids*, 49:1899–1923, 2001.

[30] D. Krajcinovic. *Damage Mechanics*. Springer: New York, 1996.

[31] R. B. Lehoucq and S. A. Silling. Force flux and the peridynamic stress tensor. *Journal of the Mechanics and Physics of Solids*, 56:1566–1577, 2008.

[32] D. Littlewood. Roadmap for software implementation. In F. Bobaru, J.T. Foster, P. Geubelle, and S.A. Silling, editors, *Handbook of Peridynamic Modeling*. Taylor & Francis / CRC Press, Expected publication 2015.

[33] David Littlewood, Jesse Thomas, and Timothy Shelton. Estimation of the critical time step for peridynamic models. Presented at SIAM Conference on Mathematical Aspects of Materials Science, Philadelphia, PA, July 2013.

[34] David J. Littlewood. Simulation of dynamic fracture using peridynamics, finite element modeling, and contact. In *ASME 2010 International Mechanical Engineering Congress and Exposition*, pages 209–217. American Society of Mechanical Engineers, 2010.

[35] Richard W. Macek and Stewart A. Silling. Peridynamics via finite element analysis. *Finite Elements in Analysis and Design*, 43(15):1169–1178, 2007.

[36] E. Madenci and E. Oterkus. *Peridynamic Theory and Its Applications*. Springer, New York, 2013.

[37] J. A. Mitchell, S. A. Silling, and D. J. Littlewood. A position-aware linear solid (pals) model for isotropic elastic materials. *Journal of Mechanics of Materials and Structures*. Accepted for publication.

[38] J.A. Mitchell. On the 'dsf' and the 'dreaded surface effect'. Sandia National Laboratories, 2013. SAND2013-1927C; Workshop on Nonlocal Damage and Failure: Peridynamics and Other Nonlocal Methods, San Antonio, Texas, March 11-12.

[39] John Mitchell. Ordinary isotropic peridynamics models; position aware viscoelastic (paṽe). Presented at PANACM 2015, 1st Pan-American Congress on Computational Mechanics, Beunos Aires, Argentina, 2015. Sandia National Laboratories, SAND2015-3078C.

[40] John A. Mitchell. A non-local, ordinary-state-based viscoelasticity model for peridynamics. Technical Report SAND2011-8064, Sandia National Laboratories, May 2011. Available at https://cfwebprod.sandia.gov/cfdocs/CompResearch/docs/SAND2011-Viscoelasticity.pdf.

[41] John A. Mitchell. A nonlocal, ordinary, state-based plasticity model for peridynamics. Technical Report SAND2011-3166, Sandia National Laboratories, May 2011. Available at https://cfwebprod.sandia.gov/cfdocs/CompResearch/docs/SAND2011-3166.pdf.

[42] S. Oterkus, E. Madenci, and A. Agwai. Peridynamic thermal diffusion. *Journal of Computational Physics*, 265:71–96, 2014.

[43] Peridynamics Capabilities Review Panel. Peridynamics capabilities review panel report. Technical Report SAND2015-1921, Sandia National Laboratories, Albuquerque, NM and Livermore, CA, 2015.

[44] *Paraview* visualization code, 2014. http://www.paraview.org.

[45] M. L. Parks, R. B. Lehoucq, S. J. Plimpton, and S. A. Silling. Implementing peridynamics within a molecular dynamics code. *Comp. Phys. Comm.*, 179(11):777–783, 2008.

[46] M. L. Parks, D. J. Littlewood, J. A. Mitchell, and S. A. Silling. Peridigm Users' Guide v1.0.0. SAND Report 2012-7800, Sandia National Laboratories, Albuquerque, NM and Livermore, CA, 2012.

[47] Michael L. Parks, Pablo Seleson, Steven J. Plimpton, Richard B. Lehoucq, and Stewart A. Silling. Peridynamics with LAMMPS: A user guide. Technical Report SAND2010-5549, Sandia National Laboratories, 2010.

[48] *Peridigm* peridynamics code, 2014. http://peridigm.sandia.gov.

[49] S. Prudhomme, H. Ben Dhia, P. T. Bauman, N. Elkhodja, and J. T. Oden. Computational analysis of modeling error for the coupling of particle and continuum models by the Arlequin method. *Comput. Methods Appl. Mech. Engrg.*, 197:3399–3409, 2008.

[50] A.G. Salinger, R.A. Bartlett, Q. Chen, X. Gao, G.A. Hansen, I. Kalashnikova, A. Mota, R.P. Muller, E. Nielsen, J.T. Ostien, R.P. Pawlowski, E.T. Phipps, and W. Sun. Albany: A component–based partial differential equation code built on trilinos. SAND Report 2013-8430J, Sandia National Laboratories, Albuquerque, NM and Livermore, CA, 2013.

[51] P. Seleson. Improved one-point quadrature algorithms for two-dimensional peridynamic models based on analytical calculations. *Computer Methods in Applied Mechanics and Engineering*, 282:184–217, 2014.

[52] P. Seleson, S. Beneddine, and S. Prudhomme. A force-based coupling scheme for peridynamics and classical elasticity. *Computational Materials Science*, 66:34–49, 2013.

[53] P. Seleson and M. Gunzburger. Bridging methods for atomistic-to-continuum coupling and their implementation. *Commun. Comput. Phys.*, 7(4):831–876, 2010.

[54] P. Seleson, M. Gunzburger, and M. L. Parks. Interface problems in nonlocal diffusion and sharp transitions between local and nonlocal domains. *Comput. Methods Appl. Mech. Engrg.*, 266:185–204, 2013.

[55] P. Seleson, Y. D. Ha, and S. Beneddine. Concurrent coupling of bond-based peridynamics and the navier equation of classical elasticity by blending. *Journal for Multiscale Computational Engineering*, 13(2):91–113, 2015.

[56] P. Seleson and D. Littlewood. Convergence studies in meshfree peridynamic simulations. Submitted for publication.

[57] P. Seleson, M. L. Parks, M. Gunzburger, and R. B. Lehoucq. Peridynamics as an upscaling of molecular dynamics. *Multiscale Model. Simul.*, 8(1):204–227, 2009.

[58] P. D. Seleson. *Peridynamic Multiscale Models for the Mechanics of Materials: Constitutive Relations, Upscaling from Atomistic Systems, and Interface Problems*. PhD thesis, Florida State University, 2010. Electronic Theses, Treatises and Dissertations. Paper 273.

[59] Pablo Seleson and Michael L. Parks. On the role of the influence function in the peridynamic theory. *Journal for Multiscale Computational Engineering*, 9(6):689–706, 2011.

[60] V. B. Shenoy, R. Miller, E. B. Tadmor, R. Phillips, and M. Ortiz. Quasicontinuum models of interfacial structure and deformation. *Phys. Rev. Lett.*, 80(4):742–745, 1998.

[61] S. A. Silling. Reformulation of elasticity theory for discontinuities and long-range forces. *Journal of the Mechanics and Physics of Solids*, 48:175–209, 2000.

[62] S. A. Silling. Linearized theory of peridynamic states. *J. Elast.*, 99:85–111, 2010.

[63] S. A. Silling and E. Askari. A meshfree method based on the peridynamic model of solid mechanics. *Computers and Structures*, 83:1526–1535, 2005.

[64] S. A. Silling, M. Epton, O. Weckner, J. Xu, and E. Askari. Peridynamic states and constitutive modeling. *Journal of Elasticity*, 88:151–184, 2007.

[65] S. A. Silling and R. B. Lehoucq. The peridynamic theory of solid mechanics. *Advances in Applied Mechanics*, 44:73–166, 2010.

[66] S. A. Silling, D. J. Littlewood, and P. D. Seleson. Variable horizon in a peridynamic medium. *Journal of Mechanics of Materials and Structures*. Accepted for publication.

[67] S. A. Silling, D. J. Littlewood, and P. D. Seleson. Variable horizon in a peridynamic medium. Technical Report 2014-19088, Sandia National Laboratories, Albuquerque, NM and Livermore, CA, 2014.

[68] Stewart A. Silling and Richard B. Lehoucq. Convergence of peridynamics to classical elasticity theory. *Journal of Elasticity*, 93:13–37, 2008.

[69] E. B. Tadmor, M. Ortiz, and R. Phillips. Quasicontinuum analysis of defects in solids. *Philosophical Magazine A*, 73:1529–1563, 1996.

[70] The *Trilinos* project, 2015. https://trilinos.org.

[71] M. R. Tupek and R. Radovitzky. An extended constitutive correspondence formulation of peridynamics based on nonlinear bond-strain measures. *Journal of the Mechanics and Physics of Solids*, 65:82–92, 2014.

[72] M. R. Tupek, J. J. Rimoli, and R. Radovitzky. An approach for incorporating classical continuum damage models in state-based peridynamics. *Computer methods in applied mechanics and engineering*, 263:20–26, 2013.

[73] T. L. Warren, S. A. Silling, A. Askari, O. Weckner, M. A. Epton, and J. Xu. A non-ordinary state-based peridynamic method to model solid material deformation and fracture. *International Journal of Solids and Structures*, 46:1186–1195, 2009.

[74] Gerald W. Wellman. A simple approach to modeling ductile failure. Technical Report SAND2012-1343, Sandia National Laboratories, Albuquerque, NM 87185, 2012.

[75] S. P. Xiao and T. Belytschko. A bridging domain method for coupling continua with molecular dynamics. *Comput. Methods Appl. Mech. Engrg.*, 193:1645–1669, 2004.

[76] K. Yu, X. J. Xin, and K. B. Lease. A new adaptive integration method for the peridynamic theory. *Modelling Simul. Mater. Sci. Eng.*, 19:045003, 2011.

Appendix A

Listing of Publications and Presentations

The following journal articles, book chapters, invited conference presentations, and intellectual property were completed over the course of this project. They were funded either in whole or in part by the Laboratory Directed Research and Development program at Sandia National Laboratories.

A.1 Peer-Reviewed Journal Articles

1. Silling, S., Littlewood, D., and Seleson, P. Variable horizon in a peridynamic medium. *Journal of Mechanics of Materials and Structures*. Accepted for publication.

2. Seleson, P., and Littlewood, D. Convergence studies in meshfree peridynamic simulations. Submitted for publication.

3. Mitchell, J., Silling, S., and Littlewood, D. A position-aware linear solid (PALS) model for isotropic elastic materials. *Journal of Mechanics of Materials and Structures*. Accepted for publication.

4. Seleson, P. Improved one-point quadrature algorithms for two-dimensional peridynamic models based on analytical calculations, *Computer Methods in Applied Mechanics and Engineering*, 282, pp. 184-217, 2014.

5. Seleson, P., Ha, Y.D., and Beneddine, S., Concurrent coupling of bond-based peridynamics and the navier equation of classical elasticity by blending, *International Journal for Multiscale Computational Engineering*, 13(2), pp. 91-113, 2015.

6. DElia, M., Perego, M., Bochev, P., Littlewood, D. *A coupling strategy for nonlocal and local diffusion models with mixed volume constraints and boundary conditions*. Submitted for publication.

A.2 Book Chapters

1. Azdoud, Y., Han, F., Littlewood, D., Lubineau, G., and Seleson, P. Coupling local and nonlocal models, in *Handbook of Peridynamic Modeling*, Florin Bobaru, John T. Foster, Philippe

H. Geubelle, and Stewart A. Silling, eds., Taylor & Francis Group, CRC Press. Accepted for publication.

2. Littlewood, D., Roadmap for software implementation, in *Handbook of Peridynamic Modeling*, Florin Bobaru, John T. Foster, Philippe H. Geubelle, and Stewart A. Silling, eds., Taylor & Francis Group, CRC Press. Accepted for publication.

A.3 Invited Conference Presentations

1. Seleson, P., Littlewood, D. Convergence studies of meshfree peridynamic simulations. The 8th International Congress on Industrial and Applied Mathematics, August 10-14, 2015, Beijing, China.

2. Seleson, P. A blending approach to concurrently couple peridynamics and classical continuum mechanics. The 8th International Congress on Industrial and Applied Mathematics, August 10-14, 2015, Beijing, China.

3. Littlewood, D., Silling, S., Seleson, P., Mitchell, J. Coupling approaches for integrating meshfree peridynamic models with classical finite element analysis. 13th US National Congress on Computational Mechanics, San Diego, California, July 26-30, 2015.

4. Seleson, P., Littlewood, D. Convergence studies of meshfree peridynamic simulations. 13th US National Congress on Computational Mechanics, San Diego, California, July 26-30, 2015.

5. Seleson, P., Littlewood, D., Silling, S. A blending approach to concurrently couple peridynamics and classical continuum mechanics. 1st Pan-American Congress on Computational Mechanics, Buenos Aires, Argentina, April 27-29, 2015.

6. Mitchell, J. On a position aware viscoelastic (PAVE) model for peridynamics. 1st Pan-American Congress on Computational Mechanics, Buenos Aires, Argentina, April 27-29, 2015.

7. Seleson, P., Littlewood, D. Convergence studies of meshfree peridynamic simulations. Conference on Recent Developments in Continuum Mechanics and Partial Differential Equations, April 18-19, 2015, Lincoln, NE, USA.

8. Seleson, P., Ha, Y. D., Beneddine, S., Prudhomme, S. A concurrent multiscale blending scheme for local/nonlocal coupling. AMS Spring Southeastern Sectional Meeting, March 27-29, 2015, Huntsville, AL, USA.

9. Littlewood, D., Silling, S., Seleson, P. Local-nonlocal coupling for modeling fracture. ASME International Mechanical Engineering Congress and Exposition, Montreal, Canada, Nov. 14-20, 2014.

10. Seleson, P., Littlewood, D. Improved quadrature algorithms for peridynamic models. ASME International Mechanical Engineering Congress and Exposition, Montreal, Canada, Nov. 14-20, 2014.

11. Mitchell, J., Foster, J. An oridinary state based plasticity model for peridynamics. ASME International Mechanical Engineering Congress and Exposition, Montreal, Canada, Nov. 14-20, 2014.

12. Littlewood, D., Silling, S., Seleson, P., Mitchell, J. Integrating meshfree peridynamic models with classical finite element analysis. Workshop on Meshfree Methods for Large-Scale Computational Science and Engineering, Tampa, Florida, Oct. 27-28, 2014.

13. Seleson, P., Littlewood, D., Silling, S. A blending approach to concurrently couple peridynamics and classical continuum mechanics. 13th International Symposium on Multiscale, Multifunctional and Functionally Graded Materials, October 19-22, 2014, Taua Resort, Sao Paulo, Brazil.

14. Mitchell, J., and Silling, S., and Littlewood, D. On position aware peridynamics constitutive models. U.S. National Congress of Theoretical and Applied Mechanics, East Lansing, Michigan, June 15-20, 2014.

15. Seleson, P., Ha, Y. D., Beneddine, S. Concurrent coupling of peridynamics and classical continuum mechanics by blending. 17th U.S. National Congress on Theoretical and Applied Mechanics, June 15-20, 2014, East Lansing, MI, USA.

16. Seleson, P. Mathematical modeling and analysis of interface problems for nonlocal diffusion. 2013 Joint Mathematics Meetings, January 9-12, 2013, San Diego, CA.

17. Parks, M., Littlewood, D., Mitchell, J., Silling, S. Peridigm: A new paradigm in computational peridynamics. 2013 Joint Mathematics Meetings, January 9-12, 2013, San Diego, CA.

18. Mitchell, J., Surface effects and affects on ordinary isotropic peridynamics models. SIAM Conference on Analysis of Partial Differential Equations (PD13), Orlando, FL, December 7-10, 2013.

19. Parks, M., Quadrature methods in peridynamics. SIAM Conference on Analysis of Partial Differential Equations (PD13), Orlando, FL, December 7-10, 2013.

20. Seleson, P., Improved one-point quadrature algorithms for two-dimensional peridynamic models based on analytic calculations. SIAM Conference on Analysis of Partial Differential Equations (PD13), Orlando, FL, December 7-10, 2013.

21. Littlewood, D. Coupling peridynamics and classical finite elements. ASME International Mechanical Engineering Congress and Exposition, San Diego, California, Nov. 15-21, 2013.

22. Littlewood, D., Parks, M., Mitchell, J., and Silling, S. The peridigm framework for peridynamic simulations. U.S. National Congress on Computational Mechanics, Raleigh, North Carolina, July 22-25, 2013.

23. Bond, S. Quadrature for nonlocal mechanics and peridynamics. U.S. National Congress on Computational Mechanics, Raleigh, North Carolina, July 22-25, 2013.

24. Silling, S., Seleson, S. Variable horizon in a peridynamic body. U.S. National Congress on Computational Mechanics, Raleigh, North Carolina, July 22-25, 2013.

25. Seleson, P. Concurrent coupling of bond-based peridynamics and Navier equation of classical elasticity by blending. U.S. National Congress on Computational Mechanics, Raleigh, North Carolina, July 22-25, 2013.

26. Silling, S., Seleson, P. Variable length scale in a peridynamic body. SIAM Conference on Mathematical Aspects of Materials Science, June 9-12, 2013, Philadelphia, PA.

27. Seleson, P. Concurrent coupling of bond-based peridynamics and Navier equation of classical elasticity by blending. SIAM Conference on Mathematical Aspects of Materials Science, June 9-12, 2013, Philadelphia, PA.

28. Parks, M., Littlewood, D., Mitchell, J., Silling, S. Peridigm: A new paradigm in computational peridynamics. SIAM Conference on Mathematical Aspects of Materials Science, June 9-12, 2013, Philadelphia, PA.

29. Parks, M., Littlewood, D., Mitchell, J., Silling, S. Peridigm: A new paradigm in computational peridynamics. Workshop on Nonlocal Damage and Failure: Peridynamics and Other Nonlocal Models, San Antonio, Texas, Mar. 11-12, 2013.

30. Mitchell, J. On the DSF and the dreaded surface effect. Workshop on Nonlocal Damage and Failure: Peridynamics and Other Nonlocal Models, San Antonio, Texas, Mar. 11-12, 2013.

31. Seleson, P. Interface problems in nonlocal diffusion and sharp transitions between local and nonlocal domains. Workshop on Nonlocal Damage and Failure: Peridynamics and Other Nonlocal Models, San Antonio, Texas, Mar. 11-12, 2013.

32. Parks, M., Littlewood, D., Mitchell, J., Silling, S. Peridigm: A New Paradigm in Computational Peridynamics. ASME International Mechanical Engineering Congress and Exposition, Houston, Texas, Nov. 9-15, 2012.

33. Seleson, P. Concurrent multiscale modeling in peridynamics. ASME International Mechanical Engineering Congress and Exposition, Houston, Texas, Nov. 9-15, 2012.

34. Seleson, P. Blending schemes for concurrent coupling of local and nonlocal continuum models in multiscale solid mechanics. 49th Annual Technical Meeting of The Society of Engineering Science, Atlanta, GA, Oct. 10-12, 2012.

A.4 Intellectual Property

1. The *Peridigm* and *Albany* codes are distributed as open-source software under the BSD 3-clause license.

DISTRIBUTION:

1 MS 0359 LDRD Program Office, 07911
1 MS 0359 D. Chavez, 01911
1 MS 0845 M.R. Tupek, 01542
1 MS 1160 D.J. Burnett, 05964
1 MS 1318 S.D. Bond, 01442
1 MS 1320 S.S. Collis, 01440
1 MS 1320 M.L. Parks, 01442
1 MS 1321 V. Tikare, 01444
1 MS 1321 R.M. Summers, 01446
1 MS 1322 J.B. Aidun, 01425
1 MS 1322 S.A. Silling, 01444
1 MS 1322 J.A. Mitchell, 01444
1 MS 1323 D.Z. Turner, 01444
1 MS 9042 J. Ostien, 08256
1 M. Gunzburger
400 Direct Science Library
Florida State University
Tallahassee FL, 32306-4120
1 P.D. Seleson
Oak Ridge National Laboratory
P.O. Box 2008, MS 6164
Oak Ridge, TN 37831
1 MS 0899 Technical Library, 9536 (electronic copy)


Sandia National Laboratories